UNIVERSITAT DE BARCELONA

Electrochemical tunneling microscopy and spectroscopy of electron transfer proteins

Montserrat López Martínez

ADVERTIMENT. La consulta d’aquesta tesi queda condicionada a l’acceptació de les següents condicions d'ús: La difusió d’aquesta tesi per mitjà del servei TDX (**www.tdx.cat**) i a través del Dipòsit Digital de la UB (**diposit.ub.edu**) ha estat autoritzada pels titulars dels drets de propietat intel·lectual únicament per a usos privats emmarcats en activitats d’investigació i docència. No s’autoritza la seva reproducció amb finalitats de lucre ni la seva difusió i posada a disposició des d’un lloc aliè al servei TDX ni al Dipòsit Digital de la UB. No s’autoritza la presentació del seu contingut en una finestra o marc aliè a TDX o al Dipòsit Digital de la UB (framing). Aquesta reserva de drets afecta tant al resum de presentació de la tesi com als seus continguts. En la utilització o cita de parts de la tesi és obligat indicar el nom de la persona autora.

ADVERTENCIA. La consulta de esta tesis queda condicionada a la aceptación de las siguientes condiciones de uso: La difusión de esta tesis por medio del servicio TDR (**www.tdx.cat**) y a través del Repositorio Digital de la UB (**diposit.ub.edu**) ha sido autorizada por los titulares de los derechos de propiedad intelectual únicamente para usos privados enmarcados en actividades de investigación y docencia. No se autoriza su reproducción con finalidades de lucro ni su difusión y puesta a disposición desde un sitio ajeno al servicio TDR o al Repositorio Digital de la UB. No se autoriza la presentación de su contenido en una ventana o marco ajeno a TDR o al Repositorio Digital de la UB (framing). Esta reserva de derechos afecta tanto al resumen de presentación de la tesis como a sus contenidos. En la utilización o cita de partes de la tesis es obligado indicar el nombre de la persona autora.

WARNING. On having consulted this thesis you’re accepting the following use conditions: Spreading this thesis by the TDX (**www.tdx.cat**) service and by the UB Digital Repository (**diposit.ub.edu**) has been authorized by the titular of the intellectual property rights only for private uses placed in investigation and teaching activities. Reproduction with lucrative aims is not authorized nor its spreading and availability from a site foreign to the TDX service or to the UB Digital Repository. Introducing its content in a window or frame foreign to the TDX service or to the UB Digital Repository is not authorized (framing). Those rights affect to the presentation summary of the thesis as well as to its contents. In the using or citation of parts of the thesis it’s obliged to indicate the name of the author.

Universitat de Barcelona
Departament de Ciència dels Materials i Química Física
Programa de doctorat:
ELECTROQUÍMICA. CIÈNCIA I TECNOLOGIA

Electrochemical tunneling microscopy and spectroscopy of electron transfer proteins

Memòria que presenta Montserrat López Martínez per optar al títol de Doctor per la Universitat de Barcelona

Directors

Dr. Pau Gorostiza Langa
Professor ICREA. Institut de Bioenginyeria de Catalunya

Dr. Ismael Díez Pérez
Departament de Ciència dels Materials i Química Física de la Universitat de Barcelona

Tutor

Dra. Elvira Gómez Valentin
Departament de Ciència dels Materials i Química Física de la Universitat de Barcelona

Barcelona, maig de 2017

Electrochemical tunneling microscopy and spectroscopy of electron transfer proteins

Montserrat López Martínez

Directors:

Dr. Pau Gorostiza Langa
Professor ICREA. Institut de Bioenginyeria de Catalunya

Dr. Ismael Díez Pérez
Departament de Ciència dels Materials i Química Física de la
Universitat de Barcelona

Tutor

Dra. Elvira Gómez Valentin
Departament de Ciència dels Materials i Química Física de la
Universitat de Barcelona

Barcelona, maig de 2017

Cover designed by Cristina Pérez-López Torres

A mis padres

Index

Outline

This thesis has been organized in seven chapters:

Chapter 1 is dedicated to an introduction to electron transfer (ET) processes in biology and the capabilities of Scanning Probe Microscopies to address its study. This chapter describes the different biological structures involved in ET processes, focusing in Azurin protein as a model system, and Photosystem I as a promising candidate for bioelectronics. The **objectives** of the thesis are included at the end of this chapter.

Chapters 2 to **6** include the vast majority of this thesis, as they contain the experimental results. Each chapter is treated individually and comprises a brief specific introduction to the matter, an experimental section, and results and discussion.

Chapter 2 presents the study of Azurin metalloprotein with Electrochemical Scanning Tunneling Spectroscopy (ECTS). This chapter includes the current voltage characteristics obtained for azurin and the obtention of a transition voltage value, which describes certain parameters that modulate the electron transfer process.

Chapter 3 describes the development of a new imaging mode of the Electrochemical Scanning Tunneling Microscope (ECSTM). This chapter includes the technical development, the validation of the technique with a well-known system, and the application of this new imaging mode to the study of Azurin metalloprotein.

Chapter 4 contains the development of a protocol to electrically insulate conductive Atomic Force Microscopy (cAFM) tips in order to work in electrolytic environments. Besides, it details the study of Azurin protein with cAFM under electrochemical control, including force controlled current-voltage spectroscopy measurements, and current and force-distances spectroscopies.

Chapter 5 details the study of different strategies followed to immobilize the photosystem I (PSI) complex protein to a gold electrode, including the AFM topographical characterization, and ECSTM imaging, and voltage-dependence imaging.

Chapter 6 presents ECTS measurements of PSI bound to a gold electrode. The current-distance measurements are shown for different sample and bias potentials, and the variance of the distance decay factor is analyzed.

Chapter 7 is reserved for the general conclusions of this thesis.

Finally, there is a summary of this thesis in Spanish, and two appended sections. Appendix I comprises a list of symbols and abbreviations that have been used throughout this thesis. Appendix II is a publication and communication list related to this thesis.

1

Introduction

1.1 Electron Transfer in Biology.

Electron transfer (ET) is a fundamental process in biology[1]. Among other roles, it is crucial for processes related with energy conversion, such as photosynthesis or cellular respiration, which enable all cell activity. Electron transfer takes place in and in between proteins, between metal centers or other cofactors that are separated by long distances. Many experimental and theoretical efforts have been dedicated to understand the process of ET in biology, not only for the fundamental interest of the field, but also for the potential technological applications of ET proteins as components of biomolecular electronic devices[2].

1.1.1 Redox ET proteins

Biological ET mostly takes place in between redox protein centers. The main redox protein families involved in ET processes are cytochromes, iron-sulfur clusters and cupredoxins. Combined, these redox proteins cover the whole range of reduction potentials in biology[3]. The redox centers of the different families have different geometries (Figure 1.1), but they all satisfy the requirements for efficient ET[1], 1) minimal change in geometry between redox states, what minimizes the reorganization energy associated to the ET process, and 2) efficient electronic coupling between donor and acceptor over long distances through the protein[4].

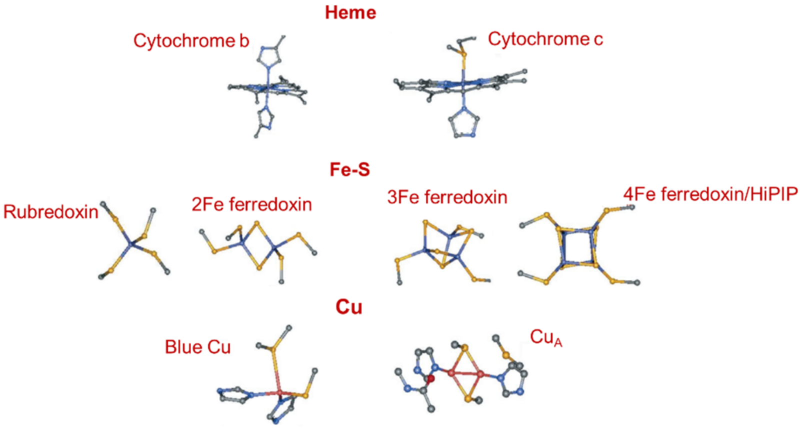

Figure 1.1. Active sites of the main redox proteins families for biological ET. Adapted with permission from (Solomon, E. Inorganic Chemistry 2006 45 (20), 8012-8025). Copyright (2006) American Chemical Society.

1.1.1.1 Cytochromes

Cytochromes are a family of heme-containing ET proteins, that are mostly present in the inner mitochondrial membrane of eukaryotic organisms, and in a wide variety of Gram-positive and Gram-negative bacteria[3].

Cytochromes with ET function contain a Fe center hexacoordinated. The iron atom is fixed into a rigid porphyrin through four equatorial bond and axially ligated to amino acids such as His, Met or an N-terminal amine group[3, 4]. Cytochromes are classified into *a, b, c, d, f, o* cytochrome types based on the absorption maxima of the heme macrocycle, which shifts as a result of different substituents on the periphery of the heme group. Cytochromes c are involved in biological ET processes in both aerobic and anaerobic respiratory chains, and are one of the most studied proteins classes[3, 5].

All different kinds of cytochromes have a rigid redox center, which makes the electronic structure very similar between them. However, since different cytochromes participate in different ET pathways, each cytochrome has evolved its ET properties to match those of its redox partners.

1.1.1.2 Fe-S proteins

Fe-S proteins are found in all forms of life, and play roles in crucial processes such as photosynthesis and respiration. These proteins show a wide range of redox potentials and different structural motifs that allow them to interact with different redox partners, participating in numerous biological processes [6, 7].

The common classification of Fe-S proteins is based on the number of iron and sulfur atoms and on structural motifs. We can distinguish three major groups: Rubredoxins, Ferredoxins, and HiPIPs (high potential iron-sulfur proteins). Each class of Fe-S usually have a common structural motif, different from the others, but all classes show a tetrahedral Fe coordinated by sulfur ligands[4]. Rubredoxins are the simplest among Fe-S proteins.

Ferredoxins are small, highly acidic Fe-S proteins. The Fe-S cluster is surrounded by a hydrophobic patch, which gives the protein a distinctive dark-brown color[8]. Among other functions, Ferredoxins act as the first electron acceptor in the stromal side of chloroplasts and work as electron carriers in photosynthesis.

HiPIPs (High Potential Fe-S proteins) are found mainly in photosynthetic anaerobic bacteria. HiPIPs contain a [4Fe−4S] cluster with a higher reduction potential than Ferredoxins, resulting on a $[4Fe-4S]^{2+/3+}$ state[9]. They are highly charged, either acidic or basic, and act as soluble periplasmic electron carriers in photosynthetic bacteria between the photosynthetic reaction center and the cytochrome *bc₁* complex[3].

Fe-S proteins also include complex Fe-S Centers present in hydrogenases and other enzymes, and in the Respiratory Complex chain, which we will discuss in a later section.

1.1.1.3 Cupredoxins

Copper proteins that act as ET mediators (or electron carriers) include blue copper proteins (or type 1) and dinuclear Cu_A centers. In cupredoxins, the metal centers are not fixed in the same way as in the heme groups of cytochromes, or the iron-sulfur clusters. The protein scaffold play a more significant role in keeping the geometry of the redox center. In both types of cupredoxins, Cu present a trigonal geometry and a strong copper-thiolate bond.

Cu_A dinuclear proteins have a binuclear copper center bridge by two cysteine ligands in a Cu_2S_2 *diamond* structure. This type of center is present in cytochrome *c* oxidase and other enzymes, which are terminal electron acceptors of different ET processes.

Blue copper proteins include mononuclear proteins involved in ET processes like Plastocyanins, Azurins, and multicopper enzymes[10] . These copper centers exhibit an extremely intense light absorption band, which is responsible for their deep blue color, and a very small Cu parallel hyperfine splitting in their electron paramagnetic spectra[11, 12]. The copper center structure of the blue copper proteins is very conserved even between different proteins. In all of them, the copper is coordinated by two His residues and one Cys residue as equatorial ligands. The active site structure is predetermined by the protein scaffold, thus there is no change in the active site at different oxidation states. Blue copper proteins are found in archaea, bacteria, and plants, where they act as electron carriers between donor and acceptor proteins in biological ET.

In the group of blue copper proteins, Azurin protein stands out as a model system to study ET in proteins. Azurin is a small globular protein that acts as an electron mediator in bacterial respiratory chains[13]. Azurin has a blue copper center located 8 Å below the Az surface and a solvent-exposed disulfide bridge between Cys 3 and Cys 26[14].

1.1.2 Respiratory complexes

The mitochondrial respiratory system is the main energy producer in eukaryotic cells[3]. It is composed by an assembly of more than 20 discrete electron carriers group into five multi-polypeptide complexes[15-19] and ubiquinone and cytochrome *c* as mobile electron carriers. (Figure 1.2)

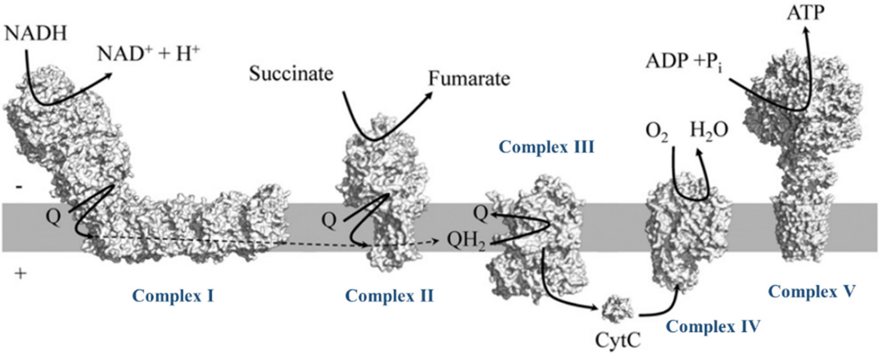

Figure 1.2. Mitochondrial respiratory chain. Schematic representation of the classic mitochondrial respiratory complexes. (Adapted from Marreiros BBA 2016[15]).

Electrons enter the respiratory chain at complex I (NADH-UQ oxidoreductase) and complex II (succinate dehydrogenase), where NADH and succinate act as electron donors to reduce ubiquinone to ubiquinol. Ubiquinol then transfer electrons through complex III (Cytochrome *bc$_1$* complex) to cytochrome *c*. Cytochrome *c* is then oxidized by complex IV (Cytochrome *c* oxidase complex) and transfer electrons to O_2 to produce water. This process is coupled to proton pumping across the membrane, which generates a proton gradient across the membrane. This proton gradient is used by complex V (ATP synthase) to generate ATP.

Mitochondrial Complex I is one of the largest macromolecular assemblies known and is the largest component of the respiratory chain[20]. The structure of the mammalian complex I was determined by cryo-EM at 5 Å resolution[21] and more recently at 4.2 and 3.9 Å[17, 22] . The mammalian mitochondrial enzyme consists of 44 different subunits (45 in total, as one subunit is present in two copies[21]). Both mitochondrial and bacterial complex I have an L-shaped structure with one hydrophobic arm embedded into the membrane and the hydrophilic arm pointing into the matrix space[21, 23]. For each NADH oxidation, complex I pumps four protons across the inner mitochondrial membrane, contributing a major part (about 40%) to the driving force for the ATP synthesis by complex V[20]. The electron transfer pathway can be traced through the protein structure [3, 24] with all redox centers within 14 Å from each other, a maximal distance for electron tunneling[25].

Complex II (Succinate dehydrogenase) is a membrane-bound protein that consist in four subunits. It has a hydrophilic domain[26] anchored to the membrane and a hydrophobic domain not involved in the ET pathway. Complex II catalyzes the oxidation of succinate with the reduction of ubiquinone, but this reaction is not coupled to charge translocation through the membrane.

Complex III (Cytochrome bc_1 complex) structure varies between different species: from bacteria where it has three subunits to the mammalian mitochondrial complex where it shows eleven subunits[3, 27]. This complex catalyzes the electron transfer from ubiquinol to cytochrome *c*, coupled to the translocation of two protons through the membrane for each ubiquinol molecule, contributing directly to the generation of membrane potential[16] .

In the complex IV (Cytochrome *c* oxidase complex) takes place the final step of the mammalian mithocondrial respiratory chain, the transfer of electrons from cytochrome *c* to O_2, forming $2H_2O$ molecules. This is a four-electron reaction that pumps 4 protons per 4 electrons across the membrane. The complex IV is composed by two catalytic subunits and 11 additional subunits[15, 16].

1.1.3 Photosynthetic proteins.

In a similar organization as the mitochondrial chain, for oxygenic photosynthesis, three protein complexes are located in the thylakoid membrane of chloroplast, where electron transfer takes place with proton translocation across the membrane[15, 28] (Figure 1.3). In this case, Plastocyanin (PC) and quinone act as mobile electron carriers. In the photosynthetic chain, the Photosystem II (PSII) oxidizes water to produce oxygen and reduced quinones. The reduced quinones are then used by the cytochrome *b₆f* to create a proton grandient across the membrane and to reduce the electron carrier, PC, which is the electron donor for Photosystem I (PSI). An additional photon is adsorbed by any of the PSI pigments and transferred to the special pair of chlorophylls P700, thus oxidizing it. The electron removed from P700 moves across an internal chain of electronic states and eventually reduces ferredoxin (Fd), the final electron acceptor of PSI. The P700 is re-reduced by the PC electron carrier. Reduced Fd is involved in several cellular pathways, mainly the reduction of NADP to NADPH, which together with ATP power the Calvin cycle to produce carbohydrates[29]. ATPase uses the created membrane potential to synthesize ATP. These protein complexes are present in all the organisms that carry oxygenic photosynthesis, cyanobacteria, algae and plants.

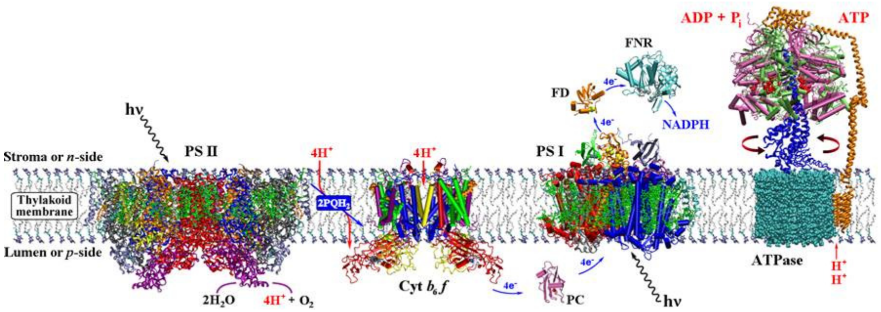

Figure 1.3. Schematic representation of the oxygenic photosynthetic electron transfer chain. Adapted with permission from (Blumberger, J. Chemical Reviews 2015, 115 (20), 11191-11238). Copyright (2015) American Chemical Society.

The crystallographic structure of the four complexes involved in oxygenic photosynthesis has been described[30-42], and high resolution has recently been reported for the PSI super complex[29, 43].

1.1.3.1 Photosystem II.

Several X-ray crystallographic structures have been reported for PSII [37, 40, 41, 44]. The PSII reaction center is composed by two similar proteins D1 and D2, which coordinate the electron-transfer components[45]. Bordering the reaction center there are the intrinsic light harvesting proteins CP43 and CP47 that bind 14 and 16 chlorophyll-a molecules respectively[41]. Light harvesting complex II (LHCII) antenna complexes are located in the periphery of PSII. The LHCII are trimers of light harvesting proteins Lhcb1, Lhcb2, Lhcb3. Each of the Lhcb proteins bind 14-16 chlorophylls a and b molecules and up to 4 carotenoids[3, 46]. The energy transfer from these LHCII antenna complexes to the PSII is mediated by the light harvesting proteins Lhcb4, Lhcb 5 and Lhcb6[30].

The oxygen production in PSII involves the oxidation of two water molecules and the adsorption of four photons. The special pair of chlorophylls P680 act as the primary electron donor. The absorption of a first photon translocates an electron from P680 to a bound quinone Q_A, via an accessory chlorophyll and a pheophytin molecule. The bound quinone Q_A then reduces a mobile quinone Q_B. The oxidized $P680^+$ center has the highest redox potential observed in a biological system (>1V), and oxidizes an adjacent tyrosine (Y_Z). Oxidized Y_Z extracts an electron from a cluster of four manganese ions, known as the oxygen-evolving complex (EOC)[47]. The EOC binds two water molecules, a calcium ion, a chloride ion and a bicarbonate ion. A second photochemical cycle reduces again the mobile quinone, resulting in Q_B^{2-}. Q_B^{2-} takes two protons from the stromal side and forms Q_BH_2, which is released into the lipid bilayer, and replaced by an oxidized quinone. At this point, the EOC has two oxidizing equivalents. After two more photochemical cycles, and it has four oxidizing equivalents which oxidize two water molecules and produces O_2[30].

1.1.3.2 Cytochrome b_6f complex

Chloroplast Cytochrome b_6f complex is similar to the mitochondrial Cytochrome bc_1 complex[30, 48], which may indicate that both complexes evolved from a common ancestor. The cytochrome b_6f complex is dimeric. Each monomer contains four large subunits: cytochrome *f*, cytochrome b_6, an iron-sulfur protein and the subunit IV, in addition to four small hydrophobic subunits: PetG, PetL, PetM, PetN[36, 42]. The extramembrane domains of cytochrom *f* and the iron-sulfur protein (at the luminal side of the protein) are shifted in comparison to the bc_1 complex [36, 42], and PetG, PetL, PetM and PetN have no parallels in cytochrome-bc_1 complex.

In cytochrome b_6f, the oxidation of a reduced quinone (bound to the luminal Q_0 site) releases two protons to the aqueous lumen. One electron is transferred from the reduced quinone to plastocyanin (PC) via an iron-sulfur protein and the cytochrome *f*. The second electron is translocated across the membrane through two heme groups of cytochrome b_6 to reduce a quinone bound to the stromal Q_i site. After a second reduction event, two protons of the stromal side have been used to reduce a quinone that then is released into the lipid bilayer[30].

1.1.3.3 Photosystem I

PSI of higher plants is composed mainly of two parts: the reaction center and the light harvesting complex I (LHCI) that surrounds the reaction center. LHCI maximizes the light absorption and transmits the energy to the reaction center.

The reaction center is composed by 19 subunits. Among them, PsaA-PsaB heterodimer forms the heart of the reaction center. It contains the special pair of chlorophylls P700, where the light driven charge separation starts, and the first electron acceptors A_0 (chlorophyll-a), A_1 (phylloquinone) and Fx (Fe4-S4 cluster). This heterodimer coordinates ~80 chlorophylls that act as additional antenna[34, 49]. The terminal electron acceptors of the chain, F_A and F_B, two Fe4-S4 clusters, are bound to the PsaC subunit. The rest of subunits are involved in the docking of Fd, PC, and the association with LHCI[30, 50, 51]. The PsaF subunit has a domain with several aminoacids with a positive charge, which forms an amphipathic motif in the luminal side of the complex. This domain appears to be essential for the electrostatical recognition of PC, and for the formation of a stable PSI-PC complex [51]. In the stromal side of the complex, we find an extramembranous domain, the “stromal hump”, composed of three subunits (PsaC, PsaD, and PsaE) are closely linked to one another, forming a binding groove for the electron acceptor Fd[51].

The peripheral light harvesting antenna (LHCI) is composed by four light-harvesting proteins (Lhca1-Lhca4) arranged into two dimers. LHCI complex docks with the PsaF subunit side of the reaction center[35]. The association of the LHCI to the reaction center is asymmetric, since only one monomer (Lhca1) binds tightly to the reaction center. The other Lhcas have weaker interactions with the reaction center[35, 52]. The composition of the LHCI may be altered depending on the light intensity or the nutrient availability. This, together with the flexible interaction with the reaction center is probably essential for the plant adaption to different light conditions[53].

The PSI reaction center is highly conserved between cyanobacteria algae and plants. The main differences are that plant PSI is much larger than its cyanobaterial counterpart [51], and that plant PSI-LHCI is present in monomeric form, while cyanobacteria present a trimeric PSI. Cyanobacteria also have specific light harvesting complexes, as a result of the life at low-light conditions[54].

In PSI nearly 50 chlorophylls are in close distance to the electron transport chain and may supply the P700 with excitation energy[34, 35]. In PSII, there are only two chlorophylls in the central domain, maybe because of the high oxidizing potential of P680, which might oxidize any pigments in its proximity[30, 41]. This could explain why the PSI quantum yield is close to unity, while the PSII is about 0.8. Also, PSI has two parallel electron transfer chains that are active, although they work at different rates. In PSII both branches cannot be active simultaneously, since it would take a much longer time to reduce twice the same quinone, increasing the risk of the quinone reducing back the P680[30].

1.1.3.4 ATP synthase

ATP synthase is found in both chloroplast thylakoid membranes and mitochondrial inner membranes. In cyanobacteria and the chloroplast of algae and plants, this enzyme catalyzes the ATP synthesis using the proton gradient generated during the photosynthetic electron transport chain,[55] thus storing the converted energy into a chemical species that can be used elsewhere in the organism. The structure of ATP-synthase is highly conserved between organisms, and is very similar to the mitochondrial ATP synthase[30]. The enzyme is a multisubunit complex divided into two main regions, the stromal region CF_1 where the ATP synthesis takes place at specific sites, and the transmembrane region or CF_0.

1.1.4 Electron Transfer theory

There has been many experimental and theoretical studies to understand biological electron transfer (ET)[25, 56-71] since Marcus[1] introduced the theoretical basis for biological ET.

Marcus theory describes the rate of ET between an electron donor (A) and an acceptor (B) held at a fixed distance in terms of the driving force for the ET reaction ($-\Delta G^o$), the reorganization energy required for ET (λ), and the electronic coupling strength (H_{AB}) between A and B at the transition state:

$$k_{ET} = \sqrt{\frac{4\pi^3}{h^2 \lambda k_B T}} H_{AB}^2 exp\left(-\frac{(\Delta G^o + \lambda)^2}{4\lambda k_B T}\right) \qquad \text{eq. 1}$$

Where k_B and h stand for the Boltzmann and Planck constants, respectively, and T for temperature. H_{AB}^2 describes the probability of electron tunneling in the activated complex, and has an exponential dependence on the distance between donor and acceptor (d_{AB})[1]. The exponential factor reflects the probability of forming the activated complex for the reaction, and depends on $-\Delta G^o$ relative to λ. Thus, when the driving force equals the reorganization energy, the rate for ET has an exponential dependence on d_{AB} (Eq. 2). The key parameter in this relationship is the distance decay factor β, characteristic of the ET mechanism, and the medium between donor and acceptor.

$$k_{ET} \propto exp(-\beta d_{AB}) \qquad \text{eq. 2}$$

In biology, charges travel within and between redox proteins over distances of several nm[72-76], which are longer than the distance covered by a single step tunneling process (up to ~2 nm)[66, 77]. The way to achieve long range ET is to arrange cofactors over long chains, each spaced at a tunneling step distance, so this cofactors can act as intermediators of the overall ET[25, 78]. These intermediators are not necessarily redox cofactors, it has been reported that charges can hop using aminoacids side chains along the protein backbone. In redox ET proteins, multiple ET pathways can exist[79-81], and depend on protein structure and environment.

Several theoretical models have been developed to describe long-range ET in biological ET chains including: Superexchange, charge hopping and flickering resonance mechanism[82] (Figure1.4).

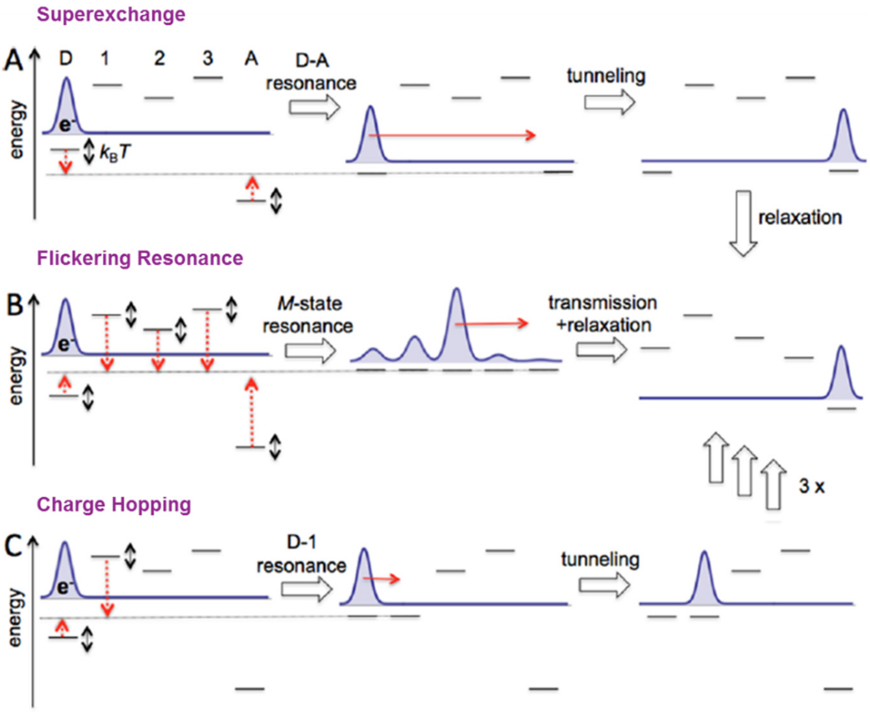

Figure 1.4. Schemes of the different long range ET mechanism models. (A) Superexchange, (B) flickering resonance, and (C) hopping models. First site is the electron donor (D), last site is the acceptor (A), and there are three bridge sites (1, 2, 3). The excess electron is indicated by a Gaussian function, initially localized at site D. In the SE model (A), thermal fluctuations bring D and A levels into resonance, followed by tunneling from D to A. The bridge sites remain off resonance; they only enhance tunneling but are not significantly occupied by the tunneling electron at any time. In the FR model (B) all five levels are assumed to be in resonance before the electron transfers to the acceptor. The bridge sites become partially occupied by the tunneling electron. In the hopping model (C), the donor D and the nearest neighbor bridge site 1 get into resonance, followed by electron tunneling from D to 1. This step is repeated three times until the electron has made four consecutive hops to reach A. Adapted with permission from (Blumberger, J. Chemical Reviews 2015, 115 (20), 11191-11238). Copyright (2015) American Chemical Society.

In the superexchange (SE) mode for ET, electron tunneling between the electron acceptor and donor states is mediated by intermediate states, corresponding to unoccupied states of the medium (bridge). These intermediate states enhance tunneling with respect to vacuum (lowering the activation energy), but are not occupied during the process (the electron does not populate these states). Thermal fluctuations, bring acceptor and donor states into resonance, and the electron tunnels through the intermediated states. Superexchange is a model for direct tunneling, and thus the ET rate depends on distance between donor and acceptor[68]. Alternatively to superexchange ET, hole transfer can also occur via superexchange. In this mechanism, one of the intermediate sites donates an electron to the acceptor and then the electron vacancy (hole) tunnels through the occupied states of the medium. A combination of electron and hole transfer is also possible[68]. SE transfer is predicted to be independent on temperature and this feature has been used to characterize experimentally the ET mechanism in several redox proteins.

In the flickering resonance (FR) model, the medium is no longer seen as a pure bridge, but as a chain of redox states that can accept and donate electrons or holes. The flickering mechanism takes into account the dynamical nature of the system[83] and assumes that the charge transfer occurs when thermal fluctuations align the energy levels of donor, bridge and acceptor. In this case, the transfer rate has an exponential distance dependence as in the superexchange model. Biological ET usually involves aligned multiple groups and redox cofactors, with coupling rates highly sensitive to conformal fluctuations, that could be explained through the flickering resonance model.

In the charge hopping model, charge transfer between donor and acceptor occurs through consecutive hops from site to site, with an associated probability of hopping both forward and backwards. This mechanism shows weak distance dependence and can explain longer ET distances[84].

1.1.5 ET in proteins and applications to bioelectronic devices

ET proteins have unique electrical and chemical properties including selectivity and self-assembly[85]. Many experimental and theoretical approaches have been used to study these systems and to characterize the biological ET in which they are involved. Typically, an intramolecular electron transfer rate would be measured between an electron donor (D) and acceptor (A) site of the protein, which could be either the natural donor and acceptor sites, or some other probes that are artificially implanted (e.g. organic molecules or electrodes). Most of the k_{ET} rates for protein ET have been obtained using flash-quench method[58, 64-67, 86] or pulseradiolysis methods[57, 87]. Based on the measured ET rates it was shown experimentally that the logarithm of the proteins' k_{ET} was proportional to the donor-acceptor distance, with a characteristic distance decay factor β (as shown in eq. 2). The obtained typical β values for proteins were in the range of 10-14 nm^{-1} for ET along β strands and α helices, respectively[58, 88].

Protein ET has also been studied by electrochemical methods, where the protein is assembled in a monolayer onto a working electrode, and the ET rate of the transfer process between the protein redox center and the electrode is measured. Electrochemical methods have been used to study ET in a variety of metalloproteins[56, 89-94] including cytochrome[95], stellacyanin[95], and multicopper enzymes[57].

The special properties of these proteins make them promising candidates for a wide variety of technological applications[96], including energetic[97, 98], biomedical[99-101] and environmental[102] applications.

1.1.5.1 Azurin metalloprotein as a model system to study ET

Pseudomonas aeruginosa azurin (Az) is a 14.6 KDa globular protein that acts as an electron mediator in certain bacterial respiratory chains[13]. It is a cupredoxin protein, with a blue copper center that can switch between two stable redox states (Cu^{1+}/Cu^{2+}). The copper center is located 8 Å below the Az surface and is coordinated by five residues with a distorted tetrahedral symmetry. Az also presents a solvent-exposed disulfide bridge between Cys 3 and Cys 26[14], that can be used to covalently immobilize the protein onto a Au electrode[12, 103-106]. Azurin metalloprotein represents a benchmark for the study of ET in proteins[107].

Many studies of the ET process of Azurin have been performed in solution, using flash-quench methods[58, 64, 108-110] or pulse-radiolysis method[57, 87]. Studies of azurin protein with a Ru redox probe attached to histidine residues at different points of the protein[111] yielded a distance decay factor of $\beta \sim 10 nm^{-1}$, in agreement with previous calculations[79] and in the same range as the one obtained for saturated alkyl chains, suggesting that the ET mechanism was superexchange tunneling in both cases[56, 58].

These experiments were performed in solution. Another approach to study Azurin ET is to immobilize the protein on the surface of an electrode, and study the ET with electrochemical methods[91, 112-119]. This can be achieved either by covalent bond through the native cysteines (or through bioengineered ones) to a gold substrate, or through the creation of a self assembled monolayer (SAM), that covers the working electrode and acts as a linker between the electrode and the protein. SAMs allow simple means of functionalizing the metallic electrode with diverse chemical groups ($-CH_3$, $-OH$, $-COOH$, $-NH_3$) without limiting ET with the solution if the layer is not thicker than eight carbon-carbon bonds[71]. Using different lengths of the SAM, the distance dependence of the ET reaction was studied[61], which confirmed the $\beta\sim10nm^{-1}$ previously reported[71, 120, 121].

Azurin electron transport properties have also been measured in solid state configuration, either sandwiched between two electrodes[122-124], or wired in a molecular junction approach[104, 106, 125-131], The electron transport process of Azurin trapped between two electrodes showed no temperature dependence over the 20-360K range[124], indicating tunneling mechanism. However, when the redox center was modified the temperature dependence changed[84], as well as when the protein H was isotopic exchanged to D[123]. Metal - electrode coupling is the dominant factor for transport, and when the Cu center is modified, it leads to a weakened coupling and thus a less efficient electron transport. The fact that the transport is also affected by deuteration of the protein, indicates that the hydrogen bonding network, by maintaining the specific protein conformation, has an influence in metal-electrode coupling[123]. These experiments were performed in air, which makes them difficult to compare to the results obtained in liquid under electrochemical control[107, 132].

Azurin has shown efficient transport properties along ~3.5 nm, a distance too long for electron tunneling through saturated organic molecules[84]. This long range ET pathway is supposed to be assisted though oxidizable aminoacids like tryptophan and tyrosine along the protein backbone[108].

Azurin redox properties have been further characterized by modifying the protein residues surrounding the copper center, which tuned its electrochemical properties and might be interesting for potential technological applications[133, 134]. Azurin technological potential is already being studied in different applications, such as biomemory[135, 136] and other electronic devices[106, 137].

1.1.5.2 Photosystem I as a promising potential device.

PSI acts as a natural photodiode, allowing electron conduction through the protein complex upon light illumination. Light absorption results in photoexcitation of the P700 center, which is promoted to its excited singlet state (P700*). The excitation of an electron to this high-energy state leaves an electron vacancy (hole) in P700 that also behaves as a charge carrier, but is subject to electric forces of opposite sign when immersed in the same electric field. P700* is rapidly oxidized to P700$^+$, i.e. the high energy electron is transferred to the primary electron acceptor, chlorophyll a (A_0), and then to a tightly bound phylloquinone molecule (A_1). The cofactor chain is completed by three [4Fe-4S] clusters, F_X, F_A and F_B, the terminal electron acceptor of PSI[47]. These electronic states are organized with progressively lower energy as they leave the location of the P700/P700* states, and cause the effective separation of the photogenerated electron toward the Fd bindig site and the photogenerated hole toward the Pc site. The energy transfer efficiency of PSI in this process is close to unity[138].

The organization of the cofactors associated with electron transfer, specially the F_X, F_A and F_B clusters, is quite close to the surface of PSI, which allows rapid ET with Ferredoxin[139]. This surface accessibility to the electron acceptors and donors in the chain can be exploited in the study of ET of PSI and in the employment of PSI for technological applications. All these features make PSI one of the most investigated systems of ET in biology, both because its importance[47] and because its promising applications in biomolecular electronics.

PSI shows a transport efficiency across more than 7nm distance[140], and shows temperature independence over a wide range of temperatures (160-320K)[141]. These results suggest a tunneling based mechanism, but the distance exceed the maximum length for tunneling observed for organic molecules[142]. Also, the photocurrent of a single PSI molecule[143] resulted higher than expectations based on the rates of PSI in solution[144]. Interestingly, light-induced electron transfer through oriented PSI is highly spin selective, with the favourable electron spin being aligned parallel to the biological ET direction in the protein[145].

The integration of PSI into photoelectrochemical devices has attracted a lot of attention. PSI complexes, both from cyanobateria or higher plants, have been applied to photosynthetic energy production involving hydrogen production[98, 146-156] and generation of photocurrents[157-161]. PSI has a quantum efficiency close to unity, but is limited to absorb ~1% of natural sunlight. Carmeli et al.[162] enhanced PSI light absorption capability with the attachment of colloidal gold and silver NPs, which acted as optical antennas. Besides, it has been shown that PSI isolated from cyanobacteria and plants remain photochemically active in solid state over 21 days[163], in aqueous hydrogen producing bioreactor over 85 days[146] and in wet electrochemical cell over 280 days[164].

1.2 SPM to study ET in biology.

1.2.1 Scanning Tunneling Microscopy and Atomic Force Microscopies.

Scanning Probe Microscopies (SPMs) appeared in the year 1981, with the invention of Scanning Tunneling Microscopy (STM)[165]. STM was revolutionary because it offered a resolution below the light diffraction limit and allowed visualizing individual atoms on surfaces. Basically, STM consists in a very sharp conductive probe positioned next to a conductive surface, so close that the electrons can tunnel between the electrodes (sample and probe). When a bias potential is applied between the electrodes, a tunneling current can be measured between them. This tunneling current is recorded by the STM system and used as a feedback mechanism to adjust the distance between sample and probe. When the probe is scanning the sample, in order to keep the tunneling current constant, the STM feedback loop will modify the probe-sample distance when the probe encounters a feature in the surface. The correction of the height is recorded during subsequent scans and the obtained profiles are used to reconstruct a three-dimensional image of the surface of the sample.

STM achieves high resolution but requires the sample surface to be conductive. This requirement was overcome when a variation of STM was developed: Atomic Force Microscopy(AFM)[166]. Essentially, a nanometrically sharpened needle is attached to the end of a (micro)cantilever, whose deflection senses the interaction force at the tip apex. In order to measure deflection, a laser beam is reflected in the back of the cantilever to a photodiode. When the tip is moved around the sample while scanning, the laser beam transduces the protrusions or grooves present in the surface to electrical signals detected in the photodiode.

The development of the SPMs was instrumental for the growth and expansion of the fields of nanoscience and nanotechnology.

1.2.2 Advantages of SPM to study ET in biology

Bulk measurements sometimes obscure the properties of individual molecules[116, 117, 167]. SPMs allow the measurement of small amounts of protein, or even single molecules, in vacuum, air, inert atmosphere or liquid medium. The possibility of working in aqueous media enables studying biological systems in quasi-physiological conditions.

STM in liquid allows the possibility of controlling the electrochemical potential of both electrodes (sample and probe) using a bipotentiostat. The electrochemical STM (ECSTM) works in a four-electrode configuration, where sample and probe act as working electrodes, and a counter electrode and reference electrode are added into the electrochemical cell. The potential of both electrodes are independently controlled by the bipotentiostat. The difference between the probe potential and sample potential define the bias potential ($U_{bias}= U_{probe}- U_{sample}$). Thus, operation of an ECSTM system involves two simultaneous feedback loops (current-distance controlled by the STM and current-potential by the bipotentiostat) and the use of special probes: working in electrolytic media, the probe faradaic current must be minimized below 50pA in order to allow a reliable measurement of the tunneling current. Thus, the probe exposed area must be reduced, by electrically insulating the body of the tip and leaving just the very apex of the probe uncoated[168].

This configuration allows full electrochemical control of the system while offering the possibility of single-molecule resolution, being ideally suited for the study of individual redox biomolecules[12, 71, 105, 169].

One of the strongest points of both ECSTM and AFM is the fact that besides high resolution imaging, they can perform different kinds of spectroscopies, thereby probing different properties of the sample, relating to its electronic behavior, and structural and mechanical properties.

ECSTM can perform spectroscopic experiments at fixed points of the sample surface. Tunneling spectroscopies include current-distance and current-voltage measurements. In current-distance measurements the ECSTM probe can be regarded as a redox probe in solution that is located at different distances along a well-defined axis of the protein[105, 170]. Current-voltage spectroscopy allows us to obtain the conductance characteristics of individual biomolecules. The analysis of the experimental data obtained with the ECSTM provides insights into electron transfer processes at the single molecule level.

AFM imaging in liquid provides information about the topography and structure of a sample and its mechanical properties. An outstanding property of AFM is the possibility to operate in aqueous environments on a wide variety of biological samples, from single molecules such as DNA or proteins to macromolecular assemblies or even whole cells. Among the different modes of AFM, conductive AFM (cAFM) represents an excellent tool to investigate ET through biomolecule junctions. cAFM allows studying simultaneously the mechanical and electronic properties of a molecular junction, characterizing the relationship between the molecule structure and its electronic behavior.

1.2.3 ECSTM and CAFM applied to ET proteins

ECSTM has been used to study of model ET proteins such as azurin[71, 104-106, 112, 137, 169, 171], and cytochrome[172-174], and also to study redox enzymes[175, 176]. ECSTM has shown that the ET process in azurin involves its Cu ion[71, 171]. ECSTM imaging showed that the apparent height of azurin depends on the applied overpotential, which is defined as the redox potential of the molecule minus the applied substrate potential. The maximum apparent height of Azurin is obtained at zero overpotential, that is at its redox potential, indicating that at this point, the ET process is more efficient, which is supported by ECTS measurements[105, 106, 137].

Azurin has also been studied using conductive-AFM approaches[128, 177, 178], which showed that the azurin conductance is dependent on the applied loading force. cAFM have been also applied to study ET proteins like plastocyanin[179] bacteriorhodopsin[180, 181] or photosystem I [141, 182, 183], in non-electrolytic environments.

PSI was also characterized by STM and STS[184, 185], which showed its diode-like behavior, and studied its dependence with respect to the orientation of the molecule on the surface. However, its ET mechanism has not been characterized in an electrochemically controlled environment, like the ones offered by ECSTM.

1.2.4 Current challenges

SPMs have been proven very useful to study biomolecules. ECSTM allows single biomolecule imaging and spectroscopy in quasi-physiological conditions, and controlling the electrochemical potential of the sample (redox ET proteins, in our case, which can be reduced and oxidized at will) and of the probe, which offers a wide potential window to measure tunneling currents and their dependence with potential and distance.

Many ET proteins are suitable for ECTSM imaging and spectroscopy, once they are immobilized on an atomically flat electrode. ECSTM and ECTS have shed light on certain aspects of ET mechanism in ET proteins, but several experimental challenges lie ahead, such as improving the speed of ECTS measurements and their spatial resolution. A reliable and rapid method to obtain the conductance of single molecules at high spatiotemporal resolution would be very useful to characterize multiredox ET proteins or long electron transfer chains.

Another important technical challenge is to use cAFM in liquid environments. This development would allow studying the relationship between the structure of redox proteins and their electronic behavior under full electrochemical control. In order to work in electrolytic environments, the AFM conducting probe requires almost complete insulation except at the very end of the probe apex[186]. Obtaining AFM probes that fulfil this requirement is challenging due to their complex geometry.

These and other technical improvements would help characterizing conduction pathways in redox proteins and protein complexes at the nanoscale, thus providing deeper insights on the ET process in which they are involved. The combination of such experimental data obtained with SPMs with the available atomic-level simulations will lead to a better understanding of cellular bioenergetics and to potential technological applications.

1.3 Objectives

The general objective of this thesis is to investigate electron transfer in redox proteins at the single molecule level. To that end, we use Electrochemical Scanning Tunneling Microscopy (ECSTM) and conductive Atomic Force Microscopy (cAFM), and we focus on two redox protein systems: azurin, a small electron carrier protein and photosystem I, a light-sensitive oxidoreductase protein complex.

In azurin, we aim to study the protein conductance as a function of its redox state and location on the protein surface, which are biologically relevant parameters. We are also interested on the effect of technical parameters such as the contact properties between azurin and the metal electrodes, the mechanical force applied in such contact, and the requirements to improve the resolution of current measurements in ECTS. For the latter, we adapt to our ECSTM setup an alternating current method often used in ultrahigh vacuum (UHV) STMs. The sensing of mechanical force involves developing a methodology that combines AFM-based single-molecule force measurements with single-molecule electrical measurements, while working in an electrochemically controlled environment. For that purpose, the key technical improvement is the design and fabrication of new force probes with electrical insulation against faradaic current.

In photosystem I, we aim to characterize the mechanism of ET at the level of individual protein complexes. To achieve this objective, we first develop a method to immobilize complexes on a substrate suitable for ECSTM like atomically flat gold. In these conditions, we characterize photosystem I by imaging and spectroscopy, and evaluate its conductance and distance-decay properties in a wide range of biologically relevant electrochemical potentials.

2

ECSTM and ECTS of Azurin metalloprotein

2.1 Introduction

Azurin is a blue copper protein that acts as an electron carrier in the respiratory chain of denitrifying bacteria. It contains a Cu redox center that makes the protein capable of accepting and transporting electrons by switching its redox state (Cu I/II). Besides, azurin can be immobilized on single crystal Au <111> surfaces via a dithiol covalent bond, representing a model system to investigate the Electron Transfer (ET) process in redox proteins.

ECSTM is an extremely useful technique for the study of single redox molecules, and it has been widely applied to the study of ET in azurin. No longer after the first STM study of azurin[104], ECSTM imaging studies reported that the Cu center of the protein was the most likely candidate to mediate the ET process[169, 171] and that the voltage dependence exhibited a resonant- like behavior in agreement with a multistep tunneling process[71, 112].

Beyond imaging, ECSTM can be also used to probe local electronic properties of the sample by studying the tunneling current and changing the distance between the electrodes or the electrochemical potentials applied to the system[170, 187]. Current-distance spectroscopies of azurin molecules and ECSTM break junction (ECSTM-BJ) technique have been applied to the study of azurin on gold under bipotentiostatic in our group prior to this thesis[105, 106]. Here we performed current-voltage tunneling spectroscopy of azurin protein, both in tunneling and “wired” configurations, and studied the transition voltage related to the tunneling barriers of the ET process.

The experiments included in this chapter were initiated by Juan Manuel Artés as the final project of his Ph.D. thesis, and were completed by Montse López-Martínez during her training stage.

2.2 Experimental methods

Chemicals and materials

Azurin and all reagents were purchased from Sigma. Buffer solution was 50 mM Ammonium Acetate buffer (pH 4.55). All solutions were prepared using Milli-Q water of 18 MΩ · cm, and were bubbled with Ar right before performing the experiments.

Electrode preparation.

The Au electrodes used where Au <111> single crystals (Mateck GmbH). The electrodes were prepared using reported protocols[188]. To clean and ensure a <111> surface of the single crystals they were flame annealed with a butane flame for 3 minutes. Then they were let to cool under an Argon stream. The crystal surface was then electropolished by applying 10 V in a H_2SO_4 0.1 M solution for 30 seconds. The superficial Au oxide was removed by immersion of the electrode in HCl 1M for 2 minutes. The electrode was then rinsed with abundant Milli-Q H_2O to remove the rests of HCl. The immersion in HCl and posterior rinsing was performed twice, to ensure the elimination of any Au oxide rests. Finally, the crystal was flame annealed again for 3 minutes and let cool down under an Argon stream.

Azurin incubation.

Protein solution was incubated on the electrode surface for a minimum of 2 hours, following reported protocols to attach azurin on gold[104] through native cysteines Cys3 and Cys26, which results in a defined orientation of the protein on the surface, while preserving its native-like conformation[189] and electrochemical properties[12, 103].

ECSTM measurements.

ECSTM imaging was perform in a PicoSPM microscope head and a PicoStat bipotentiostat (Molecular Imaging) controlled by Dulcinea electronics (Nanotec Electronica). A homemade electrochemical cell was used in four electrode configuration, using a Pt:Ir (80:20) wire as counter electrode and a miniaturized ultralow leakage membrane Ag/ AgCl (SSC) reference electrode filled with 3M KCl. The potentials of the gold electrode sample (U_S) and ECSTM probe (U_P) are expressed against this reference. Pt:Ir ECSTM probes were prepared as described[168]. Data were acquired and analyzed using WSxM 4.0 software[190].

For the current voltage measurements, the probe was stopped at a current setpoint of 0.5nA, and the STM feedback was briefly turned off during the application of a 0.5V symmetric ramp to U_P. The difference between the initial setpoint current and its value at the end of the ramp (upon restoring the initial U_P, prior to resuming feedback) was taken as a measure of the vertical drift of the probe during the tunneling I-V recording. Curves were automatically discarded if the deviation was higher than 10%. For current-voltage measurements performed with the "wired" configuration, we performed current-time recordings to spontaneous single wired protein junctions. In this case, after bringing the probe to tunneling distance to the substrate, the STM feedback was turned off and the current was recorded as a function of time. When a molecule bridges probe and sample electrodes, a sudden "jump" or "blink" in the current is detected (I_{blink}). When an azurin bridge was detected, a potential ramp was automatically triggered and applied to U_P, while the current signal was recorded.

TVS representations were obtained by two alternative methods. I-V reference curves (with the ECSTM probe far from the surface) were subtracted from the individual I-V curves in tunneling regime to remove electrochemical background currents as previously described[170]. Curves were then smoothed using an adjacent averaging method with a 5000 points window. The obtained smoothed data was used to produce the TVS representation (Ln (I/V^2) vs 1/V). In an alternative approach, the numerical version[191] of the 2-step ET formalism[62] was used to fit individual I-V. The resulting equation was then represented in the TVS context (Ln (I/V^2) vs 1/V). The minima found in the plots correspond to the TV in each case.

2.3 Results and Discussion

2.3.1 Current-Voltage Characteristics.

Current-bias voltage measurements were carried out in tunneling configuration, where there is no physical contact between the STM probe and the protein, and in “wired” configuration, where the azurin is in direct contact with the protein. In tunneling configuration, the tip is positioned within tunneling distance to the sample. When the tip is stable, the feedback mechanism is briefly switched off, and a potential ramp is applied to the tip (Figure 2.1). For the wired configuration, we use the current- versus time technique, to create spontaneous molecular junctions. We monitor the current, and when a current step is detected, a potential ramp is applied to the tip.

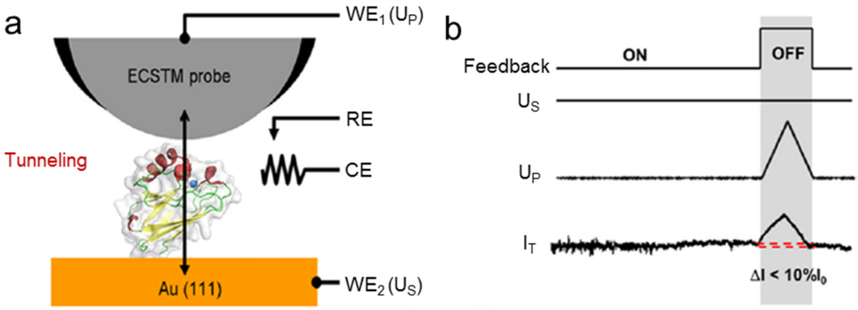

Figure 2.1. a) Experimental setup scheme (Azurin structure PDB: 1jzf). b) Example of IV recording. A triangular ramp was applied to the probe (WE$_1$(U$_P$)) while the feedback loop was off. Sample potential (WE$_2$ (U$_S$)) was kept constant. Adapted with permission from reference [192] (*Artés et al. 2012*). Copyright (2012) American Chemical Society.

In the current -bias voltage measurements we see two types of curves: one population with current-rectifying behavior and other population with a linear/non-rectifying behavior (Figure 2.2). In absence of Azurin molecules, all the curves showed a linear behavior, thus we attribute the current-rectifying curves to the Azurin protein. The rectifying behavior depends on the sample potential (the redox state of azurin) and is in agreement with the metalloprotein electrochemical behavior[105, 137, 169, 177]. At $U_S = -0.3$ V, most of the molecules are in a reduced state, and efficient electron withdrawal from the Cu^+ center to a positively biased probe occurs (Figure 2.2). At $U_S = 0.2$ V, azurin is oxidized, and the most efficient process is electron injection into the Cu^{2+} center from a negatively biased probe[105] (Figure 2.3).

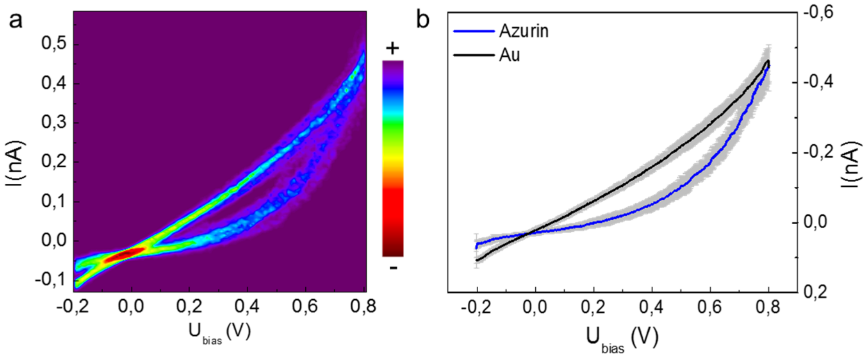

Figure 2.2. a) 2D I–V histogram showing the IV curves obtained in a sample of azurin on Au. $U_S = -0.3$ V (reduced azurin); initial $U_P = 0.5$ V; current set point = 0.5 nA; N = 50. (b) Average of the two I–V populations identified in (a), corresponding to azurin (blue) and Au (black). Gray error bars indicate standard deviations.

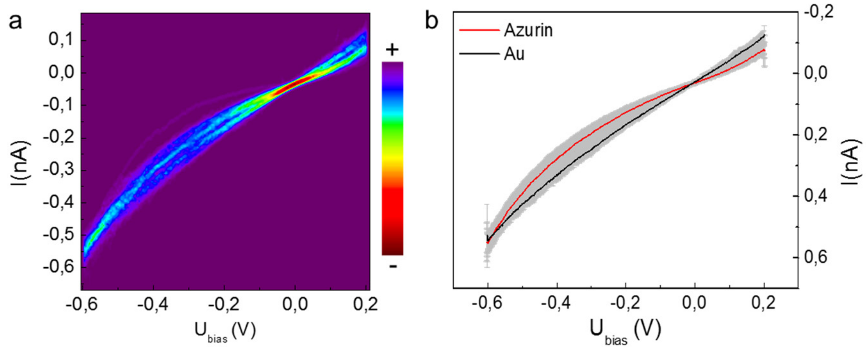

Figure 2.3. a) 2D I–V histogram showing the IV curves obtained in a sample of azurin on Au. $U_S = 0.2$ V (oxidized azurin); initial $U_P = -0.4$ V; current set point = 0.5 nA; N = 50. (b) Average of the two I–V populations identified in (a), corresponding to azurin (red) and Au (black). Gray error bars indicate standard deviations.

From the IV curves, we can calculate the conductance (G) of the tunneling gap using the relation $G = I/U_{bias}$. From the IV curves obtained in the presence of Azurin, the conductance was between 10^{-6} G_0 and 10^{-5} G_0. ($G_0 = 2e^2/h = 77\mu S$ conductance quantum), in agreement with the reported conductance of azurin[106].

Using reported procedures[193], we calculated the transition voltage (TV) value for azurin conductance from the IV curves. The TV value helps to describe the dependence of azurin conductance with the electrochemical potential[193]. Although it cannot be physically interpreted in the same terms as for small molecules confined between metal electrodes that undergo coherent electron transport [142, 193, 194], it is useful for the sake of comparison. The Azurin transition voltage spectra (TVS) showed minima values distributed around 0.4 V (Figure 2.4), lower than the ones found for other single molecules[193, 194], but on the same order as the ones reported for porphyrin dimers measured in air [195]. This low TV value suggests that the effective barrier for tunneling through a solution is lower than the barrier found in pure tunneling processes (tunneling through vacuum).

This is in agreement with experimental and theoretical works on tunneling through an electrochemical environment[187, 188, 196-198]. In the context of two-step ET in a redox molecule, a transition was predicted by theory to occur in the range where the effective voltage in the redox center is higher than the reorganization energy of the molecule[61].

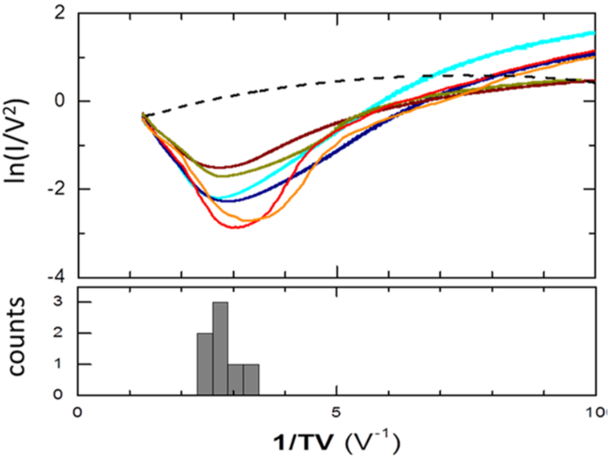

Figure 2.4. TVS representation of smoothed raw-data I−V curves of azurin for U_S = −0.3 V and initial U_P = 0.5 V. The dashed line shows the average I−V curve for the Au control. The TV is the voltage where the plot displays a minimum. (b) Histogram showing the distribution of the minima of the plots in (a), which is centered at 0.37 ± 0.03 V. ECTS recordings obtained M. López-Martínez, figure prepared by JM Artés [and included in this chapter for completeness]. (Reproduced with permission from reference [192] (*Artés et al. 2012*). Copyright (2012) American Chemical Society[192])

The TVS can be used to obtain values for the various parameters describing the ET process. We fit our experimental data to the numerical version of the Kuznetsov-Ulstrup formalism for adiabatic two-step ET with partial vibrational relaxation[120, 191]:

$$I_T = 1820\kappa U_{bias}\left\{exp\left[\frac{9.73}{\lambda}(\lambda + \xi\eta + \gamma U_{bias})^2\right] + exp\left[\frac{9.73}{\lambda}(\lambda + U_{bias} - \xi\eta + \gamma U_{bias})^2\right]\right\}^{-1} \quad \text{eq. 1}$$

In which κ is the electronic transmission coefficient, $U_{bias} = U_P - U_S$ is the potential difference between probe and sample electrodes; λ is the reorganization energy; η is the overpotential, given by $\eta = U_S - U_{AZ}$, where U_{AZ} is the redox potential of an azurin molecule; and γ and ξ are two model parameters describing the shifts in U_{bias} and η at the redox center, respectively. The parameters γ and ξ are related to the electronic coupling of the molecule with the probe and the substrate, respectively. The fitting parameter values are summarized in Table 1.

	tunneling		wired
Sample Potential U_S (V/SSC)	-0.3	0.2	0.2
Transition Voltage (V)	0.38 ± 0.18	-0.42 ± 0.08	-0.06 ± 0.01
Reorganization energy λ	0.56 ± 0.13	0.60 ± 0.13	0.90 ± 0.40
Probe Coupling γ	0.16 ± 0.04	0.11 ± 0.02	0.92 ± 0.15
Substrate coupling ξ	0.74 ± 0.22	0.75 ± 0.28	0.64 ± 0.45
Transmission Coefficient κ	0.8 ± 0.3	0.9 ± 0.2	0.7 ± 0.4

Table 1. Average Values Obtained from Fits of the Experimental I−V Curves to the Two-Step ET Model

Numerical simulations of the TVS representation of the two step ET formalism show that the stronger modulator of the TV is the electronic coupling with the ECSTM probe electrode. The TV diminishes when the probe coupling increases, indicating that the TV is related to the limiting energy barrier in the ET process.

In the tunneling configuration, the TV is related to the tunneling barrier developed through the liquid gap between the molecule and the STM probe, as described by the distance decay factor $\beta \approx C \cdot TV^{1/2}$, with $C = 1.05$ $Å^{-1}$ $V^{-1/2}$ [193]. This expression yields $\beta \approx 0.66$ $Å^{-1}$, in good agreement with the value obtained for azurin under the same experimental conditions by current–distance electrochemical tunneling spectroscopy ($\beta = 0.5 \pm 0.1$ $Å^{-1}$)[105].

We also examined the TVS spectra corresponding to IV measurements of azurin in a wired configuration, where the STM probe is transiently bound to the protein[106] using the I-t method[199]. In ~50% of the IV recordings, a minimum was found in the negative branch that corresponded to a very low TV (-0.06 ± 0.01 V), as predicted by the numerical simulations. The lower TV value reflects the stronger coupling with the probe electrode, which lowers the energy barrier between the levels of the STM probe electrode and the molecule. The dependence of the TV value with the configuration (tunneling or wired) of azurin is an indication that the contact geometry of the electrodes and the molecule dramatically affects the measured TV[193, 195, 200].

TV marks the transition between two conductance regimes that are in agreement with the biological activity of azurin: exchange and transport charges. These results suggest that biological ET could be modulated by the electronic coupling between redox partners, a concept that has been studied using electrochemical approaches[201].

2.4 Conclusions

We performed the first I–V measurements and TVS data for a redox protein under potentiostatic control. In the tunneling configuration, the azurin conductance revealed a transition with a TV value as low as 0.4 V, in agreement with studies of porphyrins in air[195]. The observed TV is consistent with previously measured distance decay factors for azurin in electrochemical environments[105]. The ultralow TV values obtained in the wired configuration show that electrode coupling is particularly optimized in the case of single-azurin junctions.

Charge storage[202] occurs in the weak coupling configuration, and charge transfer is favored with strong coupling. From a biochemical perspective, these regimes are reminiscent of the two basic functions of azurin: to carry and exchange charge in ET chains. We have found that the TV is strongly regulated by the electronic coupling of the protein with the STM probe.

In this study, azurin was immobilized, exposing the surface involved in the transient ET reactions with partner proteins under physiological conditions. Thus, these results suggest the intriguing possibility of gating between the two conductance regimes by varying the electronic coupling between the proteins, for example through the proximity of redox centers and protein-protein recognition[58, 203].

3

Differential Conductance Imaging with ECTSM

3.1 Introduction

As we have seen in the previous chapter, Electrochemical Scanning Tunneling Microscopy (ECSTM) is an excellent tool to study electronic materials and redox molecules including proteins. Besides imaging, ECSTM spectroscopic modes provide a wide amount of information. In particular, current voltage tunneling spectroscopy, provides the local differential conductance of the sample in electrochemical media. However, it has several technical drawbacks: the feedback must be briefly switched off to fix the distance between probe and surface during the potential ramp. In this interval, the probe is vulnerable to drifting and crashing. The application of fast potential ramps can also break down the probe insulation. In addition, a large number of I-U curves must be collected, processed and statistically averaged to obtain statistically meaningful results.

In this chapter, we adapted the current-voltage spectroscopy mode of ECSTM to include a sinusoidal voltage modulation to the STM tip and current measurement by means of a lock-in amplifier. The lock-in amplifier renders the derivative of the current-potential curve (dI/dU), which is proportional to the local density of states (LDOS)[204] of the studied surface. We can use this signal to construct a differential conductance image as we scan the surface, getting simultaneously a differential conductance image and the traditional topographic one. This method provides a direct, spatially resolved measurement of the differential conductance of single molecules.

We validated and optimized this method using an iron electrode, whose reversible oxidation in borate buffer is well characterized[170, 205]. We then applied Differential Electrochemical conductance (DECC) imaging to gold Au <111> surfaces coated with Azurin protein, which revealed regions with different conductance within the protein that bears relevance both for biological ET mechanisms between metalloproteins and for their integration on bioelectronic devices[106, 137, 206].

3.2 Experimental methods

Chemicals and materials

Azurin and all the reagents were purchased from Sigma. Buffer solutions were 0.3 M Sodium Borate buffer (pH 7.5) for the Fe electrode measurements, 50mM Ammonium Acetate buffer (pH 4.55) for the Azurin measurements. All solutions were prepared using Milli-Q water of 18 MΩ · cm, and were bubbled with Ar right before performing the experiments.

Sample preparation.

Fe electrode was a polycrystalline iron disk 99.99%, 0.3 mm thick and 10 mm diameter. The electrode was mechanically polished with silicon carbide polishing papers of 9-, 3- and 1-µm particle size, and 0.3-µm aluminum oxide power. Between each polishing step, the iron surfaces were rinsed with Milli-Q water. Au electrodes used were Au <111> single crystals (Mateck GmbH). Electrode preparation followed the same procedure as in chapter 2.

Protein incubation.

Protein solution followed the same procedure as chapter 2.

ac-ECSTM measurements.

All imaging experiments were carried out with our local ECSTM setup, described in chapter 2. Data were acquired and analyzed using WSxM 4.0 software[190]. STM probes were prepared by an electro-sharpening process previously described[168]. All the glass material used for the preparation of solutions as well as the electrochemical cell were previously cleaned with piranha solution 7:3 H_2SO_4/H_2O_2 (CAUTION: Piranha is extremely dangerous and should be used with extreme precaution). The ECSTM setup was modified by introducing an *ac* modulation to either the probe or sample potential. Both the *ac* signal generator and the lock-in amplifier are integrated in the Dulcinea control system. Tests were also performed with an external SR530 dual-phase lock-in amplifier (Stanford Research Instruments, Sunnyvale, CA), obtaining similar results. The STM feedback circuit was active through the whole measurement. During DECC image acquisition, the phase of the *ac* signal is maintained equal to zero, to ensure that most of the signal recorded corresponds to the resistive (real) part of the signal. For Fe/FeO imaging, an *ac* modulation of 25 mV amplitude at 1 kHz was applied to the probe potential. For the metallic state, potentials were U_S =-900 mV U_P= -950 mV. FeO oxide layer was grown keeping the sample potential at U_S = -600 mV for 5 minutes. FeO images were obtained at U_S =-400 mV and U_P= -950 mV. All Fe/FeO images were taken at 500 pA setpoint, with a scan frequency of 0.5 Hz. Topographic images were plane-subtracted but conductance images shown are raw data. For Az/Au imaging, *ac* modulations of 25-50 mV amplitude and 1 kHz were applied to the probe potential. Alternatively, *ac* modulations of 25-50 mV amplitude and 3 kHz were applied to the sample potential. Potentials were kept at U_S = 200 mV and U_P=-100 mV. All images were acquired at 1 nA setpoint, with a scan frequency of 0.5 Hz. All the images shown for this system were substracted a plane.

3.3 Results and Discussion

3.3.1 Experimental setup for differential electrochemical conductance recordings.

The experimental setup is based on an electrochemical scanning tunneling microscope (ECSTM) that has been modified to simultaneously record the topography and differential electrochemical conductance (DECC) of the sample.

To measure the local conductance, an alternating current (*ac*) modulation was added to the bias potential between probe and sample ($U_{bias} = U_P - U_S$). Consequently, the tunneling current is modulated with amplitude proportional to the first derivative of I/U. This amplitude can be retrieved by means of a lock-in amplifier. The differential conductance signal is simultaneously acquired with the topographic data and can be used to construct a differential conductance image that is displayed in real time during normal imaging (i.e. without turning the feedback off, whose bandwidth is below the employed *ac* frequencies).

The bias can be modulated via either the probe and sample potentials. As the probe is virtually grounded in our setup, to modulate the probe potential (U_P), the *ac* signal must be applied through a virtual channel that in fact applies the *ac* signal simultaneously to the sample and the potentiostatic loop, resulting in a modulation of the bias, that maintains the sample electrochemical potential constant (Figure 3.1). The potentiostatic loop has a bandwidth limitation of 1 kHz, which can represent a limitation to our setup. As can be seen in Figure 3.2 (red plot), an input sinusoidal signal of 100 mV applied to the probe was reduced at 100 Hz and severely attenuated at 1 kHz. In an attempt to overcome this limitation, we modified the setup to test the alternative configuration, by adding the *ac* modulation to the sample potential (U_S) as indicated in the experimental scheme of Figure 3.3. With this setup, frequencies up to 3 kHz could be used without amplitude attenuation, as shown in Figure 3.2(blue plot).

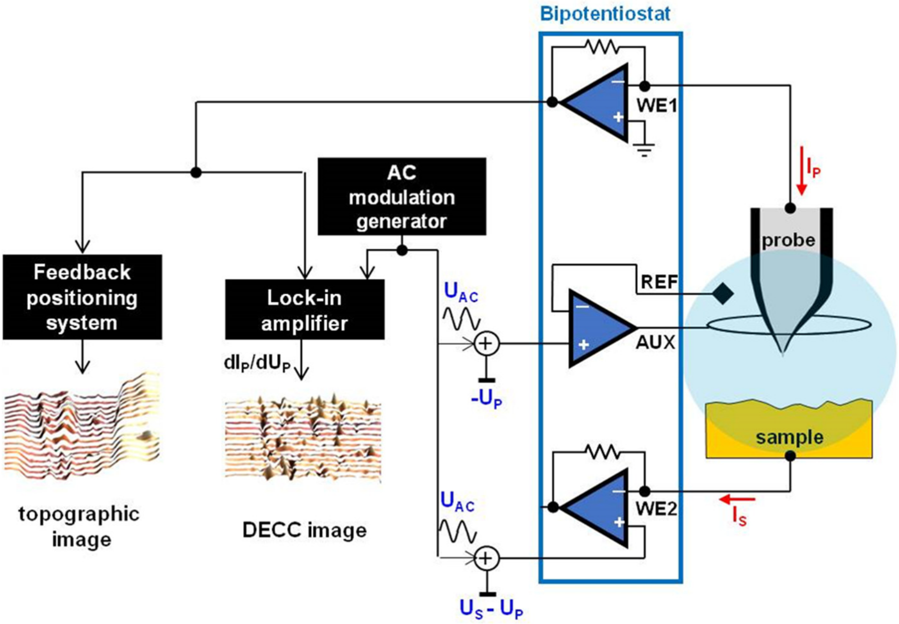

Figure 3.1. Scheme of the ac-ECSTM setup. A sinusoidal potential is applied simultaneously to the sample potential (U_P) and the potentiostatic loop, thus modulating the bias and the tunneling current flowing between probe and sample (I_P). The differential conductance dI_P/dU_{bias} is retrieved by the lock-in amplifier and used to construct differential conductance images that are simultaneous to the topographic images and can be correlated with them.

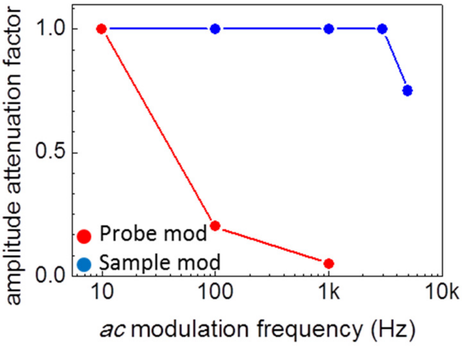

Figure 3.2. Amplitude attenuation of a sinusoidal signal of 100 mV applied at different frequencies to the probe and sample configurations (red and blue plots, respectively).

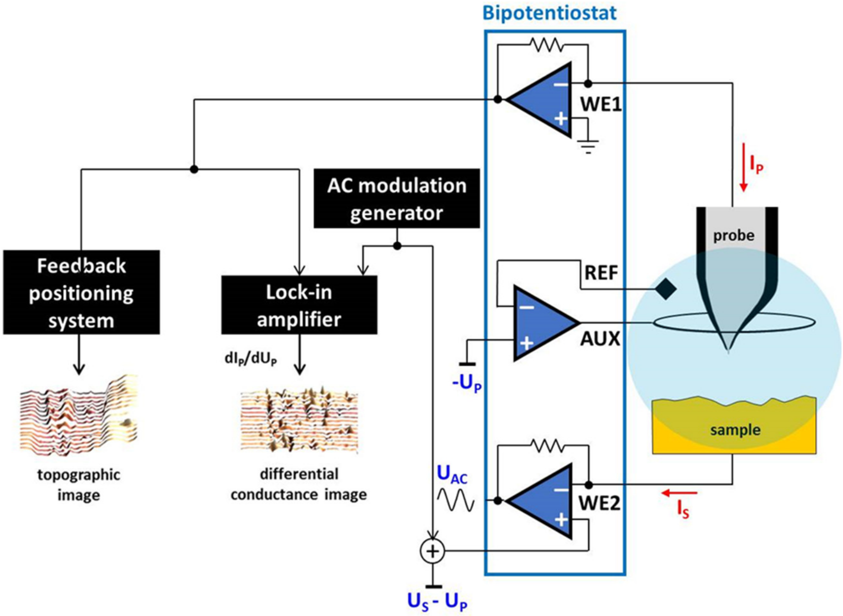

Figure 3.3. Scheme of the ECSTM setup configured to measure the local conductance by means of an ac modulation applied to the sample potential (U_S), thus modulating the bias and the tunneling current flowing between probe and sample (I_P). The differential conductance dI_P/dU_{bias} is retrieved by the lock-in amplifier and used to construct differential conductance images that are simultaneous to the topographic images and can be correlated with them.

The wider bandwidth of the sample modulation setup is convenient to apply higher frequencies and thus to integrate lock-in signals in shorter time, potentially enabling faster STM scanning rates and lower noise conductance measurements in certain cases. However, it has drawbacks like the lack of locality and the potential disturbance of redox processes on the sample surface.

To compare the performance of probe and sample potential modulation in DECC imaging, we used the highest frequency for which reproducible DECC imaging could be attained (1 kHz and 3 kHz applied to the probe and sample, respectively) and we compared several U_{ac} amplitude values. For all amplitudes, conductance imaging displayed better stability and lower noise using probe modulation. The results were consistent among different probes and scan rates. The correlation between topographic and DECC images can be quantified by Pearson's coefficient, which ranges between -1 to 1, being 1 for two perfectly correlated images, -1 for inversely correlated images, and 0 for images that are not correlated[207]. Pearson's coefficient improved at higher applied ac amplitudes to the sample, but still was worse than the results obtained with probe modulation (Figure 3.4). Thus, sample potential modulation seems to perturb excessively the system, despite offering a wider bandwidth. These perturbations affect the probe, which cannot remain steady and properly track the sample topography. In contrast, modulating the probe potential, higher correlation coefficients are obtained with lower perturbation amplitudes in the system.

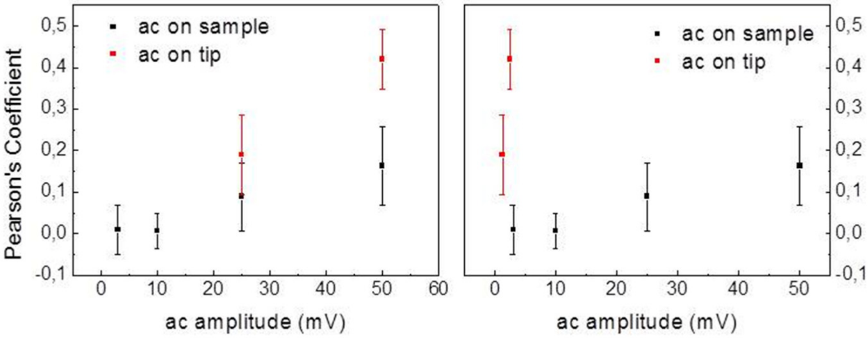

Figure 3.4. Plot of the Pearson's correlation coefficient between topography and conductance images as a function of the modulation amplitude applied to the probe and sample (left panel) and actual modulation amplitude obtained at each electrode after circuit attenuation (right panel). Note that a 1 kHz signal was applied to the probe and a 3 kHz signal to sample.

3.3.2 Conductance imaging of reversibly oxidized iron surfaces.

We first used DECC imaging to study the reversible oxidation and passivation of an iron electrode in borate buffer, a widely-studied system whose local conductance had been characterized previously with ECTS[170, 208]. This system offers the advantage of reversibly toggling between different oxidation states of the electrode surface by setting the sample potential in situ. In Figure 3.5, a cyclic voltammogram of iron displays current peaks that mark two different potential ranges. At potentials below the peak (green region in Figure 3.5) the electrode surface is in its reduced state (Fe (0)) and has metallic properties[170, 208]. At potentials above the peak (orange region in Figure 3.5), the electrode is oxidized and a mixed Fe(II)/Fe(III) oxide layer is formed on the surface that has semiconducting properties[205].

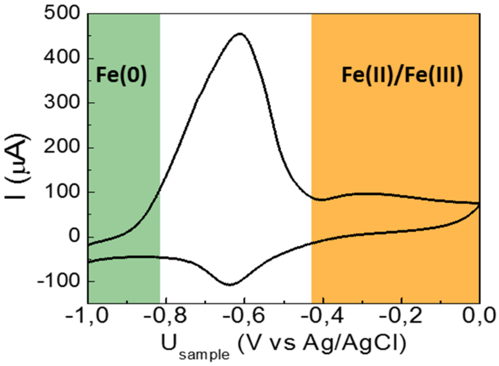

Figure 3.5. Cyclic voltammetry of the iron electrode in borate buffer. The green region indicates the potential range corresponding to the reduced Fe (0) state, and the orange region marks the oxidized Fe(II)/Fe(III) state.

Using the ECSTM described in Figure 3.1, we obtained topographic and DECC images of the electrode surface in each potential range, corresponding to reduced iron (Figure 3.6a) and to the oxidized metal (Figure 3.6b). At 500 pA setpoint current, the oxide film displays a similar topography to the metallic one but deposits up to 100 nm of size are occasionally found in the images. DECC images in the right panels of Figure 3.6a and Figure 3.6b are obtained from the output signal of the lock-in amplifier during the application of 25 mV modulatory potential amplitude at 1 kHz to the STM probe potential. DECC images appear as 'flat' images (i.e. having nearly uniform conductance), with a faint reflectance of topography. However, the differential conductance of metallic surfaces is significantly higher than that of oxidized surfaces (compare the right panels of Figure 3.6a and Figure3.6b). The distribution of differential conductance values (lock-in amplitudes from DECC images) is shown in the histograms of Figure 3.7 for the two redox states. The average conductance (peak of the green histogram in Figure 3.7) is 2.54 times higher than the one obtained from the Fe(II)/Fe(III) semiconductor surface (orange histogram in Figure 3.7). This result is in very good agreement with the conductance ratio of 2.44 obtained in the same system by ECTS[170], calculated from the slopes of I-U_P curves for U_S=-900 mV (Fe(0)) and U_S=-400 mV (Fe(II)/Fe(III)), both at U_P=-950 mV.

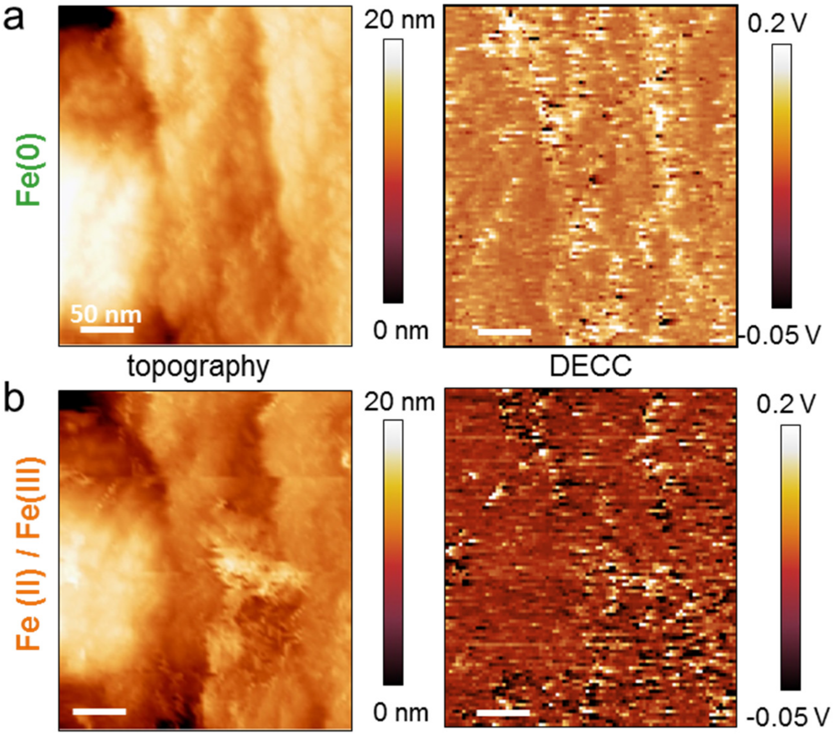

Figure 3.8. a) and b) Simultaneous topographic and DECC (dI/dU) images of the reduced and oxide surfaces, respectively. Metallic images were obtained at U_S =-900 mV, U_P= -950 mV; oxide images were obtained at U_S =-400 mV, U_P= -950 mV. All images were acquired at 500p A setpoint with an ac modulation applied to the tip potential of 25 mV amplitude and 1 kHz frequency. Scale bar corresponds to 50 nm. Both DECC images (right) show a reflection of topography, but indicate that the measured conductance is rather uniform over the surface.

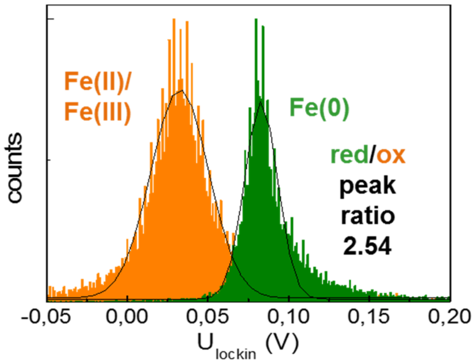

Figure 3.7. Histogram of the differential conductance values corresponding to the two redox states

3.3.3 DECC imaging of Azurin on atomically-flat gold surfaces.

After obtaining differential conductance images under bipotentiostatic control, we studied a biomolecular redox system: Azurin on atomically flat gold surfaces. Previous ECTS studies of the Azurin-Au(111) interface showed that the protein displays current rectification, in contrast with the gold ohmic behavior[192]. Thus, the topographic and electrical properties of this system make it a good candidate to obtain spatially resolved differential conductance images at high resolution.

Figure 3.8 shows simultaneous topographic and DECC images of individual Azurin molecules on an atomically flat gold terrace, obtained by applying ac modulation amplitudes of 25 mV (Figure 3.8a) and 50 mV (Figure 3.8b) at 1 kHz applied to the STM probe potential. The comparison between Figure 3.8a and Figure 3.8b shows that DECC images can be better resolved at 50 mV. The conductance of bare gold and Azurin regions can be calculated from the average of lock-in values in those regions in DECC images (the corresponding histograms of $U_{lock\text{-}in}$ are shown in Figure 3.9a) divided by the amplitude of the modulation potential U_{ac}. The resulting differential conductance ($G_{ac} = U_{lock\text{-}in}/U_{ac}$) is plotted in blue in Figure 3.9b and yields similar values at 25 mV and 50 mV. Note that in the conditions used to record the topographic and DECC images (tunneling current feedback at 0.5nA, U_P=-100 mV and U_S=200 mV, U_{bias}=-300 mV, $G_{dc} = I_{tunnel}/U_{bias}$ =0.55±0.27 nS[106]) the differential conductance of Azurin appears higher than that of gold. This result is probably due to the different I-U relationships displayed by gold (ohmic) and Azurin (nonlinear), which yield higher dI/dU slopes for the latter[192].

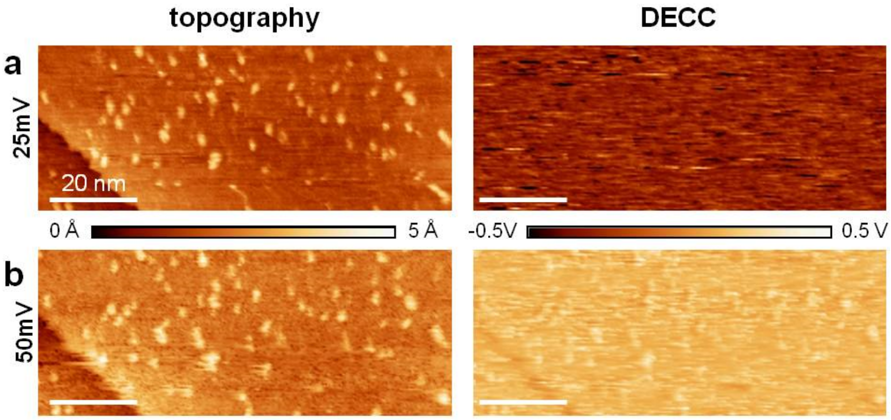

Figure 3.8. Simultaneous topographic (left) and DECC images (right) obtained by ECSTM at different ac modulatory amplitude applied to the probe: 25 mV (a) and 50 mV (b), both at 1kHz. Scale bar corresponds to 20 nm.

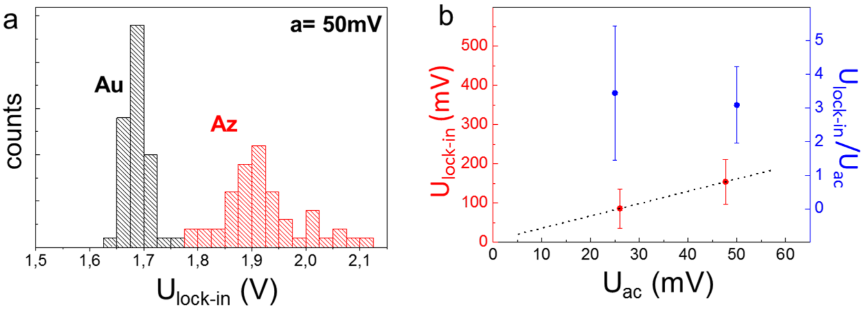

Figure 3.9. a) Histogram of the lock-in values of 50 random Az molecules (red) and the lock-in values of 50 pixels of background (black). All values were obtained from the same unprocessed image (ac amplitude of 50 mV applied to the probe). b) Taking 40 images of 50 nm x 50 nm, the average of lock-in values of Az molecules given in mV (red dots, left axis) is proportional to the modulatory amplitude (25 mV and 5 0mV) and yield similar ratio values (corresponding to the unit-less conductance; blue dots and right axis).

We further analyzed the effects of the scanning direction in DECC images. Figure 3.10 shows topographic images (at 1 nA current setpoint) and DECC images (at 50 mV modulatory amplitude) corresponding to the forward (Figure 3.10a) and backward (Figure 3.10b) directions of subsequent probe scans over the same line on the sample surface. In forward scans, the probe oves from left to right in the image, and in backward scans it goes from right to left.

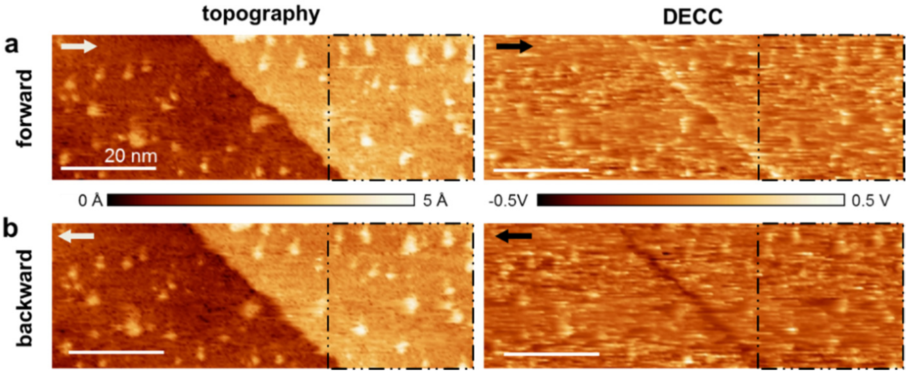

Figure 3.10. Simultaneous topographic (right) and DECC (left) images, obtained with the probe potential modulation configuration (50 mV, 1 kHz, 1 nA setpoint, U_P = -100 mV, U_S= 200 mV). Forward (a) and backwards (b) scan directions are presented.

The correlation between topographic and DECC images was quantified through the Pearson's co-localization coefficient, which ranges between -1 to 1, being 1 for two perfectly correlated images, -1 for inversely correlated images, and 0 for images that are not correlated[207]. Figure 3.11a and Figure 3.11b display an example of co-localization test to a 25 nm x 25 nm region indicated in Figure 3.10a and Figure 3.10b. Figure 3.11a displays the scatter plots of the co-localization between topography and DECC images for the forward (black) and backward (red) directions. The linear adjustment of this scatter plots (blue for forward direction, red for backward direction) give the Pearson's coefficient. Figure 3.11b shows the co-localization map for the forward topography and DECC images, where both images are superimposed and the co-localized spots are highlighted in white.

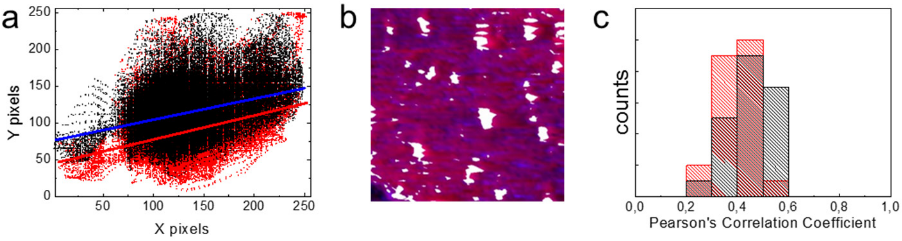

Figure 3.11. a) and b) show an example of quantification of the correlation of topographic and ac conductance images. a) scatter plot for the co-localization topography-DECC for the forward (black dots, blue lineal adjustment, Pearson's coefficient 0.327) and the backward (red, Pearson's coefficient 0.340) directions. b) colocalized pixel map for the 30x30 nm area indicated in Figure 3.10a image. c) Histogram of the Pearson's correlation coefficients calculated from 40 images with a 50 x 50 nm^2 area, for both forward (black) and backward (red) scans.

The correlation between topographic and DECC images is not affected by the scanning direction, as indicated by the similar distribution of Pearson's coefficients in pools of forward and backwards images (Figure 3.11). However, differences in the lock-in response between forward and backward scans can be seen at gold monatomic steps. An increase in differential conductance along ascending steps is observed in forward images (Figure 3.10a) whereas the conductance is reduced in backwards images, corresponding to descending steps (Figure 3.10b). Although electronic changes in the LDOS[209] and in the work function[210] have been reported at topographic steps, the main cause of these features is probably mistracking of the STM feedback system. When the probe is scanned over a descending step, the distance between probe and sample (tunneling gap) may transiently increase due to a delayed feedback response, which decreases the tunneling current and the differential conductance. Conversely, the probe-sample distance may transiently decrease in ascending steps. This effect has been reported in solid semiconductor substrates[211]. Interestingly, it is not observed in Azurin proteins, which always appear as elevations in topographic and DECC images.

In DECC images with a size of hundreds of nanometers (e.g. Figures 3.8 and 3.10), Az molecules appear as bright spots over the gold surface. At higher magnification, imaging of individual proteins revealed sub-molecular conductance features. Figure 3.12 shows high resolution topographic and DECC images of a single Az protein. A bright, high differential conductance spot near the center of the protein can be observed, surrounded by a lower conductance region. The high conductance spot appears at the same position in both scan directions (Figure 3.12a and Figure 3.12b), which rules out artifacts related to the topography or feedback mistracking. The higher differential conductance of Az with respect to the gold substrate may be due to the nonlinear I-U characteristics of the protein, as discussed above[212].

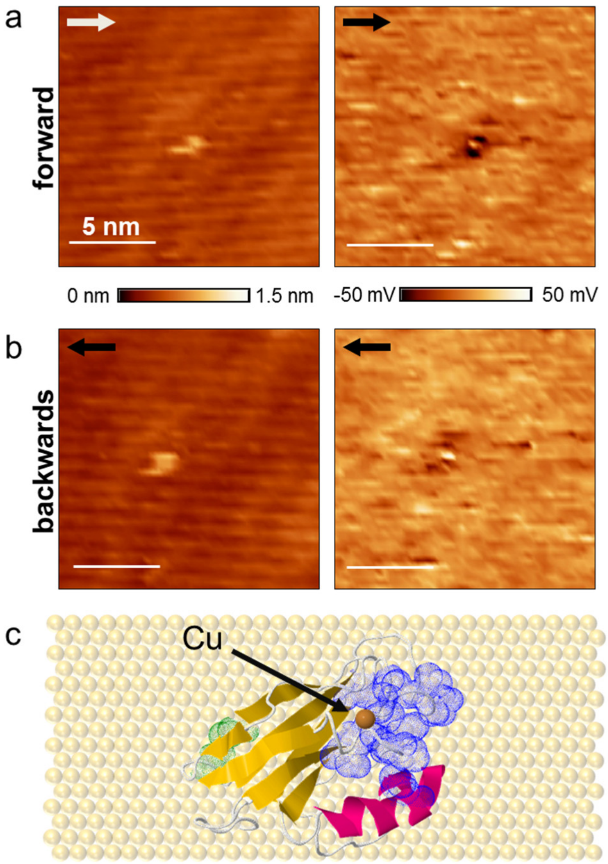

Figure 3.12. Simultaneous high resolution topographic and DECC images (left and right, respectively), obtained with the ac modulation applied to the probe (50 mV, 1 kHz, 1 nA setpoint, U_P = -100 mV, U_S= 200 mV). Scale bar, 5 nm. Forward (a) and backwards (b) directions are presented. A single Azurin protein is present and displays a sub-molecular spot with high differential conductance surrounded by a lower conductance region. c) Top-view representation of an Azurin protein (PDB: 1AZU) on an atomically flat gold (111) surface, according to a previously published model [213]. The protein is bound to the surface through a pair of cysteine residues (indicated in green) and exposes to the aqueous solution a patch of hydrophobic residues (blue) that surround the Cu I/II redox center (brown).

A similar feature was reported previously in high resolution topographic ECSTM images as a bright central spot in Az molecules that was attributed to the copper ion in the protein active site[169]. We observed that the ac modulated signal (dI/dU) is more sensitive to conductance changes than topographic features, allowing to clearly resolve a high conductance spot of Azurin in DECC images (right panels in Figure 3.12).

Simulations of Az conjugated to a gold (111) surface[213] concluded that the preferred orientation of the protein is almost lying down on the surface. The molecule, covalently bound through two surface cysteines (colored green in Figure 3.12c) is expected to lie down with its hydrophobic patch (blue in Figure 3.12c) oriented upwards. This solvent-exposed hydrophobic patch surrounds the Cu center, and plays a major role in electron transfer[169, 214, 215]. In this configuration, the Cu center would be facing the probe, thus favoring the electron transfer between them. These results are in agreement with the high conductance spot that is observed at the center of Azurin proteins (Figure 3.12) and together lend support to the idea that ET through Az is mediated by its copper atom[71, 169]. In the context of biological ET between redox proteins and their partners, protein regions with high conductance can be associated to specific, high electronic coupling sites required for efficient electron exchange[192].

3.4 Conclusions

We have developed a method to obtain differential conductance images of a surface under electrochemical control. The technique is useful to characterize materials surfaces like the reversible oxidation of an iron electrode, whose conductance and topography can be monitored simultaneously in different redox states.

The conductance changes between reduced and oxidized iron measured with this technique are in agreement with previously published results, and display several unique advantages over the classical method to measure the local conductance in solution: a low-noise dI/dU signal is measured in a narrow potential range (leading to a low electrochemical perturbation of the system, comparable to that of electrochemical impedance spectroscopy[216]) and averaged continuously at high frequency without interrupting the feedback control.

DECC imaging has also been used to characterize a bioelectrochemical system, the redox protein Az on a flat gold surface. Simultaneous topographic and conductance images of individual proteins were acquired under bipotentiostatic control of probe and sample in the aqueous solution. Conductance images revealed a sub-molecular resolution spot in the protein that indicates the existence of an ET pathway towards a localized, high electronic coupling site.

DECC imaging offers many opportunities to functionally characterize electroactive materials, nanoelectronic devices and redox biomolecules including multisite proteins. As a non-contact approach to measure the local differential conductance, it could also be combined with STM-based break-junction methods, which are extensively used in molecular electronics[217-219]. DECC imaging of molecular devices and chemically functionalized surfaces would allow assessing their uniformity and reliability, which are crucial technological aspects in micro- and nanofabrication[220]. It may also open new possibilities to study the heterogeneity of single molecule devices[126]. In redox proteins complexes, DECC imaging can be used for electroactive site spotting in combination with the control over protein orientation on the surface (e.g. by engineering cysteine residues or alternative linking chemistries) and ET computer simulations, potentially leading to the experimental verification of certain conductance pathways in three dimensions.

4

Conductive AFM in electrochemical media

4.1 Introduction.

Conductive atomic force microscopy (cAFM) is an excellent tool to investigate the electron transport through molecular junctions. It offers the possibility to study simultaneously the mechanical and electronic properties of a molecular junction, and allows investigating the relationship between the structure of a molecule and its electronic behavior. This technique has been applied to different systems, including ET proteins[128, 178, 179, 221-223] in non- electrolytic environments.

Working with AFM in aqueous solution allows studying redox proteins in nearly physiological conditions under full electrochemical control, but is technically challenging. In order to work in electrolytic environments under potentiostatic control, the EC-cAFM conducting tip requires insulation in all its body except at the apex. There is a lack of affordable commercial solutions for this problem, and thus several approaches have been reported to fabricate tips that satisfy this requirement. Most of these approaches are based either in modification of commercial tips or microfabrication of tips that require many micro- and nanofabrication steps[186, 224-229]. Some other methods, like the one developed by Abbou et al.[230] in Dr. Demaille's group, involve a fabrication process that can be entirely done in a regular laboratory, without requiring nanofabrication tools facilities.

Here, we aim to develop a protocol to obtain cAFM probes able to work under electrochemical media. For that we have followed two approaches: we applied the methodology reported by Hong et al.[231] to coat commercial tips with an Alumina layer, and second, we adapted the coating technique reported in Abbou et al.[230] to commercial tips. We obtained insulated conductive AFM tips with low leakage currents (<50 pA) and performed preliminary break junction experiments on a gold electrode by creating and breaking Au molecular wires in an electrolytic media.

In parallel, thanks to a collaboration with Dr. Demaille's group, we used the *homemade* AFM-SECM probes developed in this group[230], which had been already applied to different systems[232-234] to study gold surfaces coated with *P. Aeruginosa* Azurin in an electrochemically controlled media. With these tips we created force controlled junctions Au-Azurin-Au and explored their current-voltage (I-V) characteristics as a function of the applied force and the protein redox state. We also performed simultaneous force and current spectroscopic measurements of this system under electrochemical control. These experiments where performed in Dr. Demaille's lab at the *Laboratoire d'Electrochimie Moleculaire* (LEM) at Université Paris Diderot-Paris 7, in two research stays during the thesis.

4.2 Experimental methods

Chemicals and materials

Azurin and all reagents were purchased from Sigma, unless otherwise specified. The electrolyte for leakage current testing was Na_2SO_4 0.2M. Buffer solution for the Azurin measurements was 50 mM Ammonium Acetate buffer (pH 4.55). All solutions were prepared using Milli-Q water of 18 MΩ · cm.

Au electrode preparation.

Two kinds of Au electrodes were used for these measurements.

For the measurements performed in our laboratory in Barcelona with the coated commercial tips, Au (111) single crystals (Mateck GmbH) were used. The electrodes were prepared as described in chapter 2.

For the electrochemical cAFM measurements performed in Dr. Demaille's lab in Pairs, flat gold evaporated substrates were produced by template-stripping of a 200 nm thick gold layer deposited on mica, as previously described[235]. Briefly, the gold layer was deposited on a freshly cleaved mica sheet in the vacuum chamber of a BOC Edwards auto 306 vacuum system. The mica sheet was positioned 20 cm above pure gold (99.999%), which was then evaporated under a pressure of 2×10^{-6} mbar onto the mica surface at the rate of 0.1 nm/s. The evaporation was complete after a 200nm thick Au layer had been deposited. The gold-covered mica sheet was then glued (epotek 377) onto a clean glass slide and cured in an oven at 150 °C for 1.5 h. The mica-gold-glass sandwich was stored and the gold surface was separated from the mica just before use. To separate the gold surface from the mica, the mica-Au-glass sandwich was immersed in THF for several minutes, after which it was possible to easily pull the mica from the gold surface. The gold surface was then thoroughly rinsed with ethanol and Milli-Q water. An adhesive perforated Teflon mask was then glued to the gold surface, leaving a disk-shaped area of bare gold 0.76 cm in diameter.

Azurin incubation.

Protein solution was incubated on the electrode surface as described in previous chapters.

Commercial tip coating.

Commercial tips were single beam rectangular silicon cantilevers with a Pt/Ir coating CONTV-PT, and V-shaped Au coated tips NPG-10, both from Bruker AFM probes. Two different methods were used to coat commercial cAFM probes: atomic layer deposition and electrophoretic deposition paint.

Atomic Layer Deposition (ALD) of an Alumina layer (Al_2O_3) was performed at the Clean Room at the Nanoquim Platform at ICMAB, with Dr. Edgar León. The tips were previously cleaned with ethanol and Milli-Q and dried with a N_2 flow. The tip holders were sonicated in acetone for several minutes, then rinsed with ethanol and Milli-Q water. The tips were mounted on to the holders and introduced into the ALD chamber. Once inside the ALD chamber, they undergo a cleaning step with ozone. Then we proceed with the Al_2O_3 deposition at a rate of 0.9 Å/s at 200 ^{o}C until we achieve a 20 nm layer thickness.

Coating with Electrophoretic Deposition Paint (EDP) was performed with an Autolab potentiostat (MetroOhm). Prior to the coating, the tips were rinsed with ethanol and Milli-Q water and dried under a N_2 flow, and then cleaned in a UV-Ozone cleaner (BioForce NanoSciences) for 15 min. The electrophoretic deposition paint was a sample kindly provided by Mcdermid. The paint was diluted 1:1 and sonicated prior to use. For the deposition step, a two-electrode configuration was used, using a Pt/Ir wire as a counter electrode. Two different procedures were followed, either we applied a fixed potential of -10 V to the tip for 5 min, or we applied a potential ramp, from 0 to -5 V at a 50 mV/s rate. After the coating, the tips were rinsed with Milli-Q water to remove the possible excess of particles and the paint was cured at 110-160 ^{o}C for different curing times.

Leakage current tests

Leakages current tests were performed in a three-electrode cell with the tip as a working electrode, a Pt/Ir as counter electrode and Ag/AgCl reference electrode. The tip was immersed in the electrolyte (Na_2SO_4 0.2 M) and a constant voltage of 100 mV was applied to the tip, while we measure the current response with time.

Exposure of the tip apex and Force spectroscopy tests

Force spectroscopy tests were performed in an AFM Dimension 3100 equiped with an extended TUNA unit and controlled with Nanoscope IV electronics (Bruker). The coated tip was placed on the holder, and the metallic parts of the holder were coated with Lacomit varnish (Agar Scientific) for electrical insulation. An Au single crystal (111) was used as a substrate. To discover the apex of the tip, the tip was brought to contact the gold electrode in air. Then a combination of pulses and mechanical abrasion was applied to the tip until there was some current detection. Once we had current detection, we proceed to work in liquid in 0.2 M Na_2SO_4 electrolyte, were we performed repeatedly force curves over the substrate for different bias and velocities.

Cantilever spring constants were calibrated with a MFP-3D AFM (Asylum Research) by using the equipartition theorem (thermal noise routine)[236].

Preparation of EC-cAFM tips

EC-cAFM tips were provided by Dr. Demaille, and were prepared following a reported protocol largely detailed in[230]. Briefly, a 60 µm diameter gold wire was flattened, and its extremity was successively bent and etched to obtain a flexible cantilever (spring constant in the 1-4 N/m, fundamental flexural frequency~2-3 kHz) bearing a conical tip with a spherical apex in the ~100 nm range in radius. The tip was fully insulated by deposition of an electrophoretic paint and glued onto an AFM chip. The apex was selectively exposed to act as a current-sensing nanoelectrode.

EC-cAFM measurements.

The EC-cAFM experiments were performed with a Molecular Imaging PicoSPM AFM microscope (Scientec, France), which was modified and operated as previously described[235]. A homemade bipotentiostat enabled us to independently apply the electrochemical tip and substrate potentials with respect to a Pt/PPy quasi reference electrode described below, using a Pt wire as counter electrode. The Molecular Imaging PicoSCAN controller was used to generate the tip potential and to acquire the tip-current data. Experiments were carried out in situ in a fluid cell containing an aqueous 50 mM $AcNH_3$ buffer electrolyte solution. During the experiments, the microscope head was placed inside a homemade vibration-proof Faraday cage.

The polypyrrole quasi-reference electrode (Pt/PPy) was fabricated according reported protocols[237] previously used in the group[234]. Briefly, a polypyrrole film was electrochemically deposited on a platinum wire by cyclic voltammetry (50 cycles between -0.6 and 1.4 V vs SCE) in an acetonitrile solution containing 0.01M pyrrole and 0.1M Bu_4NPF_6. The final cycle was stopped at 0.65 V/SCE for 30 s to partially oxidize the film. The Pt/PPy quasi-reference electrode was rinsed with acetone and soaked in pure acetonitrile for 1h. Then it was immersed for 30 min in our measuring buffer (50 mM Ammonium Acetate), to exchange the PF_6^- for ion Acetate. The quasi reference electrode was stored in the measuring buffer and calibrated against a KCl saturated calomel electrode before each experiment. The quasi reference electrode showed a stable OCP of 0.130 V vs the SCE.

For the force modulated current-voltage measurements, the tip was brought into contact to the surface applying different forces. Once the contact was stable, a triangular potential ramp of 0.5 V was applied to the tip potential at 50 mV/s rate. The probe was moved between curves to ensure a representative data collection. The curves were performed at three different sample potentials: U_S= 10 mV, 150 mV and 250 mV vs Ag/AgCl. The tip potential ramps always started at the tip potential implying the more negative bias (being $U_{bias}=U_{tip}-U_{sample}$).

Force and current spectroscopy curves were acquired by approaching and retracting the tip from the sample at 25 nm/s using the deflection as feedback.

Data was acquired through the Molecular Imaging PicoSCAN controller and analyzed using Origin.

4.3 Results and Discussion

4.3.1 cAFM probe insulation techniques

In our aim to obtain a simple protocol for obtaining conductive AFM tips that could be used in electrochemical media, we followed two strategies to electrically insulate commercial conductive AFM tips: coating commercial tips with an Al_2O_3 layer with Atomic Layer Deposition, or coating the tips with a layer of Electrophoretic Deposition Paint.

4.3.1.1 Insulation with Al_2O_3.

Hong et al.[231] developed a method to improve the resolution of cAFM tips up to ~1nm. This method was based in coating a commercial cAFM tip with an insulating layer (Al_2O_3) and creating a metallic microwire in its apex electrically. Inspired by this work, we decided to test this methodology for the fabrication of cAFM tips that could work in an electrochemical media.

In collaboration with Dr. Francesc Pérez-Murano and Dr. Narcís Mestres from the Universitat Autònoma de Barcelona-ICMAB, we used Atomic Layer Deposition (ALD) to deposit a conformal 20 nm Al_2O_3 layer on commercial conductive AFM tips. The deposition conditions were 0.9Å/s at 200 ^{o}C. The small size and the geometrical shape of the tips can be a challenge for the coating, thus we used a thicker (20nm) layer than the ones reported by Hong et al., and choose high temperature depositions that would lead to more dense layers.

Some of the Al_2O_3 coated tips low leakage currents as required by cAFM, (Figure 4.1) but in general this parameter was not very reproducible. Half of the tips showed current leakages above 1 nA, and only 10% showed leakages below 100 pA. This lack of reproducibility could be due either to the Al_2O_3 layer not depositing uniformly on the tips, or to the porosity of the layer, that does not insulate completely the body of the tips.

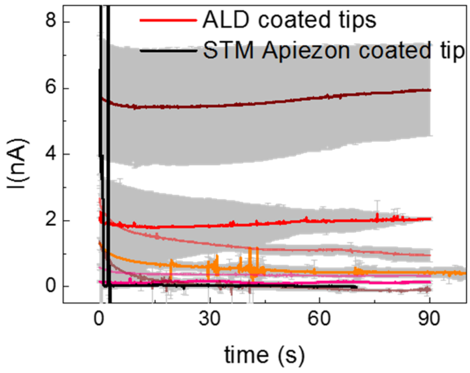

Figure 4.1. Leakage currents of Al_2O_3coated c AFM tips. Black line corresponds to the leakages of an Apiezon coated STM tip for comparison. The different red lines correspond to different Al_2O_3 tips. All tips were tested in a three-electrode configuration using a Pt/Ir wire as a counter electrode and a Ag/AgCl reference electrode. The electrolyte was Na_2SO_4 0.2 M, and applied voltage was 100 mV.

4.3.1.2 Electrophoretic Deposition Paint coating

As an alternative approach, we used electrophoretic deposition paint (EDP) to coat commercial cAFM tips. EDP had been previously used to coat fabricated tips for AFM-SECM[230, 238, 239] and STM tips[168] with very low leakages currents results. With this technique, the deposited layer can be optimized by tuning the potential applied to the tip.

We coated the tips following mainly two different strategies of deposition of the paint: applying a continuous DC potential to the tip for a determined time, or applying a potential ramp to the tip.

For the tips coated with a continuous dc potential, it was possible to optimize the conditions to get reproducible, low leakages tips. The applied potential to the tip was -10 V, after discarding more negative potentials (-30 V) that seem to damage the conductive coating of the tip. Then the curing step for the paint was optimized (Figure 4.2a) leading to a 15min curing time. With these conditions, we were able to obtain low leakage tips (Figure 4.3b), with better reproducibility: ~80% of the tips had leakages below 0.2 nA, and ~30% had leakages below 50 pA.

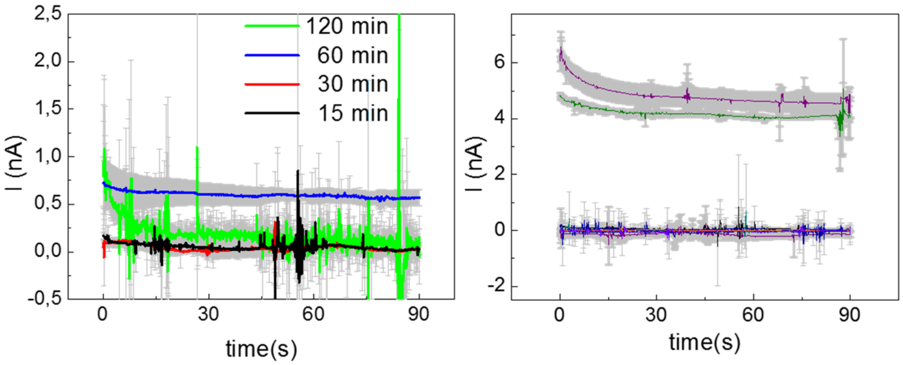

Figure 4.2. Leakage currents of EDP coated tips. All the tips were coated applying -10V during 5 minutes to the tip. a) Leakage comparison for different curing times for the paint, varying from 15 min to 120 min at 110ºC. b) Leakage currents of 10 tips coated applying -10V to the tip, with a curing time of 15 min. All tips were tested in a three-electrode configuration using a Pt/Ir wire as a counter electrode and a Ag/AgCl reference electrode. The electrolyte was Na_2SO_4 0.2M, and applied voltage was 100mV.

Although several of these coated tips had a good enough current leakage to test them in the c AFM, in more than 50% of these cases the shape of the tip was slightly compromised by the paint layer, being the paint layer too thick for the laser of the AFM to reflect on it.

Tips coated with a potential ramp instead of a continuous DC potential, showed no alteration in their shape (Figure 4.3), neither with rectangular cantilevers nor with triangular cantilevers. The success rate was even higher than with the DC continuous potential and ~70% of the tips showed current leakages below 50 pA.

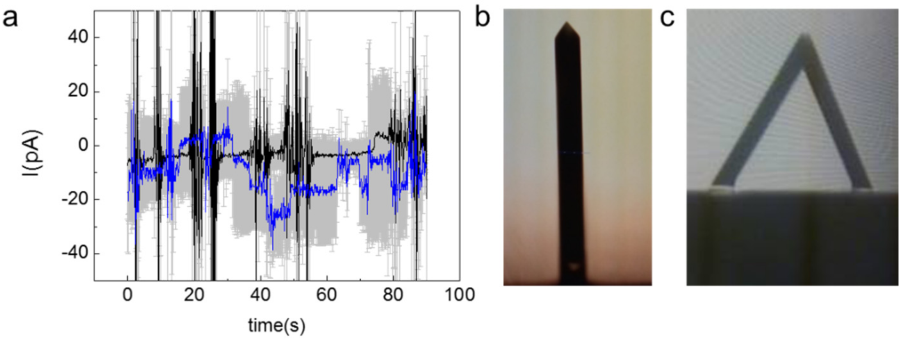

Figure 4.3. a) Leakages current of cAFM tips coated with EDP applying a ramp of potential from 0 to -5 V at 50 mV/s, tested in a three-electrode configuration using a Pt/Ir wire as a counter electrode and a Ag/AgCl reference electrode. The

electrolyte was Na2SO4 0.2 M, and applied voltage was 100 mV. b) and c) photographs of a (b) Pt/Ir coated rectangular cantilever and a (c) Au coated triangular cantilever, both EDP coated applying a ramp of potential.

With ALD coating we obtained some low leakages tips, but reproducibility was low, only ~40% of the tips had leakages under 1 nA, and just ~10% of the tips had current leakages lower than 100 pA. With EDP coating by applying a continuous DC potential we optimized the conditions to obtain around 30% of the tips with current leakages below 50 pA, but some of the cantilever showed some alterations in its properties. With EDP coating by applying a potential ramp, we obtained reproducible, low leakage curves, and with a thin coat layer that did not compromise the shape or reflectance of the cantilever.

4.3.1.3 Force and current spectroscopy of Au-Au junction in electrolytic media

The tips coated with EDP with the ramp potential method were used to perform force spectroscopy curves in c AFM in an electrolyte. Previous to the measurements, the tips were calibrated using the thermal noise method. The calibrated tips showed a spring constant between 2 and 3 times higher than the nominal one, obtaining spring constants of around 500 pN/nm for tips with nominal spring constant of 200 pN/nm, and 150 pN/nm for tips with a nominal spring constant of 60 pN/nm.

At the beginning of the experiment, the tips were completely coated with the insulating layer. To expose the apex of the tip to detect current through it, the tip was approached in contact mode with a high setpoint to the conductive substrate (Au electrode) and several pulses of 5-10 V were applied. After every pulse the current detection was checked either by imaging the surface or by performing an approach curve. This process was repeated until the tip detected current from the substrate.

Once the tip was exposed, force controlled break-junctions curves were performed in a clean substrate. Force controlled break-junctions consisted in, starting with the tip out of contact, approaching the tip till there was contact with the sample and then retracting the tip, while recording the current response (Figure 4.4). In the retracting process, we observed current traces that resemble the ones obtained with the break-junction technique: the current is saturated while the two electrodes are in contact, and decrease sharply when they the contact breaks. In most current traces, we see a current step or plateau when the tip is retracted, what indicates that a small junction is created and broken during the retraction of the tip. Collecting the retracting current traces, we can construct conductance histograms (Figure 4.5). We obtained a value of 0.67 ± 0.02 G_0 conductance value for the steps, in the range of the corresponding conductance of a Au-Au junction. The same experiment, performed with commercial conductive AFM tips without further treatment (i.e. not insulated) in air conditions resulted in an agreeing value of 0.66 ± 0.02 G_0 (Figure 4.5b, grey).

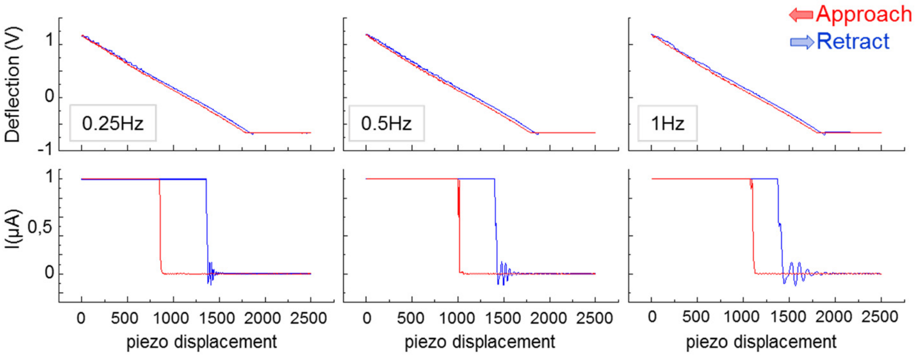

Figure 4.4. Examples of simultaneous force and current recordings of an insulated cAFM tip, at different approach rates. Measurements were performed in Na_2SO_4 0.2M applying 10 mV bias to the tip.

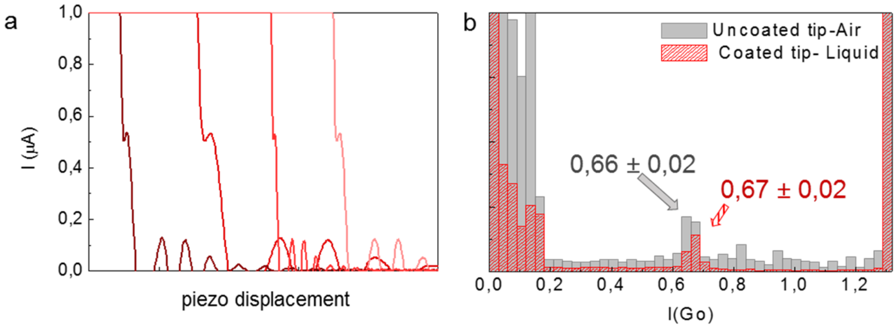

Figure 4.5. a) Current retrace curves obtained with insulated c AFM tips in Na_2SO_4 0.2 M applying 10 mV bias. The x-axis represents piezo displacement, but the traces have an offset for clarity. b) histograms of retracting current traces over a gold electrode. Grey histogram corresponds to current traces obtained in air with a commercial cAFM tip without insulation. Red histogram corresponds to curves obtained with an insulated tip in liquid, at the same rate and bias conditions.

4.3.2 Electrochemical cAFM measurements of Azurin protein.

In parallel to this experiments, we started collaborating with Dr. Demaille's Group in the Université de Paris 7 - Paris Diderot. This collaboration has included two stays in the group in Paris, where the homemade AFM probes the group developed were used to perform simultaneous current and force measurements on the Azurin-Au system, under full electrochemical control. With these measurements we evaluated the electrical response of azurin molecule as a function of the applied force at its different redox states.

4.3.2.1 Force-controlled current voltage spectroscopy (ECTS).

Force-controlled current voltage spectroscopy of azurin protein was performed by approaching the tip to the sample in contact mode at a fixed value of deflection (force) and thus creating a Au-Azurin-Au junction. Once the tip was in contact with the sample and thus the force controlled junction was established, a linear potential ramp was applied to the tip potential, recording the current response. As we applied a potential ramp to the tip potential while keeping the sample potential fixed, we are in fact measuring the current response to the variation of the bias potential ($U_{bias} = U_{tip} - U_{sample}$). We performed current-voltage spectroscopy using a wide range of applied forces in the molecular junction. To explore the conductance-force dependence of Azurin in its different redox states, we performed current voltage curves, with the same range of forces, at three different potentials U_S = 10 mV (for Azurin in the reduced state), U_S = 150 mV (at its redox midpoint) and U_S = 250 mV (in its oxidized state).

Azurin IV curves showed a clear dependence with the force applied at the three measured sample potentials (Figure 4.6). The conductance of the Au-Azurin-Au junction increases with an increasing applying force in all three cases. It is important to note that the applied forces may seem higher than usual for proteins but it should be taken into account that the homemade probes are not so sharp, being the radius about 100 nm. Thus, the applied pressure to the proteins at 100 nN would be in the same range that the pressure applied by a commercial tip of 15 nm radius when is applying 2-3 nN force.

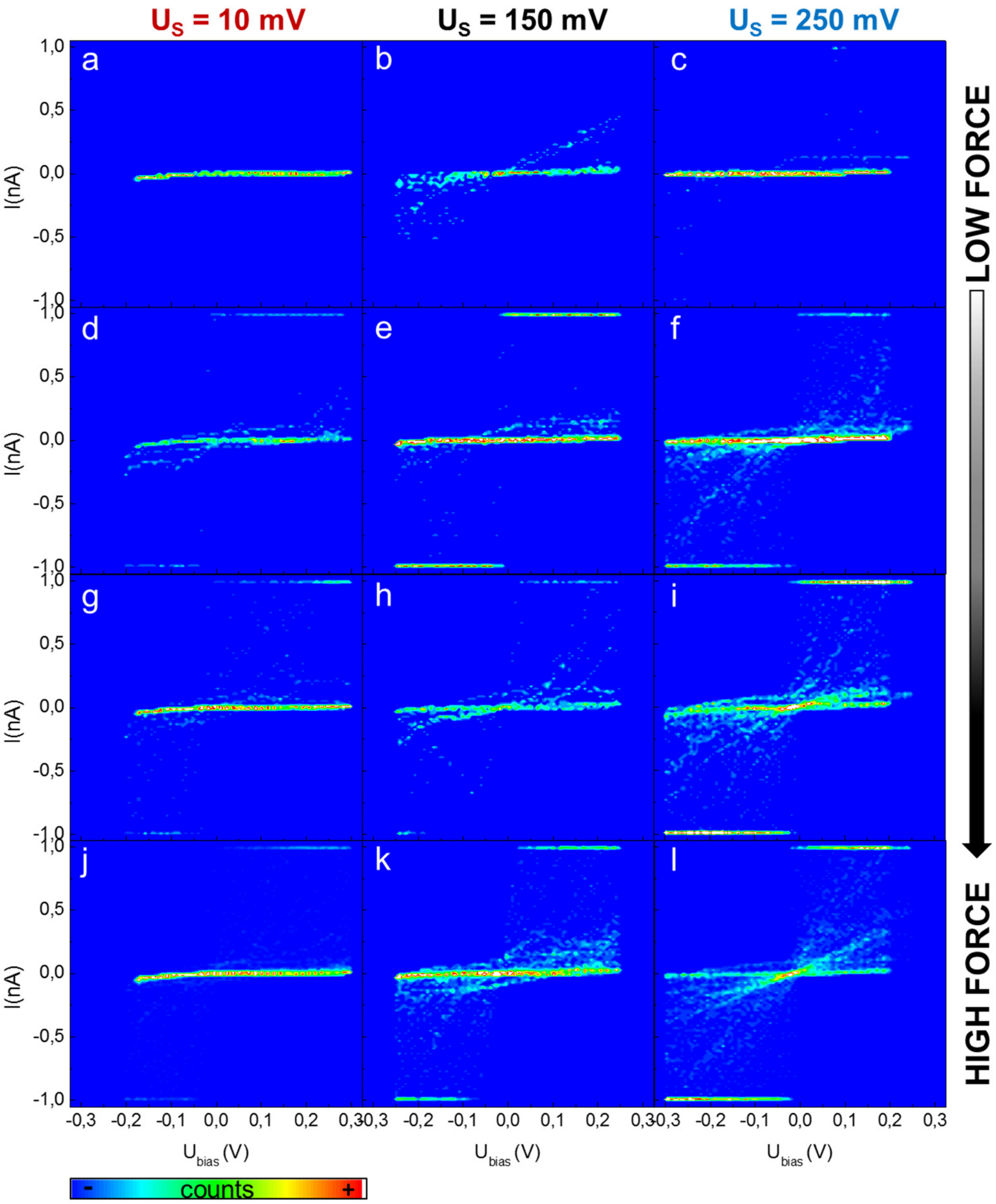

Figure 4.6. IV curves of Azurin protein at Us=10 mV (reduced state)(a,d,g,j), Us= 150 mV (midpoint potential)(b,e,h,k), and Us= 250 mV (oxidized state)(c,f,i,j), adquired with different applied forces (increasing force from top to bottom). IV curves always started at the more negative bias value.

At low forces, the I-V curves appear as almost a flat line, with a slope close to 0 nA/V. As we increase the loading force, we see the slope increase. Azurin has been reported to require a minimum load force to give current signal[128, 177, 178, 221]. The increase of conduction with the applied loading force could be due to several factors. First, an increase in the loading force may imply an increase in the tip contact area, leading to a larger number of Azurin proteins in contact with the tip. The increasing applying force also entails a decrease in the tip-substrate distance, which may contribute to the increased current. Also, the loading force may be distorting the secondary structure of the protein, which can lead to changes in the electronic properties of the protein[128]. All these factors may contribute to the increase in current flow through the junction with an increasing loading force.

Interestingly, the conductance of the protein does not increase at the same rate with applied force at different redox states (Figure 4.7). At low applied forces, in all three cases the IV characteristics are almost flat. When we increase the force, we see that when the protein is reduced, the IV curve is still flat, but for the same applied force, at the redox midpoint, the junction conductance increases, and is even higher when the protein is oxidized. Thus, the Au-Azurin-Au junction requires lower forces to conduct through the junction when the protein is oxidized.

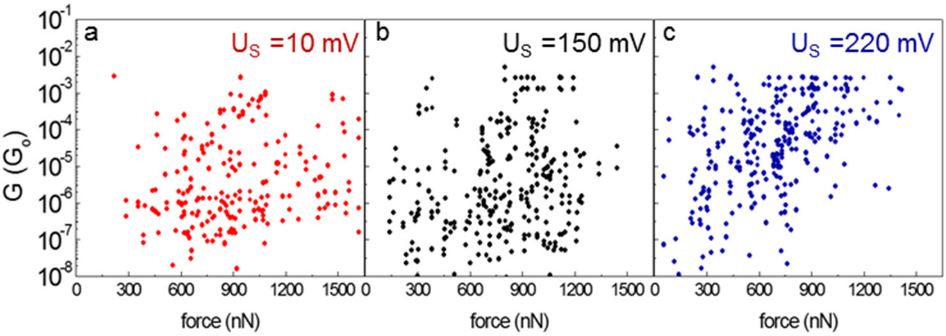

Figure 4.7. Evolution of the conductance of the Au-Azurin-Au junction with the applied force at different sample potentials a) U_S=10 mV, b) U_S= 150 mV, c) U_S= 250 mV.

The lower minimum force required to achieve a good conduction when the protein is oxidized with respect to the other states, could mean that the protein is more sensitive to force changes when it is oxidized, and thus more flexible than at its reduced form. Nevertheless, there is no evidence that suggest a change in structure of the protein with its redox state. Thus, this effect is more probably due to a more efficient ET through the protein when it is oxidized.

4.3.2.2 Force and current distance spectroscopy.

We performed simultaneous force and current-distance spectroscopy measures over the Azurin-Au system. In these experiments, the AFM tip is approached and immediately retracted from the sample while deflection and current are recorded. As the tip makes contact with the sample and presses the substrate, the current increases until a saturating point where it makes direct contact with the Au substrate, either displacing the proteins on the sample or passing through them. When the tip is retracted, in the moment that it stops contacting the Au electrode, the current stops saturating and drops sharply to 0nA. In the retraction process a molecule or a few molecules can get momentarily trapped between sample and tip, stablishing a Au-Azurin-Au junction. When this happens, we see a sudden plateau or step in the current trace. When the junction brakes, the current drops sharply again.

While performing the experiments, it was seen that the deflection and current curves not always correlated (i.e. the current did not start increasing as the tip entered in contact with the substrate), which agrees with the current-voltage results, that showed that it was necessary to apply a minimum force to measure current through the junction. We performed these experiments at different sample potentials: U_S = -20 mV for the reduced state, U_S= 120 mV for the redox midpoint and U_S= for the oxidized state. All measurements were made keeping a negative bias of U_{bias}= -100 mV.

In the first stage of the curves, when the tip is approaching the sample, we see that, for all three conditions, the current increase while the applied force increases (Figure 4.8). However, in the case of the reduced protein the minimum force necessary to detect current through the protein is much higher than in the other cases. When the protein is reduced, the current traces start increasing when the applied force is above several hundreds of nN. This does not happen when the protein is either at the midpoint or oxidized potentials. These two states have a similar distribution of required minimum forces (Figure 4.8e, 4.8f), where current starts to flow when the applied force goes above 50-100 nN.

These results agree with what we observed during the current-voltage experiments in the previous section, where we observed that the required force for current flow through the junction Au-Azurin-Au, was higher when the protein was at its reduced state. The structure of the Azurin protein is independent of its redox state[240], thus the changes we see are most probably related to the ET mechanism of Azurin,that has been reported to show asymmetries with its redox state[105]. In the case, of the force and current distance spectroscopy curves, we have a more negative tip potential than sample potential, thus the tip is injecting e^- in to the sample, or holes (electron vacancies) are transferred to the probe. It seems that the less efficient process of injecting e^- in an already reduced protein, is not accessible applying low forces on the junction. If the force continuous to increase above a threshold of 500nN, the current starts to flow through the junction. The fact that the ET mechanism becomes more favorable upon compression, could be due to an alternative e^- pathway result of a structural deformation of the protein.

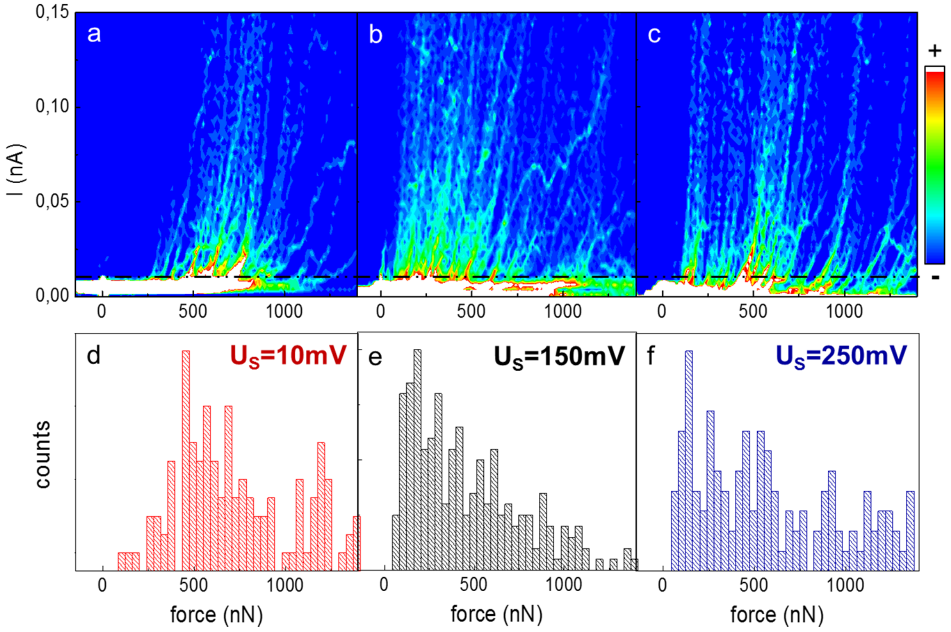

Figure 4.8. a,b,c) Evolution of the current with the applied force approaching the tip. 2d histogram that collects the current traces of the approaching curves plotted vs applied force for a)U_S = 10 mV , b) U_S=120 mV, and c) U_S= 220 mV. U_{bias} was kept constant at -100 mV. 2d histogram counts follow the shown color scale (right). d, e, f) statistics of the minimum force necessary to apply for the current to be I> 0.01 nA for d)U_S = 10 mV , e) U_S=120 mV, and f) U_S= 220 mV. The histograms in (d, e, f) represent the 1d representation of the dotted black line on the 2d histograms in (a, b, c).

During the retraction of the tip, we obtained current traces with steps or plateaus that signal the presence of transiently-established junctions. In the same way as ECSTM break junction experiments, we can collect these curves and construct conductance histograms. In our histograms (Figure 4.9) the current steps stand out as a peak around 4-9 · 10^{-5} G_o, in the range of the Azurin single molecule conductance[106]. This peak shows modulation with the sample potential, in agreement with previous results performed with ECSTM (Figure 4.10), which confirms that these steps are a result of Au-Azurin-Au junctions.

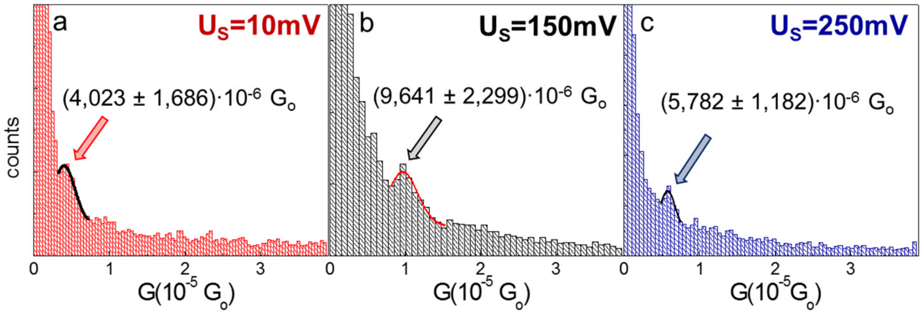

Figure 4.9 Conductance histograms constructed collecting current-distance retracting curves at a)U_S = 10 mV , b) U_S=120 mV, and c) U_S= 220 mV. All measurements were performed keeping a constant U_{bias}= U_{tip}-U_S of -100 mV.

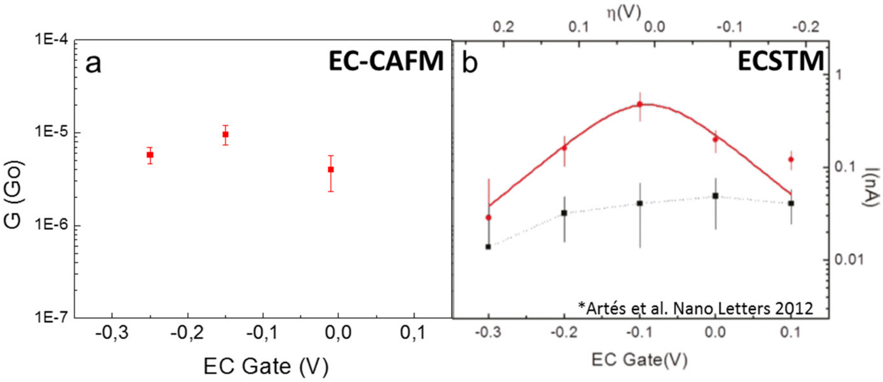

Figure 4.10 Comparison between the results for conductance gating obtained with a)EC-CAFM (figure 4.9) and b)ECSTM. b) Adapted with permission from ref [106](Artés et al. NanoLett 2012). Copyright (2012) American Chemical Society.

The applied force at the moment of the breaking of the step (Figure 4.11) gives a wide distribution in all three cases, most probably due to a limited number of replicates. However, the distribution of forces for the reduced protein hints a peak centered at higher forces than in the case of the redox midpoint, where the distribution insinuates a peak aroud 150-200 nN. This points in the same direction of the results discussed above, where the Au-Azurin-Au junction required a higher force to conduct. Once the force applied is below this threshold, the conductance drops. Regarding the applied force at the moment at which the tip stops detecting current (I<0.01 nA)(Figure 3.12), we observe no significant changes between the protein redox states. In all three cases, the distribution of forces, although wide, suggest a peak centered around 0 nN, when the tip is completely out of contact with the sample.

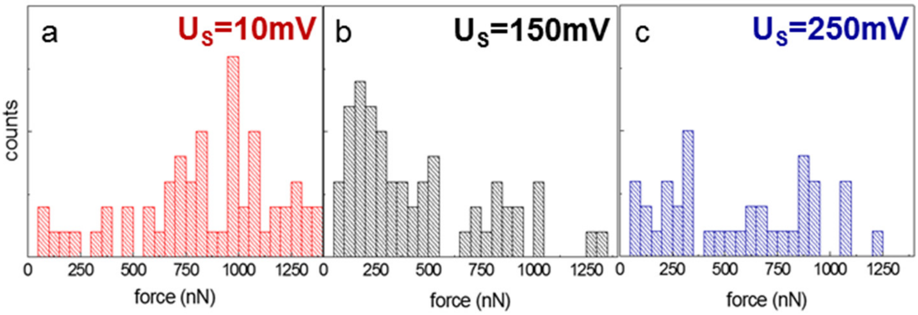

Figure 4.11. Statistics of the applied force at the end of the conductance steps, at the moment the molecular junction breaks, for three different U_S potentials a)U_S = 10 mV , b) U_S=120 mV, and c) U_S= 220 mV.

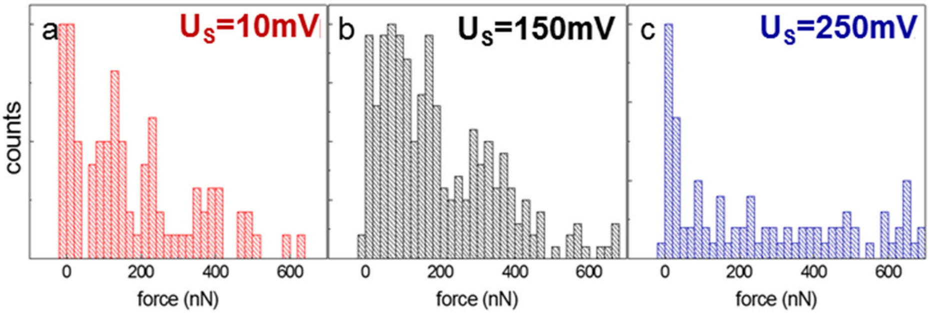

Figure 4.12. Statistics of the applied force when the tips stops detecting current (I<0.0 1nA) for three different U_S potentials a)U_S = 10 mV , b) U_S=120 mV, and c) U_S= 220 mV.

4.4 Conclusions

In this chapter, we described the adaptation of different methods to coat conductive AFM tips. We developed a protocol that allowed us to reproducibly obtain cAFM insulated tips with low leakages (<50 pA). With this protocol, we were able to coat different tip shapes, keeping low spring constants. The coating process is fast and all the steps are doable in a regular laboratory. With these tips we measured the conductance of Au-Au junctions in an electrolyte, obtaining similar results to the ones obtained with commercial conductive AFM tips in air. We are working towards adapting these tips to measure the conductance of small molecules and proteins under electrochemical solution.

Following a parallel approach, we used hand fabricated AFM-SECM tips provided by Dr. Demaille to study the Azurin-Au system. With these tips, we performed simultaneous force and conductance measurements on a protein in electrochemical media for the first time. We performed two kinds of experiments: force controlled current-voltage spectroscopy and force and current-distance spectroscopy. Both methods showed that the conductance on the Au-Azurin-Au junction increased with the applied force over the junction. Surprisingly, we found that the conductance-applied force dependence changed with the redox state of the protein: the required force for current flowing through the Au-Azurin-Au is higher when the protein is reduced.

The increase of conductance upon an increase on applied force could be due to a number of factors: An increase in the contact area, a reduced distance between the tip and the Au substrate, changes on the structure or changes on the ET mechanism. These all factors can contribute to the increased conductance through the junction, but the difference between the redox states can only be explained through a change in the ET mechanism, since there is no evidence of structural changes between redox states in Azurin.

Although further studies are needed to understand the effects of applied force in azurin and its electronic behavior, it is clear that this method leads to a deeper understanding of the complex relation between the structure of redox proteins and their electron transfer properties

5

Characterization of PSI: SPM imaging and electrochemistry

5.1 Introduction

Photosystem I is a type I reaction center in oxygenic photosynthesis. It acts as a natural photodiode, being able to funnel electrons through an electron transport chain upon light radiation. The energy transfer efficiency of PSI is close to unity[138]. These features make PSI is a very interesting protein complex to study and a promising candidate for bioelectronics applications.

SPM are excellent tools to investigate the ET properties of individual molecules, PSI not being an exception. The PSI complex and the reaction center (RCI) from plants or cyanobacteria have been characterized with AFM[157, 241-244] , cAFM[141, 182, 183], KPFM[158, 245-247], SCEM[248], SNOM[143] and STM[184, 185], but its ET mechanism has not been characterized under electrochemically controlled conditions as the ones offered by ECSTM.

To investigate the properties of PSI with ECSTM, we need to immobilize the protein onto a conductive electrode. Ideally the immobilization technique should result in a uniform coverage, with a good orientation of the protein and good electronic coupling with the substrate. We used gold single crystals (111) as they are, stable and easy to functionalize and can be rendered atomically flat.

Plant PSI has an ellipsoidal structure (Figure 5.1), with polar stroma and lumen surfaces, and a hydrophobic region in contact with the membrane. It is usually present in a monomeric form, and has a crystallographic structure with a maximal height of~100 Å and major and minor diameters of ~185 Å and ~150 Å[51] respectively.

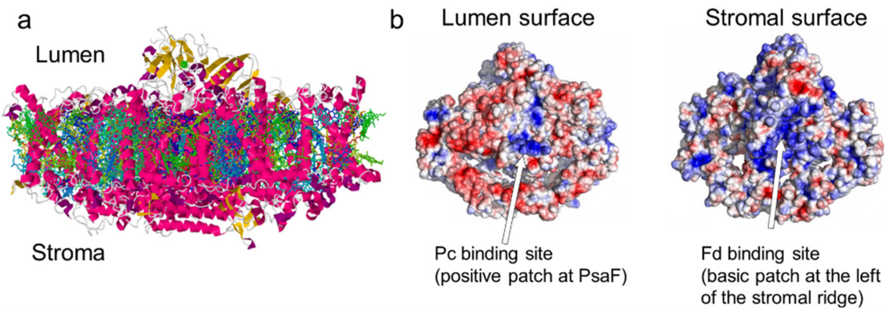

Figure 5.1. a) Crystallographic structure of PSI (PDB: 4XK8) b) Surface potential representation the lumen and stromal sides of the protein. (adapted from Mazor

et al. eLIFE 2015[29]) Color scale red for negative, blue for positive. The binding sites of PSI redox partners plastocyanin (Pc) and Ferredoxin (Fd) are indicated.

Several immobilization strategies have been described and many of them take advantage of the polar regions in the surface of the protein structure to immobilize the protein via electrostatic interactions. For this, normally a gold electrode is functionalized with a self-assembled monolayer of alkanethiols with different terminal groups[141, 159, 185, 246, 249-252]. Other immobilization techniques include electrode functionalizations to bind the PSI covalently[248, 253], PSI mutations to include surface cysteines[140, 143, 158, 247], electrophoretic deposition[157, 242, 244], molecular wires[159], etc.

In our case we used simple immobilization strategies: adsorption of PSI on a bare gold substrate; and adsorption of PSI onto alkanethiol-SAM functionalized gold substrates, with three different terminal groups: -OH, -NH2, -COOH, that yield respectively neutral, positively, and negatively charged surfaces in solution of suitable pH. We examined the PSI adsorption in each surface with AFM and evaluated the macroscopic redox activity and the photocurrent generation for the two functionalizations that resulted in higher adsorption. We finally imaged all the systems with ECSTM, and analyzed the effect in the ECSTM imaging of applied sample potential and of the bias between probe and sample potentials.

5.2 Experimental methods

Materials

All the chemicals where purchased from Sigma Aldrich, unless specified otherwise. All solutions were prepared using Milli-Q water of 18 MΩ· cm, and were bubbled with N_2 for oxygen removal. All the glass material used for the preparation of solutions as well as the electrochemical cells were previously cleaned with piranha solution 7:3 H_2SO_4/H_2O_2 (CAUTION: Piranha is extremely dangerous and should be used with extreme precaution).

Purification of Photosynthetic complexes.

PSI complexes were kindly provided by Dr. Emilie Wientjes. PSI complexes were purified as described in [254]. Thylakoids were isolated from Arabidopsis thaliana plants as described previously[255] . The PSI complex were obtained by mild solubilization of the thylakoids followed by the sucrose gradient density centrifugation, as described in [256].

Electrode preparation.

The Au electrodes used where Au <111> single crystals (Mateck GmbH). In order to clean and ensure a <111> surface of the single crystals they were annealed as describe in chapter 2.

Electrode functionalization

Right after annealing, the electrode was functionalized by immersion in an ethanol solution containing the different SAM molecules: 2-mercaptoethanol (2ME), 6-amino-hexane-1-thiol (6AHT), 8-mercaptooctanoic acid (8MOA). Concentrations. For AFM and ECSTM imaging, immersion was performed for 2 hours in the case 2ME, and overnight for the 6AHT and the 8MOA. Different immersion times were tested, and this gave the most uniform monolayers. For the voltammetric analysis, the electrode was immersed in either of the SAM solutions for 48 hours. After functionalization the electrode was immediately rinsed with ethanol and Milli-Q water repeatedly.

PSI incubation.

The PSI solution was diluted (1:10) and buffer exchanged with PBS buffer 50mM pH 7.4. Buffer exchange was done with Zeba Spin Desalting Columns for Thermo Scientific. This step was necessary to eliminate the excess of surfactant (dodecyl-β-maltoside, DDM), since an excess of surfactant could prevent the PSI to adsorb on the surface. Once filtered, the sample was immediately used for PSI incubation. In all the cases (bare gold or functionalized electrodes) 50 µl of diluted protein solution were incubated for 2 hours, in the dark, at room temperature.

Protein quantification.

Protein quantification was carried out using a Pierce BCA Protein Assay Kit from Thermo-Fischer. The BCA protein assay is based on the reduction of Cu^{2+} to Cu^{+} by protein in alkaline medium. The bicinchoninic acid (BCA) then reacts with the Cu^{+} ions resulting in an intense purple colored complex, which shows a strong linear absorbance at 562 nm with increasing protein concentrations. The protein content of unknown samples is spectrophotometrically determined by comparison with known protein standards (BSA). According to results, the concentration value of the original protein solution is 0.117 µM.

Cyclic voltammetry measurements.

Cyclic voltammetry measurements were carried out with an Autolab Potentiostat (Metrohm Autolab). The measurements were done in a three-electrode configuration with a Ag/AgCl reference electrode and a PtIr wire as a counter electrode (CE). Electrolyte was PBS 50mM pH 7.4. When indicated, it contained 20 nM $Fe(CN)_6^{3-/4-}$ as redox mediator.

UV-Vis spectroscopy.

UV-vis spectroscopy was performed in a wavelenght range between 350 and 800 nm, using an Infinite M200 PRO reader from Tecan.

Photocurrent generation measurements.

Photocurrent measurements were carried out in an Autolab Potentiostat (MetrOhm) in a three-electrode cell configuration. Light cycles were performed with a high luminosity (400 mcd) red LED (Ariston Electrónica). Before the measurement, the potential was applied for about 3 min in the dark to stabilize the current. The light-dark cycles had a duration of 60 s each.

AFM imaging.

AFM imaging was performed in an ASYLUM MFP-3D. All images were performed in liquid (PBS 50 mM pH 7.4) using tapping mode. Tips were SNL-10 (Bruker). For the images on mica the sample was prepared by incubating a drop of solution on a freshly cleaved mica.

ECSTM imaging.

ECSTM imaging was carried out with our local ECSTM setup, a PicoSPM microscope head and a PicoStat bipotentiostat (Molecular Imaging) controlled by Dulcinea electronics (Nanotec Electronica). A homemade electrochemical cell was used in a four electrode configuration, using a Pt:Ir (80:20) wire as counter electrode and a miniaturized ultralow leakage membrane Ag/ AgCl (SSC) reference electrode filled with 3 M KCl. The potentials of the gold electrode sample (U_S) and ECSTM probe (U_P) are expressed against this reference. Pt:Ir ECSTM probes were prepared as described.[168] Recording solution was PBS buffer 50 mM pH 7.4. Data were acquired and analyzed using WSxM 4.0 software[190].

5.3 Results and Discussion

5.3.1 Bulk characterization.

5.3.1.1 UV-Vis spectroscopy.

The electron transfer chain of PSI is started upon irradiation with visible light. We investigated the absorption of visible light as part of the characterization process. Figure 5.2 shows the UV-Vis spectra of two sample of PSI: one with the PSI solution (orange line) and one that has been buffer exchanged (green line).

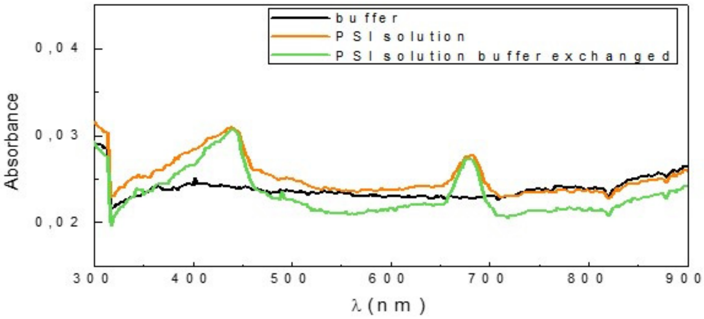

Figure 5.2. UV-Vis absorption spectra of PSI sample. Grey line corresponds to the absorption of the PBS buffer in absence of PSI. Orange line corresponds to the spectra of the original PSI solution. Green line corresponds to the buffer exchanged sample.

In both spectra, we see the two characteristic peaks for PSI[257], one centered at 675 nm and the other around 440 nm, both associated to chlorophyll content. The peak at 675 nm corresponds to the P700 center at the PSI, which is a special pair of chlorophylls that undergoes photoexcitation and starts the electron transfer chain. We observe no significant differences between the curves of the original solution and the buffer exchanged one, regarding both the position of the peaks and their absorbance. Thereby we can assume that we do not have protein loss during the buffer exchanging process.

5.3.1.2 Electrochemistry.

We characterized the redox activity of the P700 center of PSI. Figure 5.3 shows the cyclic voltammogram of a bare gold electrode, and the voltammogram of PSI protein absorbed on the gold electrode. In the bare gold electrode, we see the characteristic peak of gold in PBS (gold oxidation and stripping[250]) and a large capacitance, characteristic of a large bare electrode. When we incubated the PSI, we see a much lower capacitance current, indicating the adsorption of molecules on the electrode, and a small peak around 400 mV. Since the gold peak appears at similar potential, we cannot assign this peak to PSI.

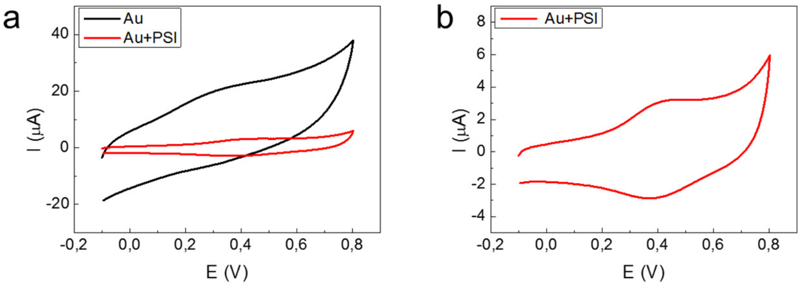

Figure 5.3 Cyclic voltammogram of PSI incubated on gold electrode (red) and of a bare gold electrode (black) in PBS 50mM buffer. Scan rate 50 mV/s. b) expanded current scale. Potentials expressed against Ag/AgCl reference electrode.

To avoid the gold peak, we characterized the redox activity of the PSI over functionalized gold electrodes with two different molecules: 2-mercaptoethanol SAM and 8-mercaptooctanoic acid SAM. Because of the SAM formation, the gold peak disappears and the capacitance decreases (Figure 5.3 Figure5.4, black). When we incubate PSI on the 2-mercaptoethanol functionalized gold we see an oxidation peak appear at ~350 mV, a bit higher than expected from the literature reports[251]. However, the potential values can change as the conditions surrounding the protein complex are modified[251].

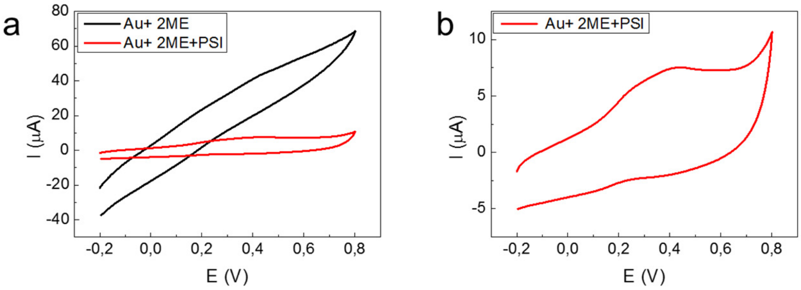

Figure 5.4. Cyclic voltammogramm of PSI on a 2 mercaptoethanol functionalizated electrode (red) and in the same system in absence of PSI (black). Rate 50 mV/s b) Expanded current scale. Potentials expressed against Ag/AgCl reference electrode.

With the 8-mercaptooctanoic acid SAM (Figure 5.4) we see a similar behavior, with a broader PSI peak centered around 350 mV.

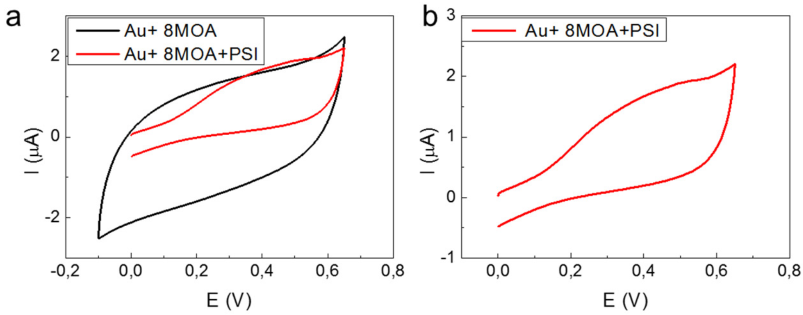

Figure 5.5. a) Cyclic voltammogram of PSI on a 8-mercaptooctanoic acid functionalized electrode (red) and in the same system in absence of PSI (blue). b) Expanded current scale. Scan rate 10 mV/s. Potentials expressed against Ag/AgCl reference electrode.

From the cyclic voltammograms we see that the PSI is attached to both SAM functionalized electrodes and is electrochemically active. The peak of the FeS centers is too negative to be explored with this technique, but it has been well characterized with square wave voltammetry in the literature[251].

5.3.1.3 Photocurrent generation.

We measured the changes in current due to illumination on PSI samples adsorbed on to 2-mercaptoethanol SAM and 8-mercaptooctanoic acid SAM functionalized Au electrodes (Figure 5.5). We kept the potential at 400 mV, at the beginning of the oxidation peak for P700. For these measurements, we add the couple $Fe(CN)_6^{3-/4-}$ as a redox mediator, since is the mediator that reported a largest photocurrent for PSI[258].

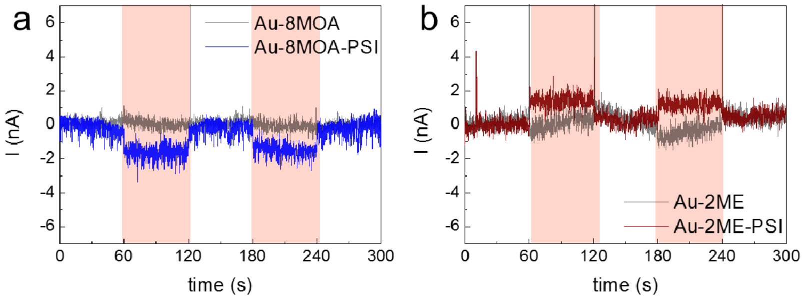

Figure 5.6. Photocurrent generation of PSI onto (a) 8-mercaptooctanoic acid and (b) 2-mercaptoethanol functionalized electrodes. Colored lines corresponds to the PSI measurements and the black one in the background represents the same measurement in the absence of PSI. Light cycles are marked with a red shadow.

The potential was set to U_S = 400 mV vs Ag/AgCl, near the peaks on Figures 5.4 and 5.5. Current traces were substracted a base line for clarity.

In the two different cases, PSI showed current generation upon illumination, indicating that the PSI was successfully immobilized on the electrodes and remained active. The generated photocurrent has a similar magnitude of ~2 nA in both surfaces, which suggest a similar electrode coverage.

5.3.2 SPM imaging

5.3.2.1 AFM imaging.

We used AFM to characterize the adsorption and topography of the PSI molecules onto different surfaces, in order to study and optimize possible immobilization systems for ECSTM experiments. For ECSTM images, we need conductive, flat electrodes. Working with Au electrodes we can achieve ultraflat conductive surfaces, easy to functionalize. Thus, we characterized PSI adsorbed onto gold electrodes, and PSI adsorbed onto functionalized gold electrodes with 2-mercaptoethanol (2ME) and 6-aminohexanethiol (6AH). All images were performed in liquid, in tapping mode.

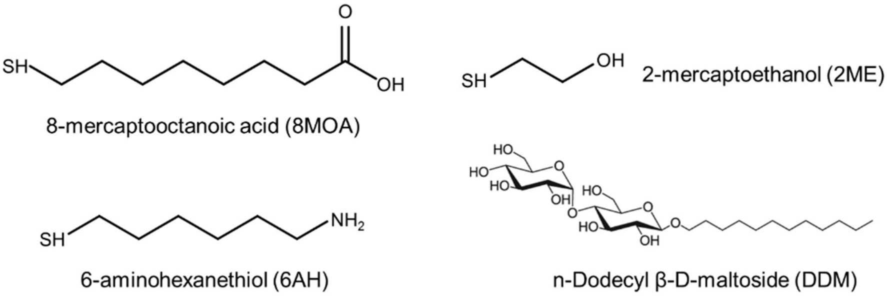

Figure 5.7. Molecular structure of the molecules used to functionalize the Au electrodes [8-mercaptooctanoic acid (8MOA), 2-mercaptoethanol (2ME), and 6-aminohexanethiol (6AH)] and of the surfactant present in the solution to solubilize PSI, n-Dodecyl β-D-maltoside (DDM). 8MOA is a weak acid, and will result in partially negatively charged SAMs surfaces at the working pH (7.4). 6AH is a weak base, thus will create SAMs with a partial positive charge. 2ME will be most likely neutral at the working pH, being able to create hydrogen bonds, and thus resulting in a largely hydrophilic surface.

We first imaged the sample on freshly cleaved mica substrates. PSI adsorbed on mica displays a homogeneous distribution (Figure 5.8). In the images we see bright spots on top of what it seems a sublayer, possibly the surfactant deposited on the mica surfaces. It should be noted that the protein samples for the experiments on mica were not dialyzed. The spots have an average height of ~9 nm, in agreement with its crystallographic height, and diameters of ~100 nm, that most likely corresponds to aggregates of proteins.

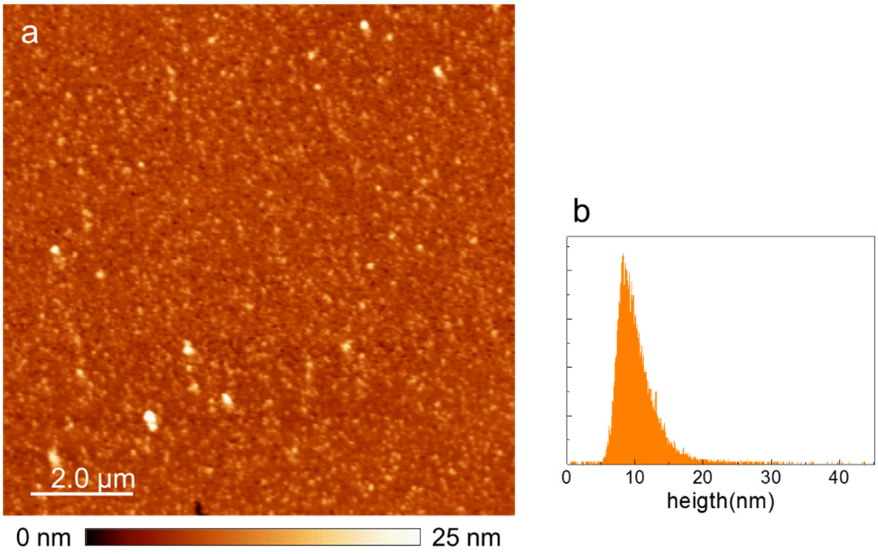

Figure 5.8. a) 10x10 μm^2 AFM tapping image of PSI onto a mica surface. b) Height distribution of image in a.

In the case of bare gold electrode (Figure 5.9) the PSI adsorbed quite homogeneously, but the coverage was lower than on mica. An incomplete layer of film with a height of ~ 1 nm was observed over the gold surface and underneath the protein. On top of it some bigger *islands* of several hundreds of nm^2 area are also observed. This layer and islands most probably corresponds to the surfactant molecules that aggregate on top of the gold forming these structures and double layering on top of it. On top of this layer and inside the *islands* there are bright spots, most likely protein molecules, with ~5 nm height above the islands.

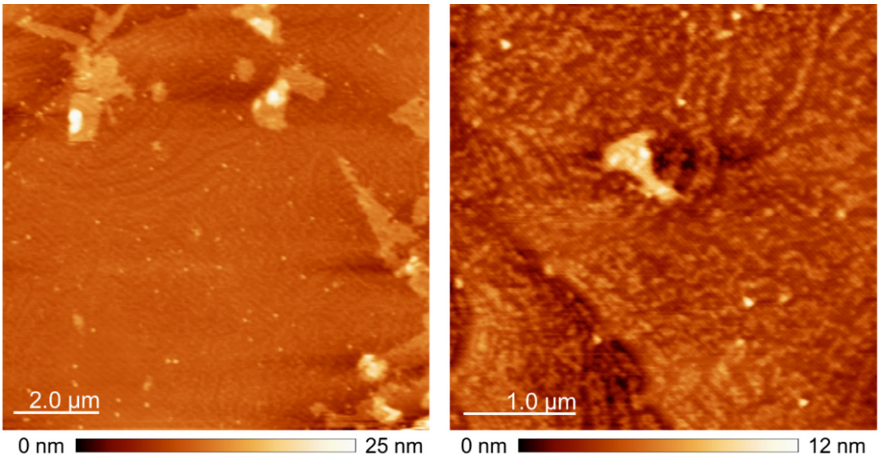

Figure 5.9. 10x10 µm² (left) and 5x5 µm² (right) AFM tapping images of PSI adsorbed onto a bare Au substrate.

PSI showed a better adsorption on the 2ME functionalized surfaces (Figure 5.10). In the AFM images, a monolayer with some holes is observed on the substrate. On top of the monolayer, there are individual bright spots and some patches with bright spots protruding around ~5.5 nm above them. The distribution of these spots is quite homogeneous. There are some *islands* or patches on the surface, but fewer than on gold electrodes, and large areas can be found without them. The patches have a height of ~4.5 nm, and the diameter of the spots is around 120 nm, bigger than on mica, which is probably an indicative of protein agglomerates. Thus, PSI adsorbs quite uniformly on the 2ME functionalized surfaces despite the formation of aggregates.

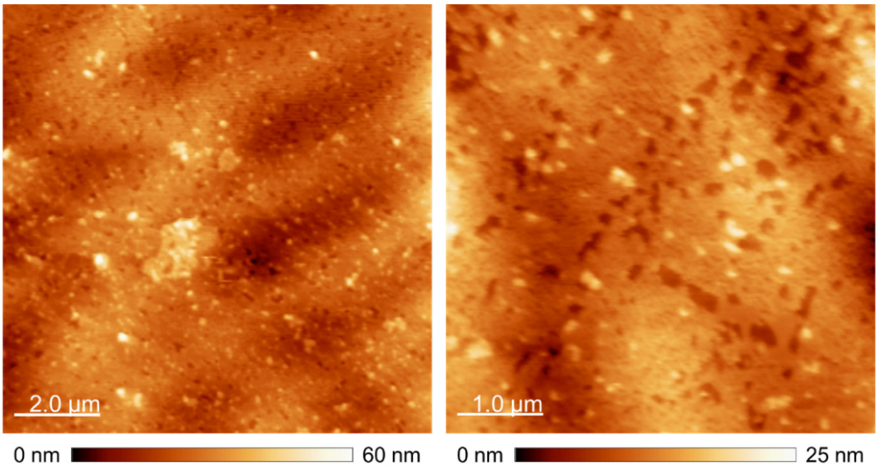

Figure 5.10. 10x10 μm^2 (left) and 5x5 μm^2 (right) AFM tapping images of PSI adsorbed onto 2-mercaptoethanol (2ME) functionalized Au electrodes.

Characterizing the 6AH SAM functionalized electrodes, (Figure 5.11) we found plenty of material adsorbed on top of the monolayer. The surface appears quite homogeneous, but the roughness is higher than in the Au electrode or the 2ME surface. It seems again that there are some surfactant islands or agglomerates, with protein protruding above them. Protein bumps show a height of ~10 nm, close to the crystallographic one, but appear in agglomerates of 110-140 nm, and they are hard to distinguish from the rough background.

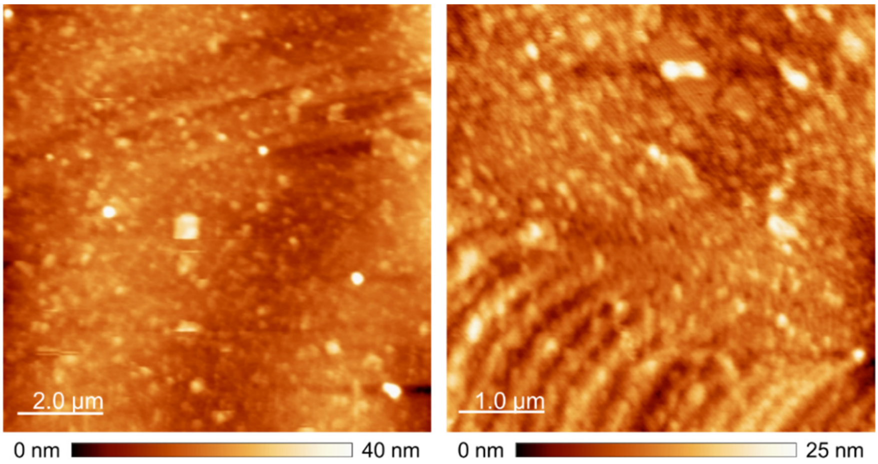

Figure 5.11. 10x10 μm^2 (left) and 5x5 μm^2 (right) AFM tapping images of PSI onto 6-aminohexanethiol functionalized electrodes.

PSI protein adsorbed on the three systems gold electrode surfaces, but adsorption was more abundant and homogeneous on the functionalized gold surfaces, both the 2ME and the 6AH SAM. In the 6AH functionalization, PSI created a rougher surface than in the 2ME one, where the sample appears more homogeneous, only creating patches or multilayers locally.

ECSTM imaging

For ECSTM imaging we used 4 different systems: the three gold surfaces we had imaged with AFM (PSI adsorption on bare gold, on 2ME, and on 6AH functionalized gold) and another SAM functionalization: 8-mercaptooctanoic acid (8MOA). This way we have, besides the bare gold surface, neutral, positively, and negatively charged functionalizations (Figure 5.7). We imaged the different systems with different potential and bias conditions.

In the case of the bare gold, PSI has a good adsorption on the surface. In the images (Figure 5.12a) we see the flat surface of the gold crystal and on top of it bright spots that seem to be individual proteins of around 10 nm diameter. In the images with higher resolution we can distinguish a sublayer behind this small spots. This sublayer or film has an apparent height of around 0.1 nm. This sublayer, that appears forming patches or islands, most likely is constituted by the surfactant forming agglomerates. To confirm this, we incubated a single crystal with buffer and surfactant, following the same procedure we followed when we incubated PSI. In Figure 5.12b, we can see that the surfactant causes this kind of islands. Sometimes we see some protrusions, probably due to double layering.

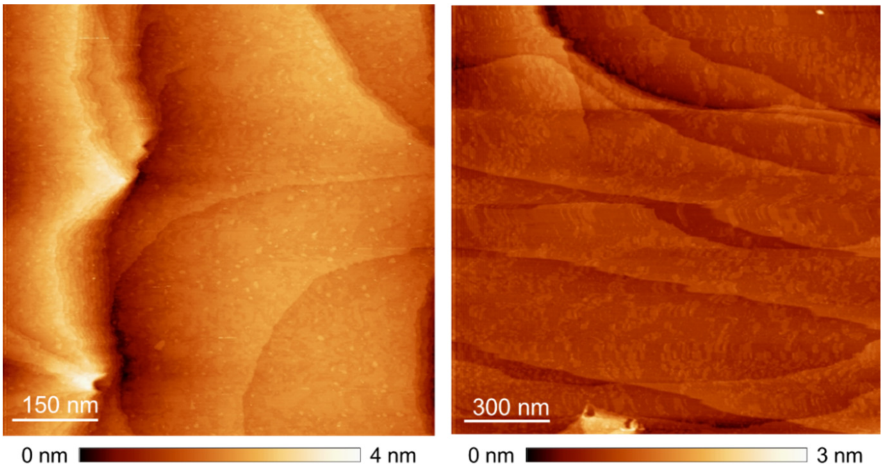

Figure 5.12. a ECSTM image of PSI onto gold electrode. b ECSTM image of DDM surfactant onto gold electrode. Both images were acquired with U_S=200 mV, U_P = -100 mV, current setpoint I =0.5 nA.

In the PSI images, the protein protrudes around 0.4 nm above this film. This apparent height under constant current mode at the indicated potential is tenfold lower than the crystallographic size of PSI, in agreement with the apparent height of the protein complex reported with STM in the literature[184].

We imaged the same sample with modified potential conditions. First, we imaged the system keeping a fixed sample potential, and varied the probe potential thus modifying the bias potential (Figure 5.13). Neither the apparent height of the film or the bumps changed significantly with the bias applied (Figure5.13d).

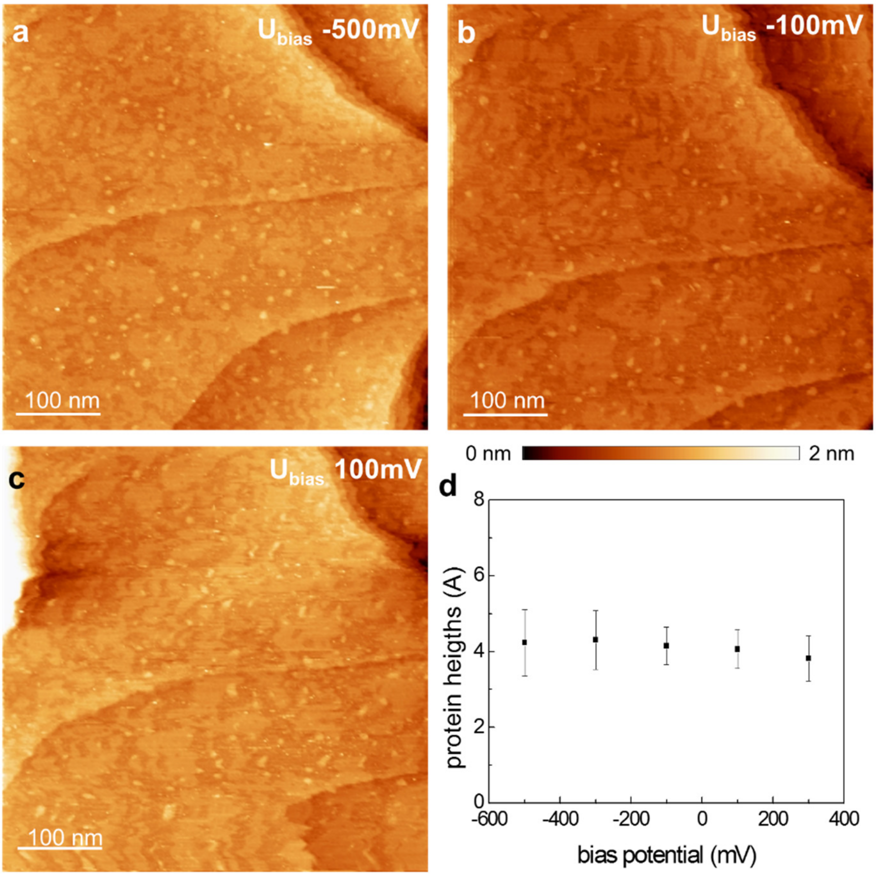

Figure 5.13. a,b,c ECSTM images of PSI on a Au electrode obtained with U_S=200 mV, with U_{bias}= 500 mV, -100 mV, 100 mV respectively. Setpoint was I=0.5 nA. d)Average protein apparent heights obtained at different bias.

We also imaged the system keeping a constant negative bias, but changing the applied sample potential (Figure 5.14). In this case the height of the bumps above the film have a small but significant change with the applied sample potential. It starts weakly increasing at U_S= 400 mV, and keeps increasing at U_S =600 mV, were the spots seem to be 0.5 Å higher. This process is reversible, as shown in Figure 5.14d (red spots correspond to images obtained at U_S=200 mV, 400 mV after applying U_S=600 mV).The PSI oxidation peak starts around 350 mV (Figure 5.3), thus differences in the apparent height of the PSI at these values can be expected, as a result of changes in the protein's oxidation state and charge availability at these potentials.

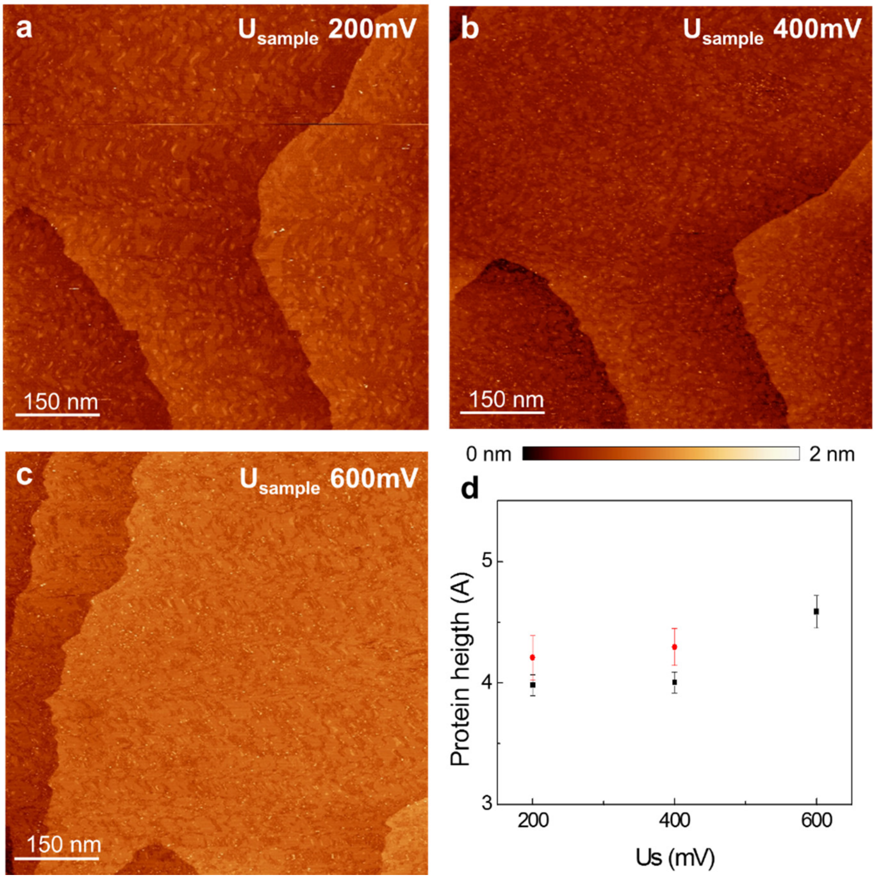

Figure 5.14. a,b,c ECSTM images of PSI on a Au electrode. Images were obtained at U_S=200 mV, 40 0mV and 60 0mV respectively, keeping U_{bias}= -300 mV. Setpoint was 0.5 nA. d) Average protein apparent heights obtained at different U_S. Black dots correspond to the heights obtained imaging a new sample, red dots correspond to a sample already imaged at U_S=600 mV.

PSI incubated onto a 2ME functionalized electrode, shows a great increase in the adsorption (Figure 5.15). The surface appears almost completely covered with small dots that seem the individual PSI complexes. These molecules are on top of a layer that could be the surfactant or the functionalization SAM. We see some holes in this layer but in general it is a complete homogenous monolayer. This system was imaged at the same sample potentials of the previous case, with a negative and a positive bias for each sample potential (Figure 5.15).

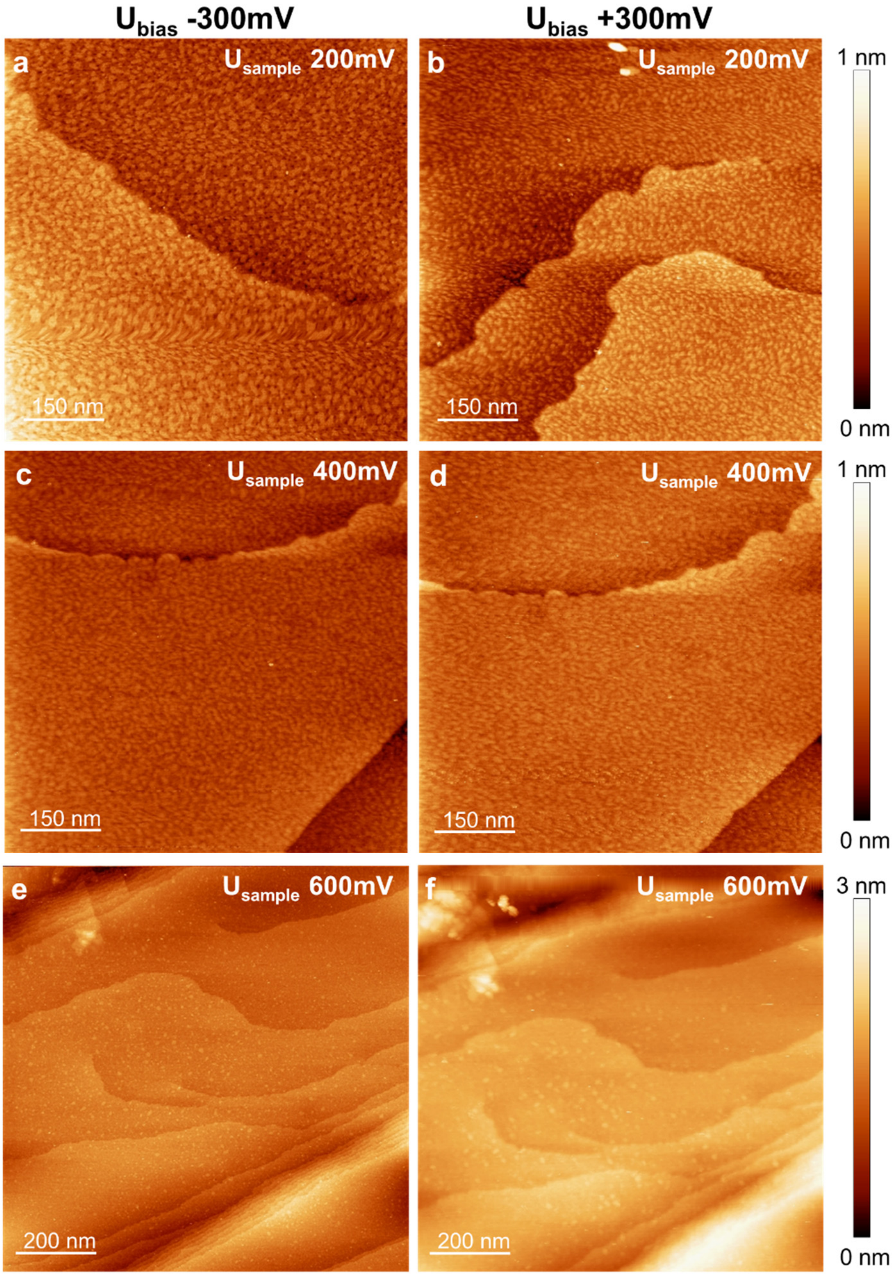

Figure 5.15. ECSTM images of PSI on a 2-mercaptoethanol functionalized Au electrode. Images were obtained at U_S=200 mV(a,b), 400 mV (c,d)and 600 mV (e,f) respectively, with a negative (U_{bias}= -300 mV, left panel) and positive bias (U_{bias}= +300 mV, right panel). Setpoint was always kept at 0.5 nA.

In all the conditions, the bumps are lower than in the bare-gold case, but the diameter is similar. Apart from U_S=600 mV, no significant difference is observed between the images acquired with positive or negative bias. In the case of U_S=600 mV, when the bias is positive, the U_P= 900 mV and the probe does not withstand properly this potential, hence the quality and resolution of the image gets compromised. Thus, we see lower spots, but bigger in diameter. We attribute these differences in the images to the tip changing its imaging capacities and not to an electrically- induced deformation of the sample. For the different applied U_S, for both positive and negative bias, the apparent height of the bumps appears lower at U_S= 400 mV (Figure 5.16), but goes up at U_S =600 mV. The apparent height is measured above the background layer.

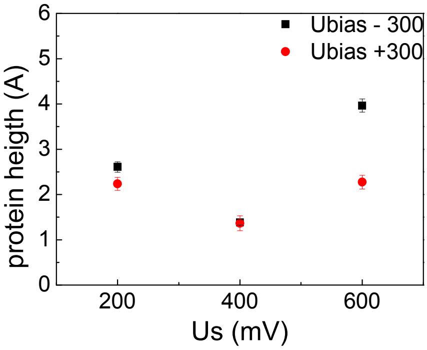

Figure 5.16. Apparent ECSTM height dependence of PSI on 2mercaptoethanol functionalized gold electrodes with Us. Red dots for positive bias, black dots for negative bias.

Working with the 6AH functionalized gold there is a similar situation to PSI incubated onto bare gold. The images show islands probably formed by surfactant molecules that surround protruding proteins (Figure 5.17). The adsorption is uniform but less efficient than with 2ME, and leads to a lower protein density. The diameter is similar to the other surfaces (around 10 nm) and does not change with the applied sample potential. The heights of the protrusions are comparable to the ones found in gold surfaces (0.3-0.4 nm). In this case the dependence with the potential is less pronounced. The protein bumps appear significantly higher as we increase the applied sample potential at U_S>400 mV as in previous cases, but the difference is smaller.

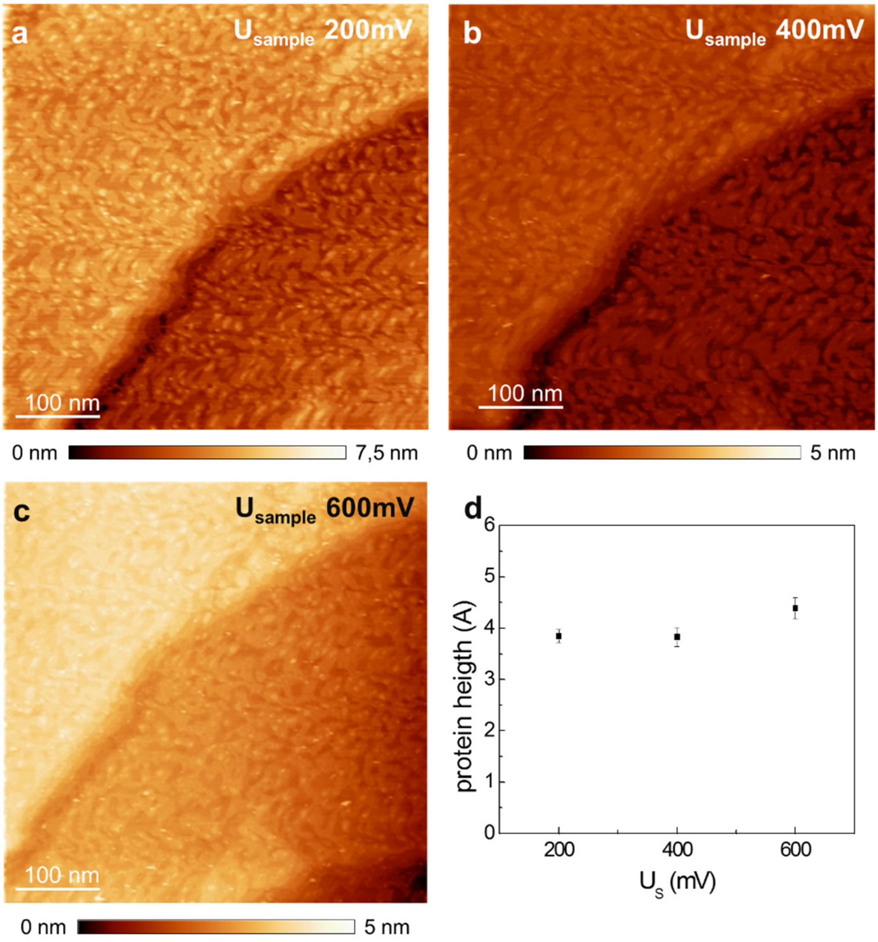

Figure 5.17 a,b,c ECSTM images of PSI on an aminohexanethiol functionalized Au electrode. Images were obtained at U_S=200mV, 400mV and 600mV respectively, keeping U_{bias}= -300 mV. Setpoint was 0.5nA. d) Average protein apparent heights obtained at different U_S.

The structure of the surfactant islands is not altered with the potential applied to the sample. In Figure 5.18 the evolution of two individual proteins with the applied potential is shown in an enlarged region. Neither the height nor the diameter change significantly as the sample potential is increased. At U_S =850 mV the image gets very noisy and the imaging gets compromised, but underneath the noise, we can distinguish the structure of the surfactant and the proteins, which maintained its structure when we returned to lower potentials.

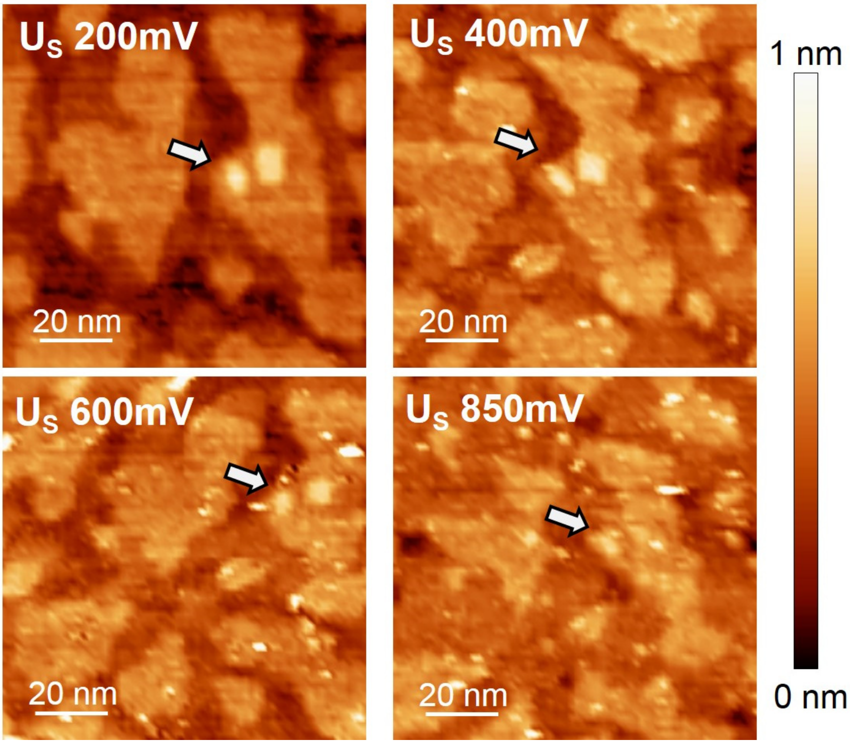

Figure 5.18 Enlarged ECSTM images of PSI on 6-aminohexanethiol functionalized Au electrodes obtained at U_S= 200 mV, 400 mV, 600 mV,850 mV respectively, keeping U_{bias}= -300 mV. Setpoint was 0.5 nA. Two individual proteins are indicated with a white arrow.

PSI also adsorbs well on 8MOA functionalized surfaces. The images show the flat gold surface covered with small protein bumps, distributed in a homogeneous way (Figure 5.19). The protein spots are smaller in diameter than in the other surfaces (~8 nm) but they show a similar apparent height (~0.4 nm).

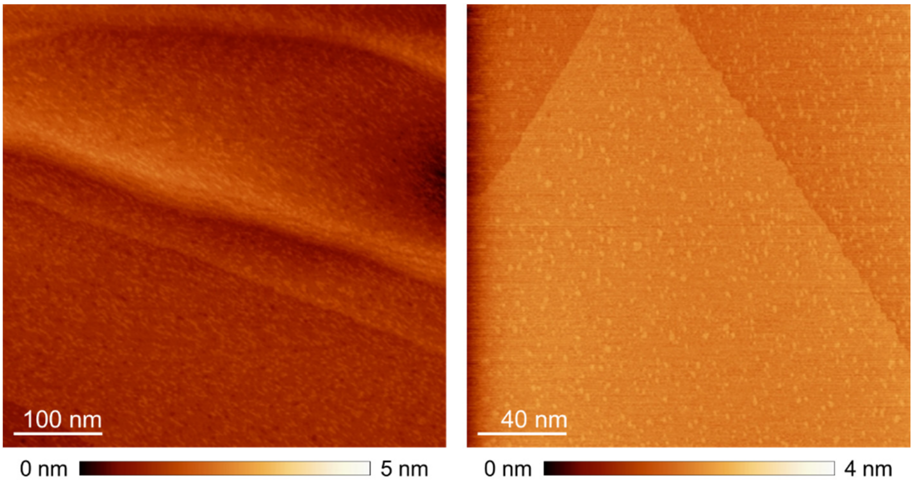

Figure 5.19 ECSTM images of PSI on a mercaptooctanoic acid functionalized Au electrode. Images were obtained at U_S=200 mV and U_{bias}= -300 mV. Setpoint was 0.5 nA.

5.3.3 PSI adsorption on the different surfaces.

All systems used here for PSI immobilization are based on physical interactions, which are unspecific in the sense that there is not a specific anchoring point targeted in the protein. PSI molecules adsorbed on all the systems, but the quantity and distribution changed depending on the surface properties of the functionalized substrates.

PSI molecules adsorbed quite homogeneously onto bare gold electrodes. The proteins appear surrounded by surfactant islands. This happened also in the 6AH SAM, but not in the 8MOA or the 2ME, where the adsorption of PSI was higher. PSI onto gold and 6AH seem also to have a similar behavior with respect to the sample potential, i.e. an increase in apparent height under oxidizing conditions. PSI is known to adsorb onto bare gold electrodes with mixed orientations[244]. The interaction of PSI with 6AH is not very clear. The surface charge of PSI and the absence of specific attachment points suggest that the nature of the interaction is most likely electrostatic, and in principle we could expect that the partially positive charge of the surface would attract the negatively charged residues of the protein. Nevertheless, it has been reported[259] that amino-terminated SAMS in presence of inorganic phosphates could adsorb phosphate molecules from the buffer solution, creating a layer over the SAM surface that would over compensate the partial positive charge of the SAM. This could result in a SAM with heterogeneous electrostatic properties, that causes in turn mixed orientations of the protein, and less adsorption due to electrostatic neutrality.

PSI is known to have a good adsorption on hydroxyl terminated SAMs[141, 185, 251, 252] through hydrogen bonding, with a homogeneously oriented population. It has been reported that the 70% of the PSI would be oriented with its ET chain vector perpendicular to the surface, although there is some controversy concerning if the PSI ET chain is pointing upwards[185] or downwards[141].The appearance of the AFM and ECSTM images indicates that PSI adsorbs homogeneously on the 2ME surface, but do not allow clarifying the orientation of the molecule.

On 8MOA functionalized surfaces, PSI molecules adsorbed in an abundant and homogeneous way. PSI and its reaction center has been reported to adsorb well on negatively charged surfaces[141, 185]. The interaction is more likely electrostatic, with the partial negatively charged surface attracting the positive residues on the protein surface. Although the positive charges are distributed on the surface of the protein, one region candidate for the interaction with the negative surface would be the positively charged patch in the lumen part of the protein that is the binding site for negatively-charged Plastocyanin[51].

5.4 Conclusions

In this chapter, we studied the immobilization of PSI molecules on four different electrode surfaces based on gold single crystals: a bare, atomically flat gold electrode, and 2ME, 6AH, and 8MOA SAM functionalized electrodes. Both AFM and ECSTM imaging showed that PSI successfully bound to all these surfaces, yet to different extents.

The systems that showed highest coverage and more homogeneous adsorption were the 2ME and the 8MOA functionalized electrodes. PSI retained its electrochemical activity in both, and produced photocurrent generation upon illumination on the two surfaces. PSI also adsorbed onto bare-gold electrodes and 6AH functionalized gold electrodes, but with a low coverage of the surface and a heterogeneous adsorption, creating islands and aggregates of the protein and/or the surfactant over the surface.

The four systems were suitable for ECSTM imaging, three of them in a variety of sample potentials. The apparent height of the PSI molecules is in agreement with reported values in the literature[184]. The apparent height of PSI was independent of the applied bias, but it changed with the applied sample potential (U_S). Imaging above U_S>400 mV, the average apparent height of the protein spots increased about a 10% (~0.5 Å). This suggests that the ET transfer mechanism has redox dependent steps, which can be elucidated with further ECTS experiments.

6

Characterization of PSI: tunneling spectroscopy

6.1 Introduction

PSI acts as a photodiode, an electrical rectifying contact or diode, with a directional electron transport chain that goes from the P700 reaction center up to the ferredoxin docking side (Figure 6.1). Upon light illumination, the P700 center is photoexcited to P700*. The excitation of an electron to this high-energy state leaves an electron vacancy (hole) in P700, which is transferred to plastocyanin. The high energy electron in p700* is rapidly transferred through the cofactor chain A_0-A_1-F_X-F_A-F_B, which is arranged in a potential cascade over a distance of several nm, separating this way the charges and thus preventing electron-hole recombination.

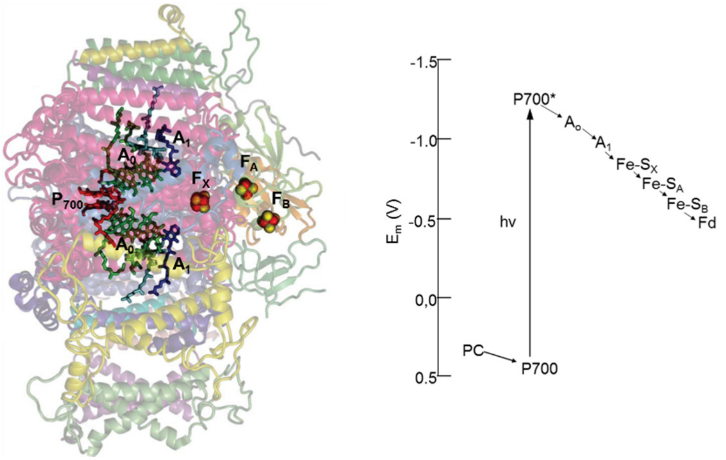

Figure 6.1. a)Side view of PSI structure showing the co-factors involved in the ET chain (adapted from ref [31]). b)Energy diagram of photochemistry and early electron transfer reactions in PSI (adapted from ref[47])

PSI electron transfer process has been studied with STS[184, 185] and c-AFM[141] in air, which confirmed its diode-like, rectifying behavior. PSI shows a transport efficiency across more than 7nm distance[140], and shows temperature independence over a wide range of temperatures (160-320K)[141]. These results suggest a tunneling based mechanism, but the distance exceeds the maximum length for tunneling observed for organic molecules[142].

With ECSTM and, more precisely, current distance ECTS, we can characterize each one of the functionalizations discussed in the previous chapter and measure directly the distance decay current factor β by measuring the current flowing between the electrodes while increasing the distance between them[105, 187]. In systems that can be described by a Metal|Insulator|Metal model, β is directly related to the effective tunneling barrier height in the tunneling process,[187, 260] which can give us an insight into the charge transfer mechanism.

We investigated the current-distance dependence for all substrates studied in chapter 5. We studied each system as a function of applied sample potential and the potential bias with respect to the probe. Finally, we performed some preliminary experiments examining the influence of light illumination in the current decay factor.

6.2 Experimental methods

Sample preparation.

The PSI samples were provided by Dr. Emilie Wientjes and were prepared as described in the previous chapter.

Electrode preparation, functionalization and PSI incubation were carried out as described in the previous chapter.

Current-distance (IZ) measurements

IZs measurements were performed in our local setup PicoSPM Microscope Head and a Picostat Bipotentiostat (Molecular Imaging) controlled by Dulcinea electronics (Nanotec Electrónica). Data were acquired using WSxM 4.0 software[190] and analyzed with Origin. Current-distance curves were recorded at different U_P and U_S potentials. Current setpoint was in all cases set to 0.5 nA. When the probe was in range and stable, we proceed to launch the IZs. To run the curves the feedback was momentaneously disabled. The probe was then retracted 5 nm at a speed of 8 nm/s and approached again to the surface. The feedback was enabled between ramps. Ramps were taken in different areas of the surfaces to ensure a heterogeneous data collection. As the feedback is disabled to run the curves, ramps that started with a deviation higher than 10% of the set point were discarded. The curves were then fit to an exponential function $I(z) = Ae^{-\beta x}$, ($r^2 \geq 0.95$) to obtain the decay factor β. Measurements under illumination were performed with a high luminosity (400 mcd) red LED (Ariston Electrónica) attached to the ECTSM cell.

6.3 Results and Discussion

6.3.1 Current –distance (Iz) curves.

We studied the current-distance behavior of PSI onto the 4 substrates studied in chapter 5. In all systems, the current decayed exponentially till it reached the faradaic current values of the tip far away from the sample. Fitting the exponential part of the curves, we obtained the distance decay factor β for all the systems, and evaluated its dependence with the applied sample potential, at positive and negative bias. In most cases we obtained β values lower than for metallic surfaces, in correspondence with the ones obtained for ET proteins[105]. However, these β values varied with the potential and bias conditions in different ways for each immobilization surface.

PSI adsorbed onto bare gold electrodes gave low β decay constants for all used potentials and bias. In Figure 6.2a, the Iz curves are shown (raw data) of the system for different sample potentials at positive and negative bias, superimposed to the control curves obtained in absence of the protein. In Figure6.2b we see the statistics of the β values of the same curves, superimposed again over the control statistics. Relatively low β values (3-5 nm^{-1}) are observed in all conditions and do not show a strong dependence with US and bias. However, a small difference is found when the applied sample potential is U_S=200 mV, and the bias potential is negative. Although the average β ~4 nm^{-1} value (peak of the histogram) is on the same order as the ones obtained for the other sample potentials, the distribution in this case is wider, and there are curves that attain β<1 nm^{-1}. They can be observed in the raw I-z curves as having a slow decay (red curves, top red panel). No other significant changes were observed with the sample potential or the bias.

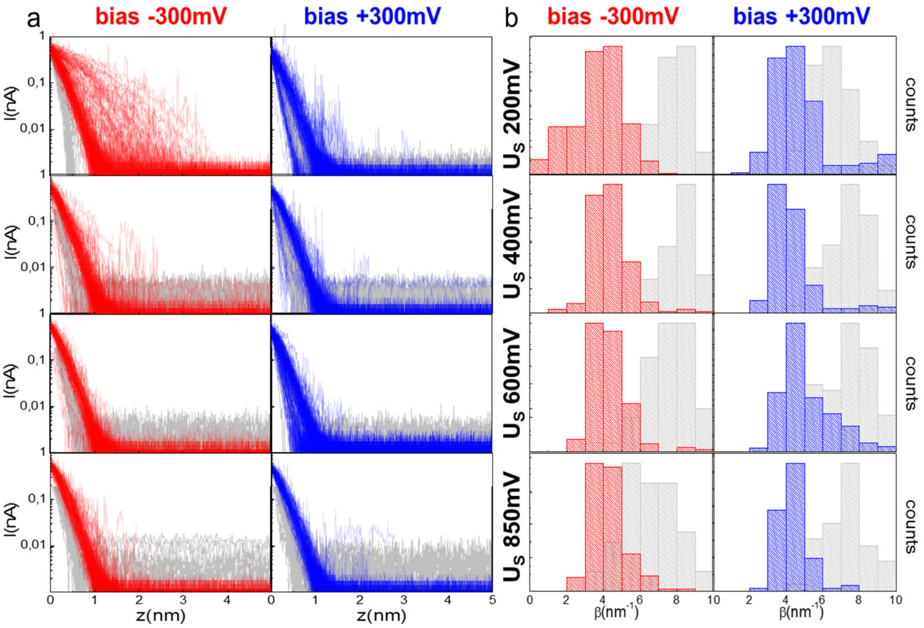

Figure 6.2 a) IZ curves for PSI onto bare gold electrodes (raw data) obtained for different sample potentials (U_S = 200mV, 400 mV, 600 mV, 850 mV, going up to down) and positive (blue) and negative(red) bias. Grey curves correspond to curves obtained in the same conditions in absence of PSI. b) Statistical representation of the obtained β values for the curves in a. current setpoint was always 0.5nA.

PSI bound to the 2ME electrode showed a different behavior (Figure). Low β values (down to 3 nm^{-1}) are found in all the conditions, but at low sample potentials (U_S=200 mV) high β values predominate. As the sample potential is increased for both positive and negative bias, low β values are more abundant than high β values. Although both bias display a similar behavior, it is more robust at positive bias where the high β peak is almost gone when increasing the sample potential to U_S=400 mV.

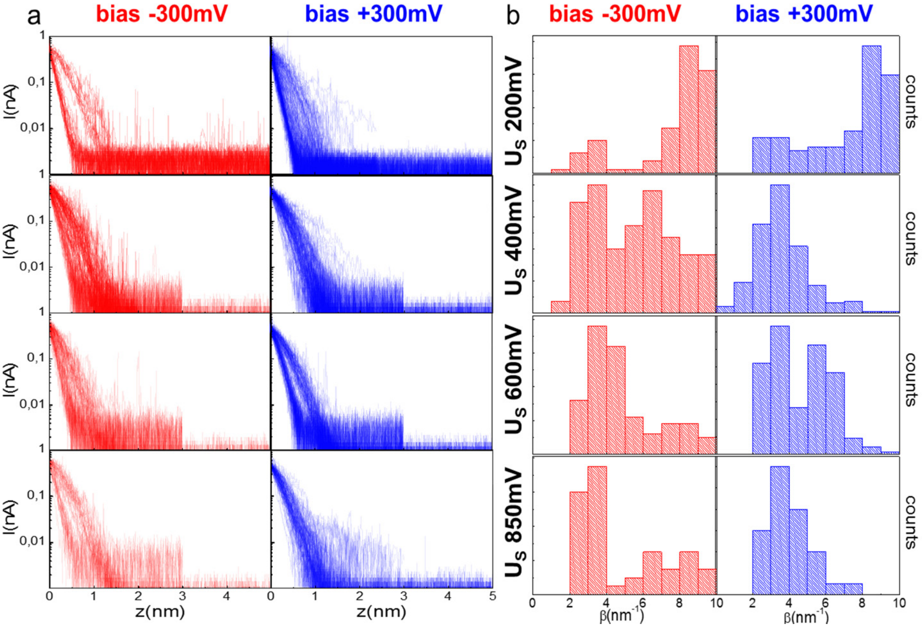

Figure 6.3. a) IZ curves for PSI onto 2-mercaptoethanol functionalized gold electrodes (raw data) obtained for different sample potentials (U_S = 200 mV, 400 mV, 600 mV, 850 mV, from top to bottom) and positive (blue) and negative(red) bias. b) Statistical representation of the obtained β values for the curves in a. Current setpoint was always 0.5 nA.

Focusing in the range of lower β values ($\beta<4nm^{-1}$) (Figure 6.4) we see that they are present in all the conditions, and that the β values ~$4nm^{-1}$ don't show a dependence with sample potential or bias. However, there is a larger population of low β curves at U_S= 400 mV and positive bias (Figure 6.3). In these conditions there are I-z curves that achieve very low β values, even forming a small peak at β~ 1.2 nm^{-1} (Figure 6.4). The appearance of this super low β value peak is clearly conditioned by the sample and bias potential.

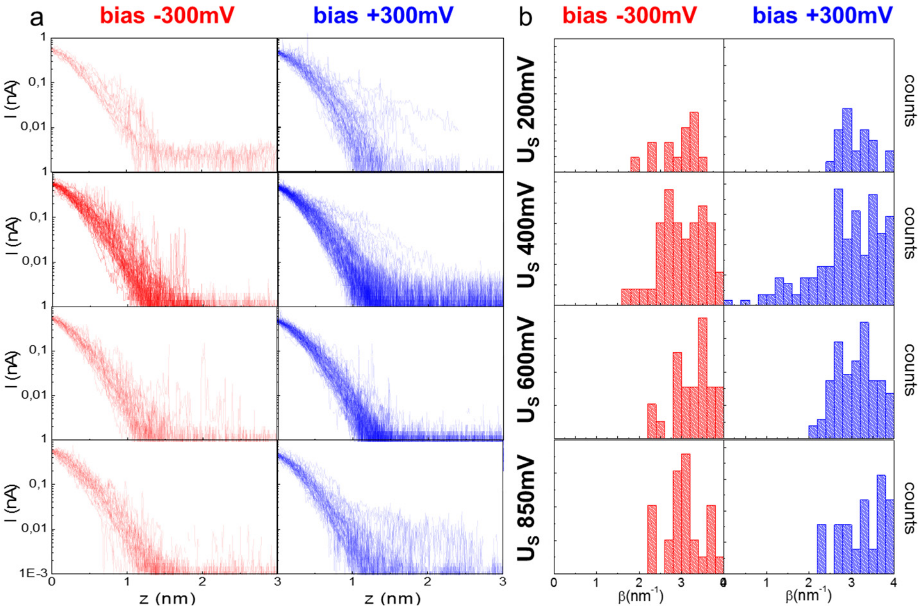

Figure 6.4. Distribution of Iz curves with β <4 nm^{-1} for PSI onto 2-mercaptoethanol functionalized gold electrodes. a) Selected Raw I-z curves corresponding to beta<4nm^{-1} are indicated in red and blue (bias -300 and +300 mV respectively). b) Enlarged histograms from Fig. 6.3b for the beta<4nm^{-1} region, including higher resolution binning. The lowest values of the distance-decay constant are found for U_S=400 mV and bias +300 mV and form a peak at β~1.2 nm^{-1}. Current setpoint was always 0.5 nA.

In the case of PSI bound to the 6AH SAM functionalized electrode, we see a wide distribution of β values in all of potentials and bias (Figure 6.5). There is nevertheless a disguised peak at β~4 nm^{-1} for U_S =200 mV, 400 mV, 600 mV at negative bias that does not appear at positive bias. The broad distribution of β values is an indicative of a mixture of orientations, although the small tendency towards high β values in the negative branch suggests that one orientation is quite more abundant than others. This kind of distribution could also be due to a low absorption of the protein, since there is a high contribution from the background.

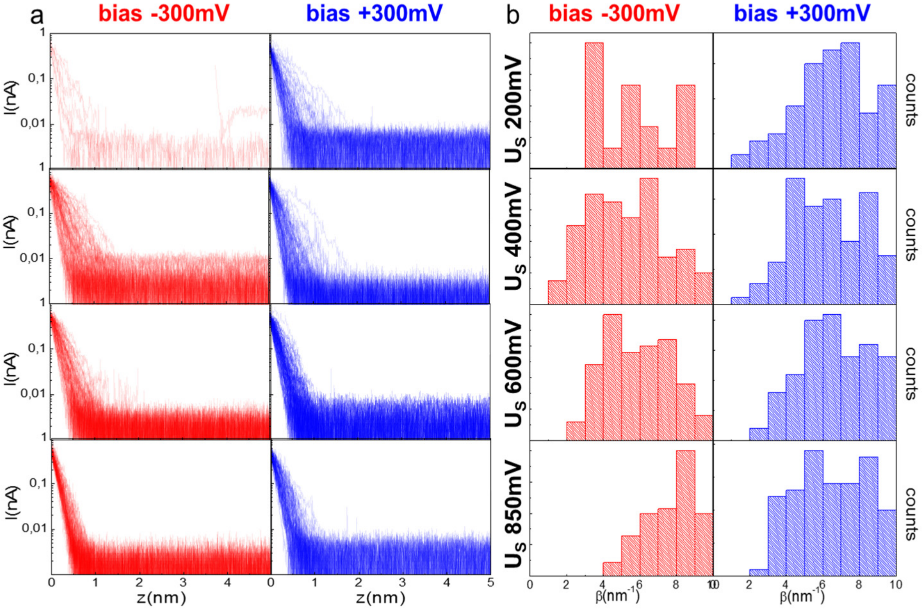

Figure 6.5. a) IZ curves for PSI onto 6-aminohexanethiol functionalized gold electrodes (raw data) obtained for different sample potentials (U_S = 200 mV, 400 mV, 600 mV, 850 mV, From top to down) and positive (blue) and negative (red) bias. b) Statistical representation of the obtained β values for the curves in a. current setpoint was always 0.5 nA.

The system of PSI bound to 8MOA SAM was the one that showed lower β values (Figure 6.6). In this case, there is a clear tendency to higher β values at higher sample potentials for both positive and negative bias. We see low the peak corresponding to β ~ 4 nm^{-1} disappear at U_s=850 mV for negative bias, and at U_S=600mV for the positive bias. Focusing in the lower beta values (β<4 nm^{-1}) (Figure 6.6), we see that there appear again curves with values of β~1 nm^{-1} at U_S = 200mV for both bias and, at U_S= 400 mV for positive bias.

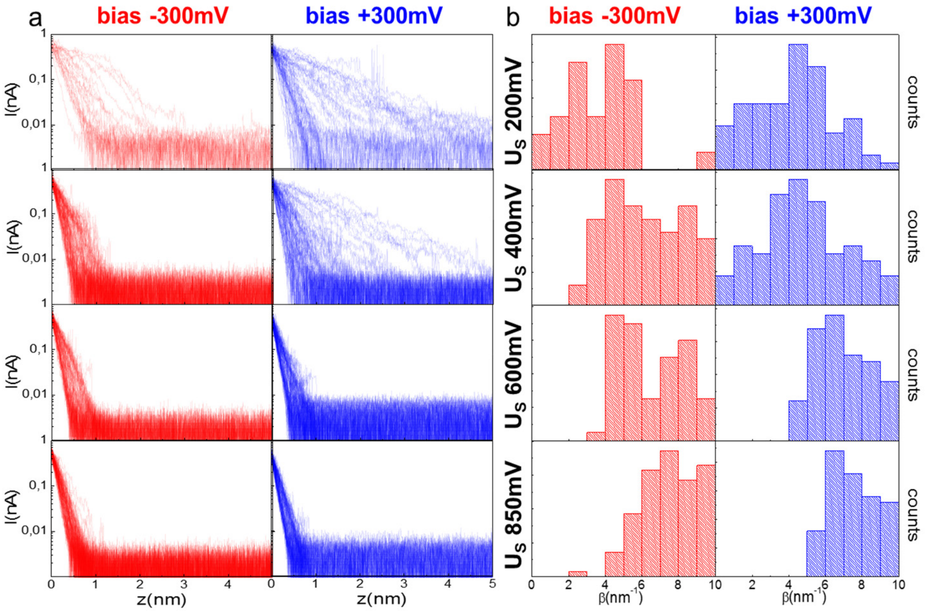

Figure 6.6. a) IZ curves for PSI onto 8-mercaptooctanoic acid functionalized gold electrodes (raw data) obtained for different sample potentials (U_S = 200 mV, 400 mV, 600 mV, 850 mV, from top to down) and positive (blue) and negative(red) bias. b) Statistical representation of the obtained β values for the curves in a. current setpoint was always 0.5 nA.

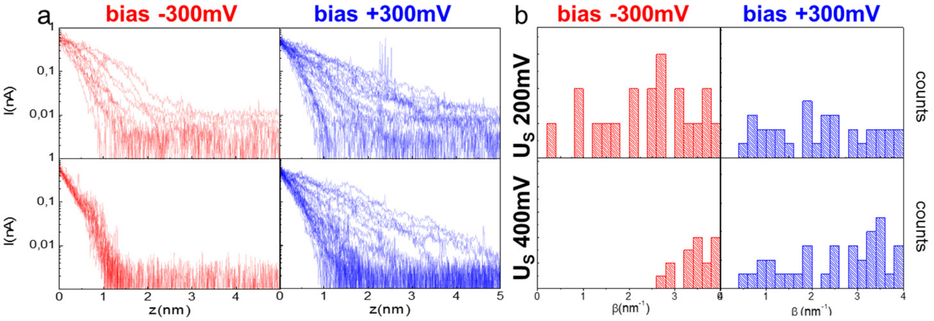

Figure 6.7. Distribution of Iz curves with β <4 nm^{-1} for PSI onto 8-mercaptooctanoic acid functionalized gold electrodes a) Selected Raw I-z curves corresponding to β<4 nm^{-1} are indicated in red and blue (bias -300 and +300 mV respectively). b) Enlarged histograms from Fig. 6.6b for the β<4 nm^{-1} region, including higher resolution binning. Current setpoint was always 0.5 nA.

In the four different immobilization systems we found curves with a low distance decay factor of β ~ 4 nm^{-1}, in the same range of previously others obtained for ET proteins[105]. In some cases we found, besides this peak, anomalously low β values up to β~1 nm^{-1}, which have never been reported in inter-protein ET and cannot be accounted for by multiple tunneling steps through the aqueous solution. In an ongoing investigation in our laboratory (A. Lagunas, in preparation), such low β values have been observed between redox partner proteins bound to the probe and sample of the ECSTM, and have been associated to strong electronic coupling that maintains efficient ET at long distances through the aqueous solution.

In order to interpret the experiments of chapters 5 and 6, a table is presented below that outlines the major results (table 6.1). It includes for each substrate (bare Au, 2ME/Au, 6AH/Au, 8MOA/Au) the distribution of β values as a function of the substrate potential and probe-sample bias, the minimum β values observed (β around 1 nm^{-1} corresponding to Long range electron transfer, LRET, are indicated with a yellow arrow), the extent of surface coverage by PSI, and the apparent PSI height measured by ECSTM at different potentials and bias.

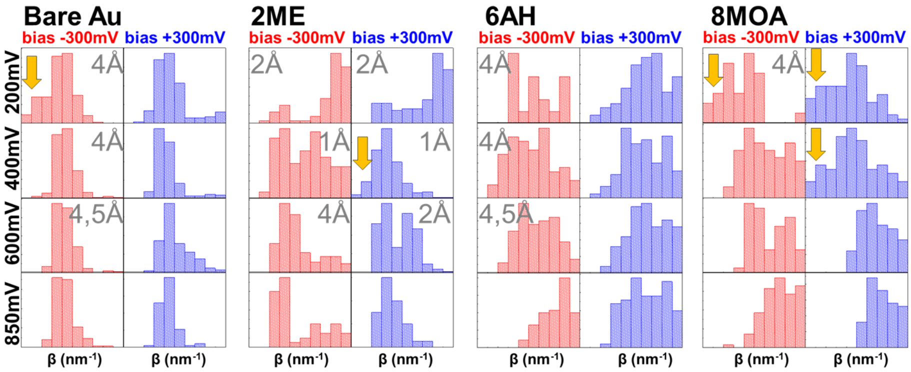

· Intermediate β values independent of U_S and bias.	· β values strongly dependent of U_S: β lower at high U_S.	· Intermediate β values weakly dependent on U_S.	· β values strongly dependent of U_S: β lower at low U_S
· β=1 nm^{-1} at U_S=200, bias -300 (weak LRET)	· β=1nm^{-1} at U_S=400, bias +300 (weak LRET)	· Low β at U_S=400-600, bias -300	· β=1 nm^{-1} at U_S=200-400, bias ±300 (strong LRET)
· Low coverage PSI	· High coverage PSI	· Low coverage PSI	· High coverage PSI
· High apparent height by ECSTM (4-4.5 Å)	· Low aparent heigth by ECSTM	· High apparent height by ECSTM (4-4.5 Å)	· High apparent height by ECSTM (4 Å)

Table 6.1. Summary of the results for the different functionalization. Histograms (top of the table) show the distribution of β values of each surface at different values of U_S and U_{bias}. Long range electron transfer regions are marked with a yellow arrow. Average apparent heights of the PSI molecules measured with ECSTM at different U_S are specified in grey in the histograms.

Many observables change with several parameters and thus it is useful to represent them in a compact way in order to establish comparisons. In Figure 6.8, the distribution of β values is shown in the y-axis with a color code (brighter for higher occurrence of I-z curves with that β value) as a function of U_S (x-axis) and bias (red and blue plots for -300 mV and +300 mV respectively). This representation of distance-decay constants or “beta-gram” can be used to interpret ET using the lower part of the plot. Values of β >10 nm^{-1} correspond to abrupt (metal-like) exponential drops between electrodes, as for the DDM surfactant alone on gold, which also does not depend on U_S. Despite the relatively low coverage of PSI, the simplest system appears to be PSI on a bare gold electrode. The β values do not depend strongly on potential changes and a region of the betagram corresponding to very low β values is clearly visible at U_S=200 mV and negative bias. The 6AH SAM gives the blurriest distribution of β values, suggesting low adsorption, as high β values are predominant. Some regions of interest in three of the electrodes are highlighted in Figure 6.9.

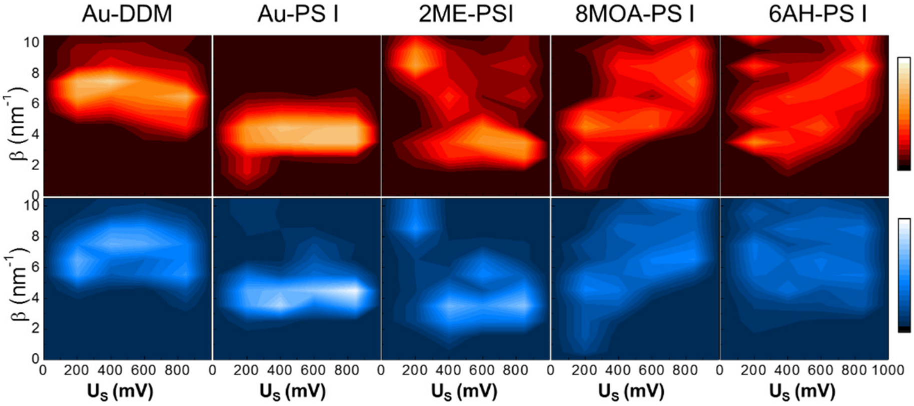

Figure 6.8. 2d-histogramms showing the evolution of the beta values with the U_S for the different systems at negative (red) and positive (blue) bias. Normalized counts follow the color scales (right).

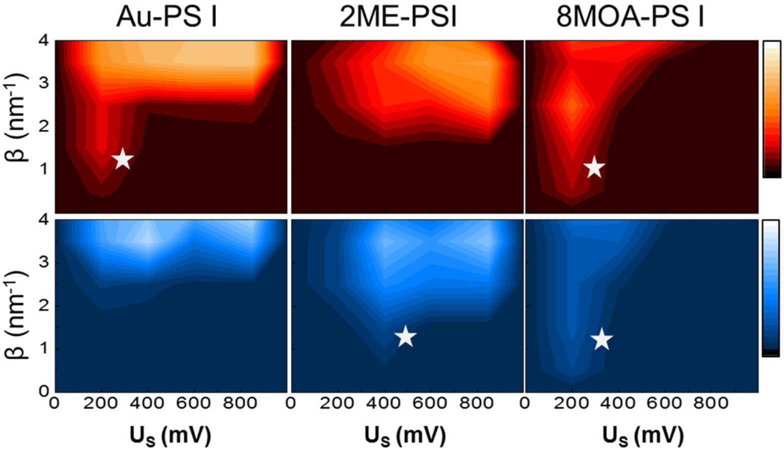

Figure 6.9. Enlarged 2d-histogramms showing the evolution of the beta values with the U_S for the beta<4nm^{-1} region, for the different systems at negative (red) and positive (blue) bias. Normalized counts follow the color scales (right). Stars indicate conditions of LRET (β=1nm^{-1}).

The interpretation of results is also facilitated by electron energy diagrams like that of PSI in Figure 6.1. The set of potentials applied in our experiments are shown in Figure 6.10. The potential conditions (U_S, U_P) in which LRET between probe and sample is observed (stars in Figure 6.9) correspond to the energy diagrams depicted in Figure 6.11.

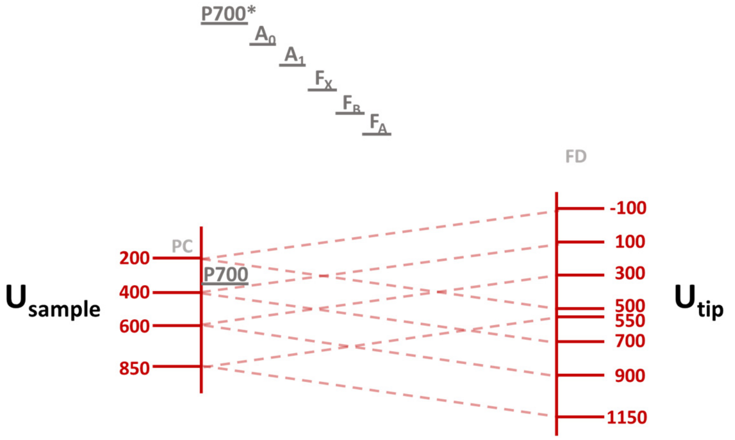

Figure 6.10. Energy diagram showing the used sample and tips potentials, including the energy diagram of the cofactors of the PSI biological ET chain. As reminder, $U_{bias}=U_P - U_S$, two bias potentials were used in ECTS experiments in this chapter (+/-300 mV).

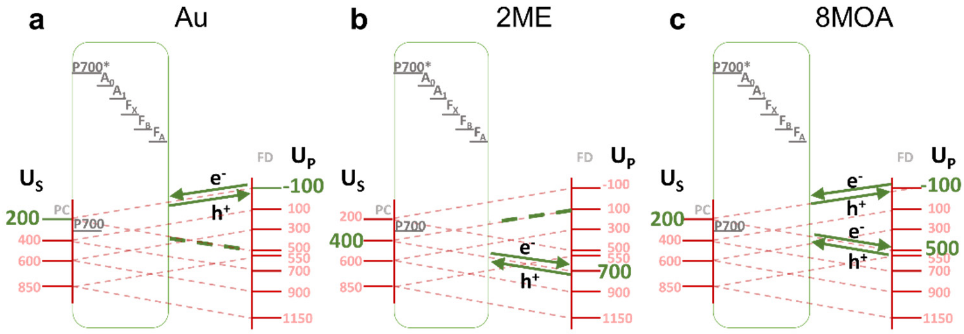

Figure 6.11. Energy diagrams for PSI in a) bare gold electrodes, b)2-mercaptoethanol surfaces and c) 8mercaptooctanoic acid surface. Green arrows show the conditions in which we found LRET.

In view of the redox potential of P700*- A_0-A_1-F_X-F_B-F_A, probably these states are not accessible to the range of electrode potentials that we are applying. Thus, the charge transfer observed in our ECSTM and ECTS experiments is probably not occurring trough the biological ET pathway. In the absence of illumination, the redox state of the P700 center can be manipulated electrochemically, but the P700 cannot get the excitation energy necessary to transfer electrons through the ET chain. Thus, we are most likely using low energy electronic states ("hole" pathways) that have unknown biological relevance.

The ability to exchange electrons between probe and sample through PSI depends strongly on the functionalization of the gold surface. Regarding the low β~4 nm^{-1} peak, we have two different situations depending on the substrate functionalization. In the cases with bare gold and 2-ME substrates, the presence of the β~4nm^{-1} peak did not depend on the applied sample potential or the bias voltage, suggesting that this low β curves are result of a charge transfer mechanism that does not involve the redox states of the molecule. In the other two systems, with the 8-MOA and the 6-AH SAMs, the β~4 nm^{-1} peak disappears at high U_S potentials. This suggest that, in this case, the pathway could be redox mediated. We should take into account that different functionalizations can lead to different orientations of the molecule on the SAM[185], thus we are probably addressing different alternative pathways.

The LRET β~1 nm^{-1} peak indicates a significant change in the charge transfer route or pathway through the protein. This peak appears in all the systems but the 6-AH functionalized electrodes, probably due to a less efficient adsorption of the protein. Looking at the potential conditions (U_P, U_S) in which β~1 nm^{-1} is observed between probe and sample (LRET, Fig 6.9), it is noticed that it appears when U_S is close to the redox potentials of P700 and PC (200-400 mV), which suggest that the P700 center might be involved in the charge transfer mechanism. In Au-PSI and 2ME, LRET depends with bias, what implies a directionality of the charge transfer mechanism. As we see in the energy diagram of Au-PSI, effective injection of low energy electrons into PSI (hole extraction) allow LRET from the probe. 2ME surfaces show efficient extraction of low energy electrons of PSI (hole injection) and LRET from the probe. This fact suggests opposite orientations of the protein over the substrate. Finally, in the 8MOA, both hole injection and extraction lead to efficient LRET with a high occurrence of β~1 nm^{-1} at U_S=200 mV and both bias, which could be due either to a mix of orientations, or to a parallel orientation of the protein on the substrate[185].

Since hole transfer from PSI to the gold substrate is especially efficient in Au-PSI, 2ME and 8MOA (Figure 6.11), we propose that hole extraction from PSI is a key factor for efficient overall ET in PSI-coated gold surfaces. Enhancing the hole-exchanging capacity of the substrate while keeping a good orientation of PSI should allow increasing even further the ET efficacy of the substrate.

6.3.2 IZ curves: Light experiments.

We carried out preliminarily studies of the effect of illumination on current-distance measurements for PSI bound to 2ME functionalized electrodes. We performed curves in the dark and under illumination applying a sample potential of U_S=200 mV (Figure 6.10), with both positive (+300 mV) and negative (-300 mV) bias.

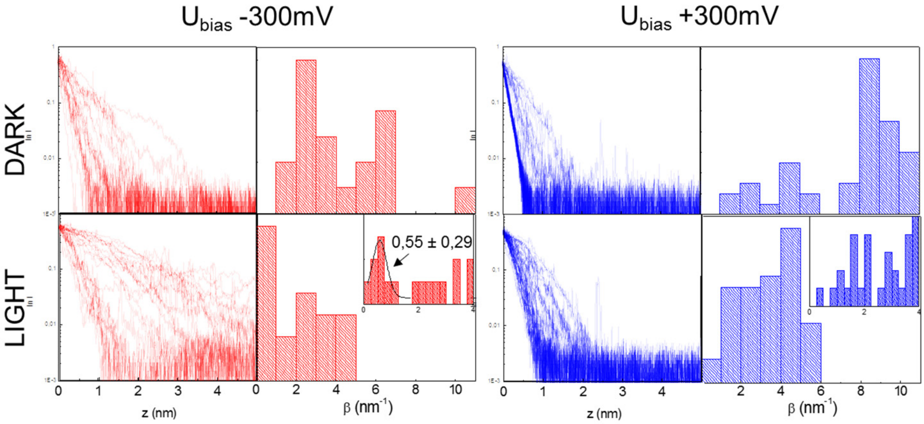

Figure 6.10. a, c) IZ curves for PSI onto 2-mercaptoethanol functionalized gold electrodes (raw data) obtained for U_S=200 mV and positive (+300 mV, blue) and negative (-300 mV, red) bias, performed in the dark (upper panel) and under red light conditions (bottom panel). b,d) statistical representation of the obtained β values for the curves in a,c. current setpoint was always 0.5 nA.

We found that both positive and negative bias curves showed lower β values upon illumination. Comparing with dark conditions, we can see that the high β values population seen in dark conditions disappeared under illumination, for both positive and negative bias potentials. However, we see a bigger effect in the case for negative bias in which β values as low as ~0.5 nm^{-1} have been obtained (inset Figure 6.10).

In both cases, the current-distance decay factor β was lower under illumination. Further results, including the differences between positive and negative bias and the interpretation of these photoeffects, will require additional experiments in a new ECSTM setup with improved illumination.

6.4 Conclusions

In this chapter, we performed current-distance spectroscopic measurements of all the PSI adsorbed onto four different substrates: bare gold electrode, 2-mercaptoethanol, 6-aminohexanethiol, and 8-mercaptooctanoic acid functionalized gold electrodes. We obtained the current decay factor β for all these systems, and evaluated its dependence with the applied sample potential and the bias potential.

The most stable β values were obtained with PSI in a bare gold electrode, and lowest β were achieved with PSI on the 2ME surface (with positive bias and U_S =400 mV) and on the 8MOA (with positive bias and U_S =200 mV and 400 mV).

We obtained low β values (4 nm^{-1}) in agreement with the ones reported for ET proteins[105] in all the systems. We also obtained LRET notably low β values (~1 nm^{-1}) in some of the systems, under determined conditions. Since we are working in the dark, and we are not addressing the molecular levels of the biological ET chain, these results suggest that we are most likely addressing low energy (holes) pathways alternative to the biological ET pathway.

LRET only appeared when U_S was 200-400 mV, a potential range of biological relevance for P700, close to its own and plastocyanin redox midpoint potentials. In bare-Au electrodes, PSI showed efficient long range hole extraction, while in 2ME electrodes, the most favorable process was hole injection. These results suggest that the P700 centre is involved in the injection and extraction of holes through the molecule, and that this mechanism has a preferred directionality. In 8MOA electrodes, PSI showed efficient LRET for both positive and negative bias, what suggest a mixture of orientations, or a parallel orientation over the electrode surface.

Preliminary current distance experiments under illumination yielded a reduced current decay factor β.

7

Conclusions

General conclusions

In this thesis we investigated ET proteins using Scanning Probe Microscopies under electrochemical control. Cases of study were two very different ET biosystems: the metalloprotein and the photosynthetic complex Photosystem I (PSI).

ECTS measurements of Azurin showed a current rectifying behavior of Azurin under electrochemical control. From the obtained current-voltage data, we obtained the transition voltage (TV) value of Azurin in the tunneling configuration as well as wired to the metal electrodes. TV marks the transition between two conductance regimes that are in agreement with the biological activity of azurin: to exchange and transport charges. The lower value of TV obtained for the wired configuration in comparison to the tunneling configuration, reflects the stronger coupling of azurin with the probe, which lowers the energy barrier between them. These results suggest that biological ET could be modulated by the electronic coupling between redox partners.

We developed a method to improve the resolution of current measurements in ECTS. This new method allowed us to obtain differential conductance images of a surface under electrochemical control. The technique was validated by characterizing the reversible oxidation of an iron electrode, whose conductance and topography were monitored simultaneously in different redox states. The conductance changes between reduced and oxidized iron measured with this technique were in agreement with previously published results. Differential conductance imaging was used to characterize azurin and revealed a submolecular high conductance spot, indicating the existence of an ET pathway towards a localized, high electronic coupling site.

We studied the force-conductance relationship of azurin deposited on gold in an electrochemically-controlled environment. Both force controlled current voltage spectroscopy and force and current distance spectroscopies, showed that the conductance on the Au-Azurin-Au junction increased with the applied force over the junction. The conductance-force dependence changed with the redox state of the protein: the required force for current flowing through the Au-Azurin-Au is higher when the protein is reduced. The increase of conductance upon an increase on applied force could be due to a number of factors: An increase in the contact area, a reduced distance between the probe and the Au substrate, changes on the structure or changes on the ET mechanism. All these factors can contribute to the increased conductance through the junction, but the difference between the redox states can only be explained through a change in the ET mechanism, since there is no evidence of structural changes between redox states in azurin.

PSI was successfully bound to Au electrodes through different surface treatments, yet it adsorbed to different extents. The systems that showed highest coverage and more homogeneous adsorption were the 2-mercaptoethanol and the 8-mercaptooctanoic acid functionalized electrodes. PSI retained its electrochemical activity, and produced photocurrent generation upon illumination on both surfaces. PSI also adsorbed onto bare-gold electrodes and 6-aminohexanethiol functionalized gold electrodes, but with a lower surface coverage and a heterogeneous adsorption, creating islands and aggregates of the protein and/or the surfactant over the surface. All four treatments were suitable for ECSTM imaging, and three of them stood a relatively wide range of sample potentials. The apparent height of the PSI molecules was in agreement with reported values in the literature. The apparent height of PSI was independent of the applied bias, but it changed with the applied sample potential (U_S). Imaging at potentials above the redox peak of p700 of PSI (U_S>400 mV), the average apparent height of the protein spots increased about a 10% (~0.5 Å), suggesting that the ET transfer mechanism has redox dependent steps.

Current-distance spectroscopic measurements showed that PSI presents low distance decay β values of β~4nm^{-1}, in agreement with the ones reported for ET proteins in other systems. We also obtained anomalously low β values of β~1nm^{-1} in some of the systems, under certain conditions of potential and surface treatment. Since measurements are performed in dark conditions, and the applied potentials do not attain the high-energy states of the biological ET chain, these results suggest that in this case ET involves low energy (holes) pathways of unknown biological relevance. Long range charge transfer (β~1 nm^{-1}) was only observed at sample potentials close to the redox potential of the P700 center, which suggests that it mediates the long range injection and extraction of holes through the complex.

Resumen en castellano

1. Introducción.

La transferencia de electrones (ET) es un proceso fundamental en biología[1]. Es crucial para procesos biológicos esenciales, especialmente los relacionados con la conversión de energía, como la fotosíntesis o la respiración celular. La transferencia de electrones tiene lugar intra- e inter-proteínas, entre centros metálicos u otros cofactores que están separados por largas distancias. Se han dedicado muchos esfuerzos experimentales y teóricos para comprender el proceso de ET en biología, no sólo por el interés fundamental del campo, sino también por las potenciales aplicaciones tecnológicas de estas proteínas como componentes de dispositivos electrónicos biomoleculares[2].

Transferencia de electrones en biología: proteínas redox.

Los procesos de transferencia de energía en biología, tienen lugar principalmente entre centros de proteínas redox. Las principales familias de proteínas redox involucradas estos procesos son: citocromos, clusters de hierro-azufre y cupredoxinas. Combinadas, estas proteínas redox cubren toda la gama de potenciales de reducción relevantes en biología[3]. Los centros redox de las diferentes familias tienen diferentes geometrías, pero todos satisfacen los requisitos para una ET[1] eficiente: 1) hay un cambio mínimo en la geometría entre estados redox, lo que minimiza la energía de reorganización asociada al proceso de ET, y 2) presentan un acoplamiento electrónico eficiente entre donante y aceptor de cargas a largas distancias a través de la proteína[4].

Los citocromos son una familia de proteínas ET que contienen un grupo heme. Están presentes principalmente en la membrana mitocondrial interna de organismos eucariotas y en una amplia variedad de bacterias Gram-positivas y Gram-negativas[3].

Las proteínas Fe-S se encuentran en todas las formas de vida y desempeñan papeles en procesos cruciales como la fotosíntesis y la respiración. Estas proteínas muestran una amplia gama de potenciales redox y diferentes motivos estructurales que les permiten interactuar con diferentes parejas redox, participando en numerosos procesos biológicos[6, 7].

En las proteínas Fe-S podemos distinguir tres grupos principales: Rubredoxinas, Ferredoxinas, y HiPIPs (Proteinas de hierro-azufre de alto potencial), además de complejos proteicos con centros de Fe-S presentes en hidrogenasas y otras enzimas, y en la cadena del complejo respiratorio, de la cual hablaremos en una sección posterior.

Las proteínas de cobre que actúan como mediadores de ET incluyen proteínas de cobre azul (o tipo 1) y centros dinucleares Cu_A. En las cupredoxinas, la estructura de la proteína desempeña un papel significativo en mantener la geometría del centro redox. En ambos tipos de cupredoxinas, el Cu presenta una geometría trigonal y un fuerte enlace cobre-tiolato. Las proteínas dinucleares Cu_A incluyen la citocromo c oxidasa y otras enzimas, que son receptores de electrones terminales de diferentes procesos ET. Las proteínas de cobre azul incluyen proteínas implicadas en procesos ET como Plastocyaninas, Azurinas y enzimas multicobre[10]. Las proteínas de cobre azul se encuentran en arqueas, bacterias y plantas, donde actúan como portadores de electrones en la ET biológica.

Complejos respiratorios

El sistema respiratorio mitocondrial es el principal productor de energía en células eucariotas[3]. Está compuesto por cinco complejos multi-polipéptidos[15] y por ubiquinona y citocromo c como portadores de electrones móviles. Los electrones entran en la cadena respiratoria en el complejo I (NADH-UQ oxidorreductasa) y el complejo II (succinato deshidrogenasa), donde el NADH y el succinato actúan como donadores de electrones para reducir la ubiquinona al ubiquinol. El ubiquinol transfiere electrones a través del complejo III (complejo Cytochrome bc_1) a citocromo *c*. El citocromo c se oxida en el complejo IV (complejo de citocromo c oxidasa) y transfiere electrones a O_2 para producir agua. Este proceso se acopla al bombeo de protones a través de la membrana, lo que genera un gradiente de protones que es utilizado por el complejo V (ATP sintasa) para generar ATP.

Proteínas fotosintéticas.

En la fotosíntesis oxigénica, tres complejos proteicos se organizan en la membrana tilacoide del cloroplasto, y plastocianina (PC) y quinona actúan como portadores de electrones. En la cadena fotosintética, el Fotosistema II (PSII) oxida el agua para producir oxígeno y reduce las quinonas. Las quinonas reducidas son entonces utilizadas por el citocromo b_6f para crear un grandiente de protones a través de la membrana y para reducir la plastocianina, que es el donante de electrones del Fotosistema I (PSI). Un fotón adicional se absorbe por cualquiera de los pigmentos del PSI y se transfiere al par de clorofilas P700, oxidándolo. El electrón extraído de P700 se mueve a través de una cadena interna y reduce la ferredoxina (Fd), que es el aceptor final de electrones del PSI. El P700 es re-reducido por la PC. La Fd reducida está implicada en varias vías celulares, principalmente la reducción de NADP a NADPH, que junto con ATP impulsan el ciclo de Calvin para producir carbohidratos[29]. La enzyma ATP sintetasa utiliza el potencial de membrana para sintetizar ATP. Estos complejos de proteínas están presentes en todas los organismos que realizan fotosíntesis oxigenada, cianobacterias, algas y plantas.

El fotosistema I (PSI)

El PSI de las plantas superiores se compone principalmente de dos partes: el centro de reacción y el complejo de recolección de luz I (LHCI) que rodea el centro de reacción y maximiza la absorción de luz y transmite la energía al centro de reacción. El centro de reacción está compuesto por 19 subunidades. El heterodímero PsaA-PsaB forma el corazón del centro de reacción. Contiene el par especial de clorofilas P700, donde comienza la separación de carga impulsada por la luz, y los primeros aceptores de electrones A_0 (clorofila-a), A_1 (filoquinona) y F_x (cluster Fe_4-S_4). Los receptores de electrones terminales de la cadena, F_A y F_B, dos grupos de Fe_4-S_4, están unidos a la subunidad PsaC. El resto de subunidades están involucradas en el acoplamiento de ferredoxina, plastocianina, y la asociación con LHCI[30].

Teoría de transferencia de electrones

La teoría de Marcus describe la constante de ET entre un donante de electrones (A) y un aceptor (B) a una distancia fija, en términos de la fuerza motriz para la reacción ET ($-\Delta Go$), la energía de reorganización requerida (λ), y el acoplamiento electrónico (H_{AB}) entre A y B en el estado de transición:

$$\boldsymbol{k_{ET} = \sqrt{\frac{4\pi^3}{h^2 \lambda k_B T}} H_{AB}^2 exp\left(-\frac{(\Delta G^o + \lambda)^2}{4\lambda k_B T}\right)} \qquad \text{eq. 1}$$

Donde k_B y h representan las constantes de Boltzmann y Planck, respectivamente, y T la temperatura. Cuando la fuerza motriz es igual a la energía de reorganización, la constante de ET tiene una dependencia exponencial con d_{AB} (Eq. 2). El parámetro clave en esta relación es el factor de decaimiento β, característica del mecanismo de ET, y del medio entre donante y aceptor.

$$k_{ET} \propto exp(-\beta d_{AB}) \qquad \text{eq. 2}$$

En biología, las cargas necesitan recorrer distancias más largas que las que podrían lograrse mediante un proceso de túnel de un solo paso. La solución para la ET de largo alcance es disponer cofactores espaciados entre sí a una distancia túnel actuando como intermediarios del ET[25, 78]. Se han propuesto varios modelos teóricos para describir la ET de largo alcance en cadenas biológicas incluyendo: Superexchange, Hopping, y Flickering Resonance[82].

En el modelo superexchange para ET, el túnel de electrones está mediado entre el aceptor y el donante por estados intermedios, que no se ocupan durante el proceso. En el modelo de flickering resonance, el medio actúa como una cadena de estados redox que pueden aceptar y donar electrones o huecos. En el modelo de hopping, la transferencia de carga entre donante y aceptor se produce a través de saltos consecutivos de un sitio a otro, con probabilidad de saltar hacia delante y hacia atrás. Este mecanismo puede explicar distancias ET más largas, ya que muestra una dependencia débil de la distancia[84].

Las Proteínas como dispositivos electrónicos

Las propiedades especiales de las proteínas de ET las convierten en candidatos prometedores para una amplia variedad de aplicaciones tecnológicas[96], incluidas las aplicaciones energéticas[97, 98] biomédicas[99-101] y ambientales[102].

La metaloproteína Azurina como sistema modelo para estudiar ET

La Azurina de Pseudomonas aeruginosa (Az) tiene un centro de cobre y presenta un puente disulfuro entre Cys 3 y Cys 26[14], que puede usarse para inmovilizar covalentemente la proteína sobre un electrodo de Au[12, 103-106]. La metaloproteína Azurina representa un punto de referencia para el estudio de ET en proteínas. La azurina presenta propiedades de transporte eficientes a lo largo de ~ 3.5nm, una distancia demasiado larga para el túnel de electrones a través de moléculas orgánicas saturadas[84]. Esta vía de ET de largo alcance se cree que está asistida por aminoácidos oxidables como el triptófano y la tirosina a lo largo de la estructura de la proteína[108]. El potencial tecnológico de la Azurina ya está siendo estudiado en diferentes aplicaciones, como biomemoria[135], y otros dispositivos electrónicos[106, 137].

El Fotosistema I como un potencial dispositivo bioelectrónico.

El PSI actúa como un fotodiodo natural, que induce transferencia de electrones tras radiación luminica. La eficiencia de transferencia de energía de PSI en este proceso es cercana a la unidad[138]. Esta eficiencia y la accesibilidad superficial a los aceptores y donadores de electrones de la cadena de ET puede ser explotada en el estudio de ET de PSI y en el empleo de PSI para aplicaciones tecnológicas. Estas características hacen de PSI uno de los sistemas de ET más investigados en biología, tanto por su importancia como por sus prometedoras aplicaciones en electrónica biomolecular.

Ventajas de las SPM para la ET en biología

Las Microscopías de Sonda Próxima (SPM) permiten la medida de una pequeña cantidad de proteína, o incluso de moléculas individuales, en vacío, aire, atmósfera inerte o medio líquido. La posibilidad de trabajar en medios acuosos abre la puerta al estudio de sistemas biológicos en condiciones casi fisiológicas. STM en líquido admite la posibilidad de trabajar bajo control electroquímico de ambos electrodos (muestra y sonda). Esta configuración permite un control electroquímico completo del sistema, ofreciendo al mismo tiempo resolución a nivel de molécula individual[12, 71, 105, 169].

Uno de los puntos fuertes tanto de ECSTM como de AFM es el hecho de que además de imágenes de alta resolución, pueden realizar diferentes tipos de espectroscopias, pudiendo sondear de esta manera diferentes propiedades de la muestra, relacionadas con su comportamiento electrónico y propiedades estructurales y mecánicas.

ECSTM y cAFM aplicado al estudio de proteinas de ET.

ECSTM se ha aplicado al estudio de proteínas de ET tales como azurina[71, 104-106, 112, 137, 169, 171], citocromo[172-174], y enzimas redox[175, 176]. ECSTM ha demostrado que el proceso ET en azurina implica su ion Cu[71, 171]. La Azurina también se ha estudiado utilizando AFM conductor[178], que muestra que la conductancia de azurina depende de la fuerza aplicada sobre ella. El cAFM también se ha aplicado al estudio de proteínas de ET como plastocianina[179]o fotosistema I[141, 182, 183], en ambientes no conductores. El PSI también se ha caracterizado por STM y STS[184, 185], lo que demostró su comportamiento de tipo diodo, y su dependencia con respecto a la orientación de la molécula en la superficie. Sin embargo, su mecanismo ET no se ha caracterizado en un ambiente totalmente electroquímicamene controlado, como el que ECSTM ofrece.

Retos actuales

ECSTM y ECTS han arrojado luz sobre ciertos aspectos del mecanismo de ET en proteínas de ET, pero todavía hay desafíos experimentales por delante, como mejorar la resolución espacial de ECTS. Un método fiable y rápido que podría caracterizar la conductancia de moléculas individuales con alta resolución espacial sería muy útil para caracterizar las proteínas ET multiredox o cadenas largas de transferencia de electrones. Otro desafío técnico importante sería el desarrollo para la aplicación de cAFM en ambientes líquidos. Esta técnica permitiría estudiar la relación entre la estructura de las proteínas redox y el comportamiento electrónico bajo control electroquímico completo, pero es técnicamente difícil.

Objetivos

El objetivo general de esta tesis es describir los mecanismos de transferencia de electrones de las proteínas ET al nivel de una molécula individual. Para abordar este objetivo, la Microscopía de Túnel Electroquímica (ECSTM) y la Microscopía de Fuerza Atómica conductora (cAFM) son técnicas ideales, ya que permiten trabajar a nivel de una sola molécula, en diferentes modos de operación.

Nuestro objetivo es explorar el comportamiento de la conductancia de la proteína Azurina con respecto a su estado redox y otros parámetros, como el modo de contacto entre azurina y los electrodos, o la fuerza mecánica aplicada con este contacto. Este objetivo incluye evaluar los requisitos técnicos necesarios para mejorar la resolución espacial y la recopilación de datos de las medidas ECTS, adaptando el método de corriente alterna normalmente utilizado en UHV-STS al STM electroquímico. Este primer objetivo principal también implica desarrollar una metodología en la que sea posible combinar las medidas de fuerza que el AFM ofrece, con medidas eléctricas, en un entorno controlado electroquímicamente. El desarrollo de esta metodología incluirá el diseño y la fabricación de nuevas puntas de AFM. Esta mejora técnica permitirá describir el proceso de ET con un gran nivel de detalle.

Además de la caracterización de Azurina, pretendemos caracterizar el mecanismo ET de una proteína ET más compleja, el Fotosistema I. Comenzaremos por caracterizar la proteína con imágenes y espectroscopia de ECSTM y evaluaremos sus propiedades de conductancia en un amplio rango de potenciales electroquímicos. Para lograr este objetivo, primero tenemos que desarrollar una estrategia de inmovilización para el Fotosistema I adecuada para ECSTM. Este primer paso permitirá la aplicación posterior de todos los modos de ECSTM y ECTS para estudiar este sistema.

2. ECSTM y ECTS de la proteína azurina

Características de corriente-potencial.

La dependencia de la conductancia de una única azurina en potenciales electroquímicos se estudió con ECTS de corriente-potencial (I-V). Las medidas se llevaron a cabo en la configuración de túnel, donde no hay contacto físico entre la punta de STM y la proteína, y en configuración "cableada", donde la azurina está en contacto directo con la proteína. En las I-Vs se ven dos tipos de curvas: una población con rectificación de corriente y otra población con un comportamiento lineal (Figura 8.1). En ausencia de moléculas de Azurina, todas las curvas mostraron un comportamiento lineal, por lo que atribuimos las curvas rectificadoras de corriente a la proteína Azurina.

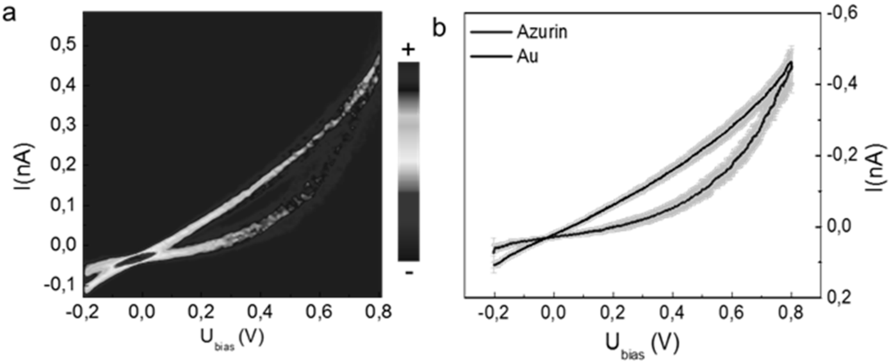

Figura 8.1 A) Histograma 2D mostrando las curvas IV obtenidas en una muestra de azurina sobre Au. US = -0,3 V (azurina reducida); UP inicial = 0,5 V; Corriente al iniciar las curvas I = 0,5 nA; N = 50. (b) Promedio de las dos poblaciones I-V identificadas en (a), correspondientes a azurina (azul) y Au (negro). Las barras de error gris indican desviaciones estándar

Calculamos el valor de potencial de transición (TV) para la conductancia de azurina de las curvas IV. Los espectros de potencial de transición de Azurin (TVS) mostraron valores mínimos distribuidos alrededor de 0.4V. También se examinó el espectro de TVS de azurina en una configuración cableada, donde se encontró un mínimo en la rama negativa que correspondía a un TV muy bajo (-0,06 ± 0,01 V). El valor de TV inferior refleja el acoplamiento más fuerte con el electrodo de punta, que baja la barrera de energía entre los niveles del electrodo de punt STM y la molécula. TV marca la transición entre dos regímenes de conductancia que están de acuerdo con la actividad biológica de la azurina: intercambio y transporte. Estos resultados sugieren que el ET biológico podría ser modulado por el acoplamiento electrónico entre las parejas redox, un concepto que ha sido estudiado usando enfoques electroquímicos[201].

3. Imagen de conductancia diferencial con ECTSM

Adaptamos el modo de espectroscopia corriente-potencial de ECSTM para incluir una modulación de potencial sinusoidal a la punta y medimos la amplitud de la modulación provocada en la corriente por medio de un amplificador lock-in. Esta señal es proporcional a la conductancia diferencial dI / dV de la superficie estudiada. Podemos utilizar esta señal para construir una imagen de conductancia diferencial mientras escaneamos la superficie, obteniendo simultáneamente una imagen de conductancia diferencial y la topográfica tradicional. Primero validamos este método estudiando la oxidación reversible y pasivación de un electrodo de hierro en tampón de borato, un sistema ampliamente estudiado cuya conductancia local se había caracterizado previamente con ECTS[170, 208], obteniendo resultados en acuerdo con los previamente publicados.

Imagen DECC de Azurina en superficies de oro.

En las imágenes DECC de proteínas Azurina individuales, la imagen de las proteínas individuales reveló características de conductancia sub-molecular. La Figura 8.2 muestra imágenes topográficas y DECC de alta resolución de una sola proteína Az. Se puede observar un punto de conductancia diferencial brillante y alto cerca del centro de la proteína, rodeado por una región de menor conductancia. El punto de alta conductancia aparece en la misma posición en ambas direcciones de escaneo (Figura 8.2a y Figura 8.2b). La mayor conductancia diferencial de Az con respecto al sustrato de oro puede ser debido a las características no lineales I-U de la proteína[192].

Simulaciones de Az en una superficie de oro (111)[213] concluyeron que la orientación preferida de la proteína sobre la superficie es casi tumbada. Se espera que la molécula, unida covalentemente a través de dos cisteínas superficiales (de color verde en la Figura 8.2c) se “tumbe” con su parche hidrófobo (azul en la Figura 8.2c) orientado hacia arriba. Este parche hidrofóbico rodea al centro de Cu, que juega un papel importante en la transferencia de electrones[169, 214, 215]. En esta configuración, el centro de Cu estaría frente a la punta, favoreciendo así la transferencia de electrones entre ellos. Estos resultados apoyan la idea de que la ET a través de Az está mediada por su átomo de cobre. En el contexto de la ET biológica entre las proteínas redox y sus parejas, las regiones de proteína con alta conductancia pueden asociarse a sitios específicos de altoacoplamiento electrónico, requeridos para el intercambio electrónico eficiente[192].

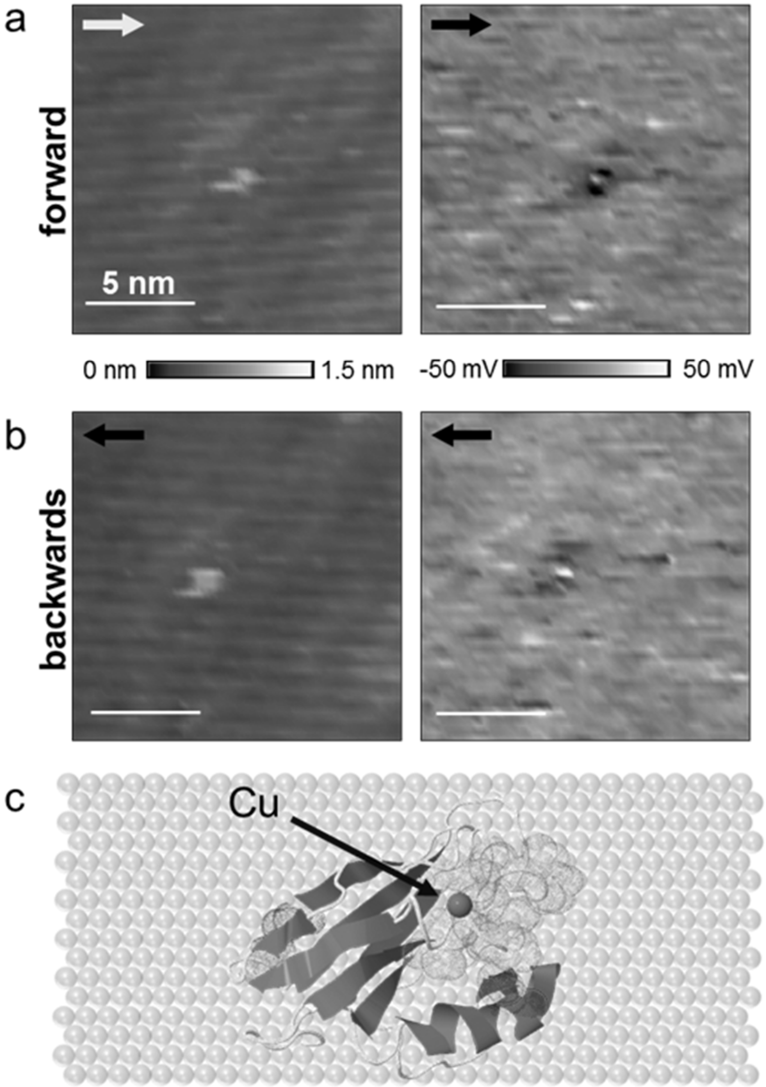

Figura 8.2. Imagenes simultaneas de alta resolucion topográficas(izq) y de conductancia diferencial(dcha). Escala, 5nm. Aparece una azurina individual, que muestra un area sub molecular con alta conductancia diferencial, rodeada de una zona de baja conductancia. (c) Representacion de la proteina azurina (PDB: 1AZU) sobre un electrodo de oro, de acuerdo con un modelo publicado [213].

4. AFM conductor en medio electroquímico

En este capítulo, pretendemos desarrollar un protocolo para la obtención de puntas de cAFM capaces de trabajar en medios electroquímicos. Para eso hemos seguido dos enfoques: en primer lugar, cubrir puntas comerciales con una capa de Alumina y, en segundo lugar, adaptamos la técnica de revestimiento del Prof. Demaille a puntas comerciales.

Paralelamente, gracias a una colaboración con el grupo del Prof. Demaille, utilizamos las puntas caseras AFM-SECM desarrolladas en este grupo, para estudiar superficies de oro recubiertas con Azurina en un medio controlado electroquímicamente.

Aislamiento de puntas de cAFM

Seguimos dos estrategias para aislar eléctricamente las puntas conductoras comerciales de AFM: recubriendo puntas comerciales con una capa de Al_2O_3 con Atomic Layer Deposition (ALD) o recubriendo las puntas con una capa de pintura de deposición electroforética. Con el recubrimiento de ALD obtuvimos algunas puntas de fugas bajas, pero con poca reproducibilidad. Con el recubrimiento EDP mediante la aplicación de un potencial DC continuo optimizamos las condiciones para obtener alrededor del 30% de las puntas con fugas de corriente por debajo de 50 pA, pero parte del cantilever mostró algunas alteraciones en sus propiedades. Con el recubrimiento EDP mediante la aplicación de una rampa de potencial, obtuvimos curvas de fugas reproducibles y con una capa de capa delgada que no comprometió la forma del cantilever o la reflectividad del laser.

Fuerza y espectroscopía de corriente de la unión Au-Au en medios electrolíticos

Las puntas recubiertas con EDP con el método del potencial de rampa se usaron para realizar curvas de espectroscopia de fuerza en cAFM en medio electroquímico. Antes de las medidas, las puntas se calibraron utilizando el método de ruido térmico. Las puntas calibradas muestran una constante de flexibilidad entre 2 y 3 veces superior a la constante nominal.

Obtuvimos curvas de ruptura de uniones (break-junctions) Au-Au. En el proceso de retracción de la punta del sustrato, obtuvimos trazas de corriente en las que la corriente está saturada mientras los dos electrodos están en contacto, y disminuye bruscamente cuando se rompe el contacto. En esta traza de corriente, vemos un escalón que indica que una pequeña unión se crea y se rompe durante la retracción de la punta. Recogiendo las trazas de corriente de retracción, podemos construir histogramas de conductancia (Figura 8.3). Se obtuvo un valor de conductancia 0,67 ± 0,02 Go de los escalones, en el rango de la conductancia correspondiente de una unión Au-Au. El mismo experimento, realizado con puntas de AFM conductoras comerciales sin tratamiento adicional (es decir, sin aislar) en aire dio como resultado un valor en concordancia de 0,66 ± 0,02Go (Figura 8.3b, gris).

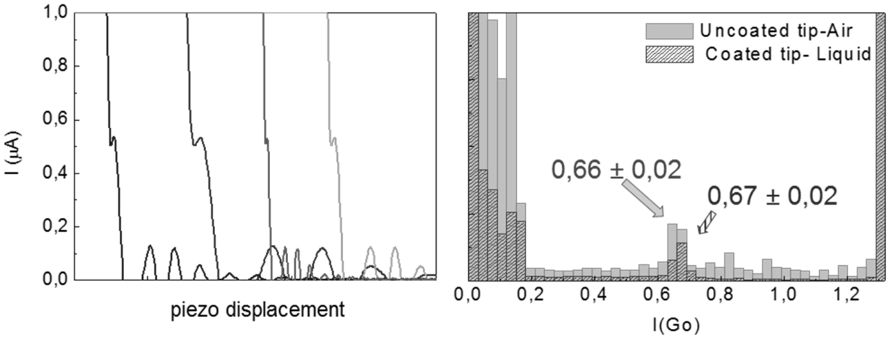

Figure 8.3. a) Curvas de corriente obtenidas durante el retroceso de la punta (aumentando la distancia punta-muestra), obtenidas con puntas de AFM aisladas en solución con un bias de -10 mV. El eje x representa el desplazamiento piezoeléctrico, a las trazas se les ha aplicado un desplazamiento para separarlas para mayor claridad. b) histogramas de trazas de corriente de retracción sobre un electrodo de oro. El histograma gris corresponde a las trazas de corriente obtenidas en el aire con una punta cAFM comercial sin aislamiento. El histograma rojo corresponde a las curvas obtenidas con una punta aislada en líquido, a la misma velocidad y con el mismo bias.

Medidas electroquímicas de cAFM de la proteína Azurina.

Paralelamente a estos experimentos, colaboramos con el grupo del Prof. Demaille en la Université de Paris 7 - Paris Diderot.

Espectroscopía corriente-potencial bajo fuerza controlada.

Las curvas de Azurina I-V mostraron una clara dependencia con la fuerza aplicada a los tres potenciales de muestra medidos. A fuerzas bajas, las curvas I-V aparecen casi como una línea plana, con una pendiente cercana a 0 nA / V. A medida que aumentamos la fuerza aplicada, vemos el aumento de la pendiente. Se ha publicado que la azurina requiere una fuerza de carga mínima para dar señal de corriente[128, 178, 221]. El aumento de la conducción con la fuerza de carga aplicada podría ser debido a varios factores. En primer lugar, un aumento en la fuerza de carga puede implicar un aumento en el área de contacto de la punta, dando lugar a que un mayor número de proteínas Azurina estén en contacto con la punta. Una mayor fuerza también implica una disminución de la distancia entre la punta y el sustrato, lo que puede contribuir al aumento de la corriente. Además, la fuerza puede estar distorsionando la estructura secundaria de la proteína, lo que puede provocar a cambios en las propiedades electrónicas de la proteína[128]. Todos estos factores pueden contribuir al aumento del flujo de corriente a través de la unión con una fuerza de carga creciente. Curiosamente, la conductancia de la proteína no aumenta a la misma velocidad con la fuerza aplicada en diferentes estados redox. Cuando aumentamos la fuerza, vemos que, cuando la proteína está reducida, la curva IV sigue siendo plana, pero para la misma fuerza aplicada, en el punto medio redox, la conductancia de la unión aumenta y es aún mayor cuando la proteína se oxida. Por lo tanto, la unión Au-Azurina-Au requiere fuerzas menores para conducir a través de la unión cuando la proteína está oxidada.

La menor fuerza mínima requerida para lograr una buena conducción cuando la proteína se oxida con respecto a los otros estados, podría significar que la proteína es más sensible a los cambios de fuerza cuando se oxida y, por tanto, más flexible que en su forma reducida. Sin embargo, no hay evidencia que sugiera un cambio en la estructura de la proteína con su estado redox. Por lo tanto, este efecto es más probablemente debido a un ET más eficiente a través de la proteína cuando se oxida, lo que sugiere un mecanismo de conducción que implica huecos.

Espectroscopía de fuerza y corriente con la distancia

Realizamos simultáneamente medidas de fuerza y distancia de corriente-distancia sobre el sistema Azurina-Au. En la primera etapa de las curvas, cuando la punta se aproxima a la muestra, vemos que, para las tres condiciones, la corriente aumenta mientras aumenta la fuerza aplicada. Sin embargo, en el caso de la proteína reducida, la fuerza mínima necesaria para detectar la corriente a través de la proteína es mucho mayor que en los otros casos. Durante la retracción de la punta, se obtuvieron trazas de corriente con escalones que señalan la presencia de uniones. La conductancia de los escalones está modulada con el potencial electroquímico, de acuerdo con los resultados anteriores realizados con ECSTM[106] (Figura 8.4).

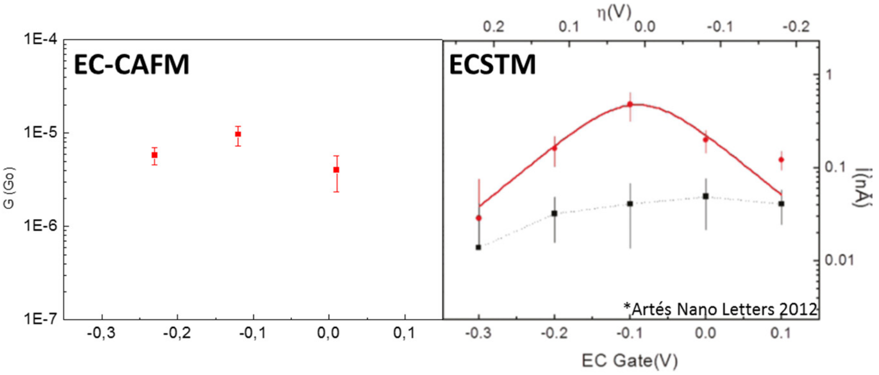

Figura 8.4. Comparación entre los resultados de modulación de la conductancia de Azurina sobre Au, obtenidos con cAFM electroquímico (izquierda) y ECSTM (derecha). Datos de ECSTM de ref[106] (Artés et al. NanoLett 2012).

5. Caracterización de PSI: imagen con SPM y electroquímica.

Para investigar las propiedades de PSI con ECSTM, necesitamos inmovilizar la proteína en un electrodo conductor. En nuestro caso utilizamos estrategias de inmovilización simples: adsorción de PSI sobre un sustrato de oro, y adsorción de PSI sobre sustratos de oro funcionalizado con monocapas auto-ensambladas (SAM) de alcanotioles, con tres grupos terminales diferentes: -OH, -NH2, -COOH, que producen superficies neutras, positivas y cargadas negativamente respectivamente.

Adsorción de Fotosistema I en las diferentes superficies.

Todos los sistemas utilizados para la inmovilización de PSI se basaron en interacciones físicas, inespecíficas en el sentido de que no hay un punto de anclaje específico en la proteína. El PSI se adsorbió en todos los sistemas, pero la cantidad y distribución depende de las propiedades superficiales de los sustratos utilizados.

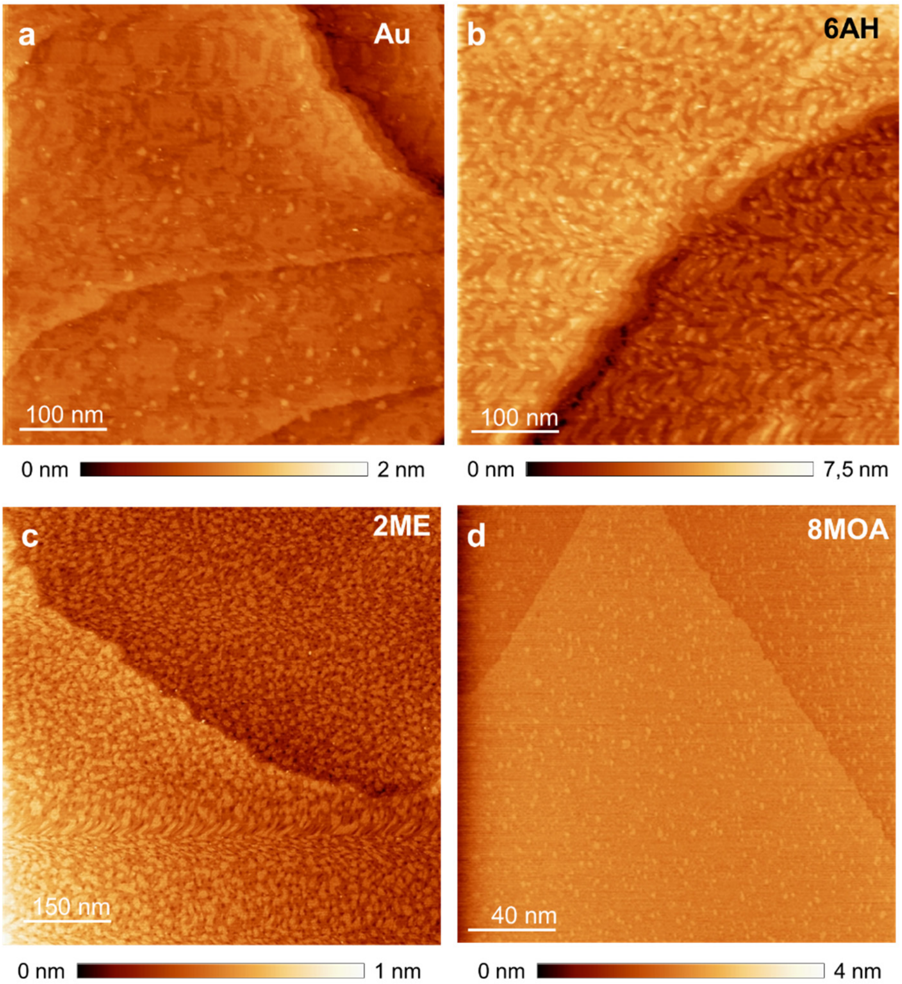

Figura 8.5. Imágenes de ECSTM del PSI sobre a) electrodos de oro, b) electrodos de oro funcionalizados con una SAM de 6-aminohexanotiol, c) electrodos de oro funcionalizados con una SAM de 2-mercaptoetanol, y d) electrodos de oro funcionalizados con una SAM de ácido 8-mercaptooctanoico. Todas las imágenes se tomaron con un potencial de muestra de U_S = 200mV, y un potencial de punta de U_P = -100 mV. La corriente se mantuvo en todo momento constante a I= 0.5nA. La escala se indica en cada imagen. La escala de color (escala en z) se indica debajo de cada una de las imágenes.

Las moléculas de PSI se adsorbieron en electrodos de oro, de manera bastante homogénea, apareciendo las proteínas rodeadas de islas de surfactante. Esto ocurrió también en la SAM de 6-aminohexanotiol SAM, pero no en el ácido 8-mercaptooctanoico o el 2-mercaptoetanol, donde la adsorción de PSI fue mayor. PSI sobre oro y 6-aminohexanetiol parecen tener también un comportamiento similar con respecto al potencial de la muestra, es decir, un aumento de la altura aparente en condiciones oxidantes. Es sabido que PSI adsorbe sobre electrodos de oro con orientaciones mixtas[244]. La interacción de PSI con 6-aminohexanetiol no es muy clara. La carga superficial de PSI y la ausencia de puntos de fijación específicos sugieren que la naturaleza de la interacción es muy probablemente electrostática y, en principio, podríamos esperar que la carga parcialmente positiva de la superficie atraiga a los residuos cargados negativamente de la proteína. Sin embargo, se ha publicado[259] que las SAMs terminadas en amino en presencia de fosfatos inorgánicos podrían adsorber moléculas de fosfato de la solución, creando una capa sobre la superficie de la SAM que sobrecompensaría la carga positiva parcial de la SAM. Esto podría dar lugar a una SAM con propiedades electrostáticas heterogéneas, que provoca a su vez orientaciones mixtas de la proteína, y menos adsorción debida a la neutralidad electrostática.

Es sabido que el PSI tiene una buena adsorción en SAMs terminadas en hidroxilo[185], mediante enlaces de hidrógeno, con el 70% del PSI orientado con su vector de ET perpendicular a la superficie, aunque existe cierta controversia en cuanto a si la cadena de ET está apuntando hacia arriba[185] o hacia abajo[141]. La aparición de las imágenes AFM y ECSTM indica que el PSI se adsorbe homogéneamente sobre la superficie de 2-mercaptoetanol, pero no permite aclarar la orientación de la molécula.

En las superficies funcionalizadas con ácido 8-mercaptooctanoico, las moléculas de PSI se adsorben de manera abundante y homogénea. La interacción es probablemente electrostática, con la superficie parcialmente cargada negativamente atrayendo los residuos positivos sobre la superficie de la proteína. Aunque las cargas positivas se distribuyen sobre toda la superficie de la proteína, una región candidata a la interacción con la superficie negativa de la SAM, sería el parche cargado positivamente en la parte lumenal de la proteína, que es el sitio de unión para la plastocianina [51].

6. Caracterización de PSI: Espectroscopía túnel

Curvas corriente-distancia.

Se estudió la dependencia de la corriente con la distancia (I-z) del PSI sobre los 4 sustratos estudiados en el capítulo 5. En todos los sistemas, la corriente decayó exponencialmente hasta alcanzar los valores faradáicos de corriente de la punta lejos de la muestra. Al ajustar la parte exponencial de las curvas, se obtuvo el factor de decaimiento de distancia β para todos los sistemas y se evaluó su dependencia con el potencial de muestra aplicado, con bias positivo y negativo. En la mayoría de los casos se obtuvieron valores β inferiores a los de las superficies metálicas, en correspondencia con los obtenidos para las proteínas ET[105]. Sin embargo, estos valores β variaron con las condiciones de potencial y de bias de diferentes maneras para cada sistema de inmovilización.

En los cuatro sistemas de inmovilización encontramos curvas con un factor de decaimiento de baja distancia de $\beta \sim 4\text{nm}^{-1}$, en el mismo rango de otras anteriormente obtenidas para proteínas ET[105]. En algunos casos encontramos, además de este pico, valores β anormalmente bajos de incluso $\beta \sim 1\text{nm}^{-1}$, los cuales nunca han sido reportados en ET inter-proteína. Estos valores pueden ser indicadores de un fuerte acoplamiento electrónico que permite una ET eficiente a largas distancias a través de la solución acuosa.

A pesar de la cobertura relativamente baja de PSI, el sistema más simple parece ser PSI en un electrodo de oro . Los valores β no dependen fuertemente de los cambios potenciales y una región a valores β muy bajos es claramente visible a U_S = 200 mV y bias negativo. La SAM de 6-aminohexanotiol da la distribución más borrosa de los valores β, lo que sugiere una baja adsorción, ya que los valores altos de β son predominantes.

En vista del potencial redox de P700 * -A0-A1 ... y Fd, probablemente estos estados no son accesibles a la gama de potenciales de electrodo que estamos aplicando. Por lo tanto, la transferencia de carga observada en nuestros experimentos ECSTM y ECTS probablemente no se producen a través de la vía de ET biológica. En ausencia de iluminación, el estado redox del centro P700 puede manipularse electroquímicamente, pero el P700 no puede obtener la energía de excitación necesaria para transferir electrones a través de la cadena ET. Por lo tanto, estamos muy probablemente utilizando otras vías de baja energía para la transferencia de carga en PSI.

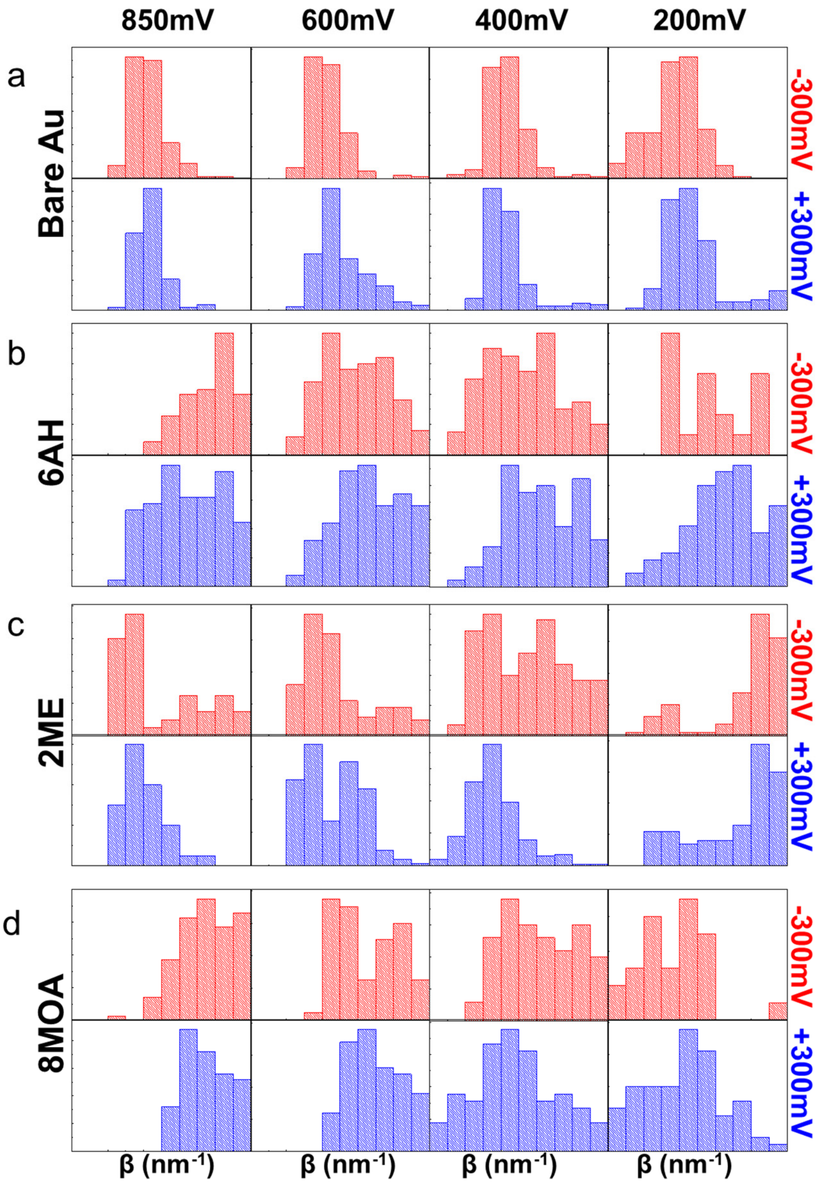

Figura 8.6. Representación estadística de los factores de decaimiento de corriente β de PSI sobre las distintas funcionalizaciones: a) electrodo de oro sin funcionalización, b) SAM de 6-amino hexanotiol, c)SAM de 2-aminoetanol, d)SAM de ácido 8-mercaptooctanoico. Los potenciales de muestra utilizados son U_S = 200mV, 400 mV, 600 mV, 850 mV, de izquierda a derecha. Los potenciales de bias utilizados son U_{bias}= -300mV (rojo) y U_{bias} =+300mV (azul).

Curvas corriente-potencial: Experimentos con iluminación.

Realizamos estudios preliminares estudiando el efecto de la iluminación sobre las medidas de corriente-distancia de PSI unido a electrodos funcionalizados con mercaptoetanol. Se realizaron curvas en oscuridad y bajo iluminación.

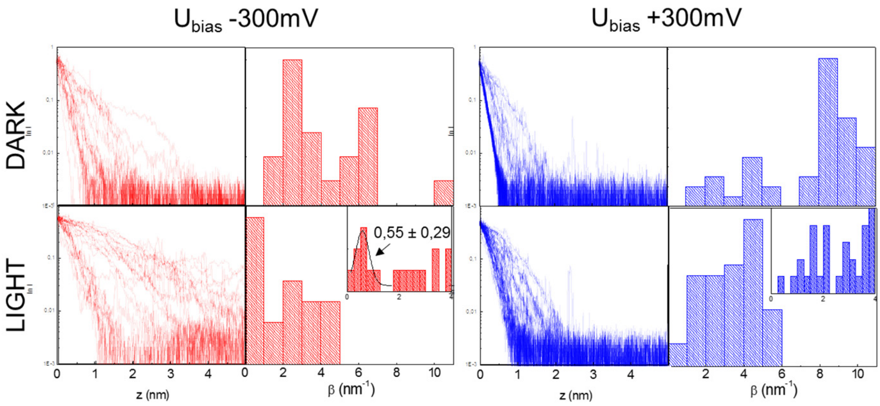

Figura 8.7. Curvas IZ y su representación estadística para PSI sobre electrodos de oro funcionalizados con SAM de 2-mercaptoetanol obtenidas para U_S = 200mV y bias positivos (+300 mV, azul) y negativos (-300mV, rojo). Experimentos realizados en condiciones de oscuridad (panel superior) y bajo iluminación de luz roja (panel inferior). La corriente al iniciar las curvas siempre se mantuvo a 0.5nA.

Tanto para bias positivos como negativos, el factor de decaimiento β era inferior bajo iluminación. La interpretación de estos resultados requerirán experimentos adicionales en una nueva disposición de ECSTM con la iluminación mejorada.

7. Conclusiones.

En esta tesis se abordó el estudio de las proteínas ET utilizando Scanning Probe Microscopies bajo control electroquímico. Los casos de estudio fueron dos proteínas ET muy diferentes: la metaloproteína Azurina y el complejo fotosintético Fotosistema I (PSI).

ECTS de la metaloproteína Azurina mostró su comportamiento de rectificación de corriente bajo control electroquímico. Obtuvimos el valor de potencial de transición (TV) de Azurina tanto en configuraciones de túnel como en cableado. TV marca la transición entre dos regímenes de conductancia que están de acuerdo con la actividad biológica de la azurina: intercambio de carga y transporte. El TV está relacionado con la barrera de tunel desarrollada entre la molécula y los electrodos. El valor más bajo de TV para la configuración cableada con respecto a la configuración de túnel refleja el acoplamiento más fuerte de azurina con la sonda, lo que reduce la barrera de energía entre ellos. Estos resultados sugieren que la ET biológica podría ser modulada por el acoplamiento electrónico entre las parejas redox.

Desarrollamos un método para mejorar la resolución y la recopilación de datos del ECTS. Este nuevo método nos permitió obtener imágenes de conductancia diferencial de una superficie bajo control electroquímico. La técnica fue validada caracterizando la oxidación reversible de un electrodo de hierro, cuya conductancia y topografía fueron monitoreadas simultáneamente en diferentes estados redox. Los cambios de conductancia entre hierro reducido y oxidado medido con esta técnica estuvieron de acuerdo con los resultados previamente publicados. Se realizaron imágenes de conductancia diferencial para caracterizar la metaloproteína Azurina, revelando un punto de alta conductancia submolecular, indicando la existencia de una vía ET hacia un sitio de acoplamiento electrónico localizado y alto.

Usando las puntas de AFM-SECM proporcionadas por el Dr. Demaille estudiamos el sistema Azurina-Au. Realizamos dos tipos de experimentos: espectroscopia de corriente-potencial a fuerza controlada y espectroscopia de fuerza y corriente-distancia. Ambos tipos de medidas mostraron que la conductancia en la unión Au-Azurina-Au aumentaba con la fuerza aplicada sobre la unión. La dependencia de la fuerza aplicada por la conductancia cambió con el estado redox de la proteína: la fuerza requerida para que la corriente fluya a través de Au-Azurina-Au es mayor cuando la proteína está reducida. El aumento de la conductancia al aumentar la fuerza aplicada podría deberse a una serie de factores: Un aumento en el área de contacto, una distancia reducida entre la punta y el sustrato Au, cambios en la estructura o cambios en el mecanismo ET. Estos factores pueden contribuir al aumento de la conductancia a través de la unión, pero la diferencia entre los estados redox sólo puede explicarse a través de un cambio en el mecanismo ET, ya que no hay evidencia de cambios estructurales entre los estados redox en Azurina.

El fotosistema I (PSI) se adsorbió en electrodos de Au a través de diferentes estrategias, pero en diferentes grados. Los sistemas que mostraron mayor cobertura y adsorción más homogénea fueron los electrodos funcionalizados con 2-mercaptoetanol y ácido 8-mercaptooctanoico. PSI retuvo su actividad electroquímica en ambos, y produjo generación de fotocorriente tras la iluminación en las dos superficies. El PSI también se adsorbe sobre electrodos de oro y electrodos de oro funcionalizados con 6-aminohexanotiol, pero con una baja cobertura de la superficie y una adsorción heterogénea, creando islas y agregados de la proteína y / o el surfactante sobre la superficie.

Los cuatro sistemas fueron adecuados para realizar imagen ECSTM, tres de ellos en una variedad de potenciales de la muestra. La altura aparente de las moléculas PSI estaba de acuerdo con los valores reportados en la literatura. La altura aparente de PSI fue independiente del bias aplicado, pero cambió con el potencial de muestra, lo que sugiere que el mecanismo de transferencia ET tiene pasos redox dependientes.

Las medidas espectroscópicas de corriente-distancia mostraron que PSI presenta valores bajos de decaimiento β, de acuerdo con los reportados para las proteínas ET en otros sistemas. También obtuvimos valores superbajos de β en algunos de los sistemas, bajo ciertas condiciones.

Dado que estamos trabajando en la oscuridad, y no estamos abordando los niveles moleculares de la cadena ET biológica, estos resultados sugieren que hay por lo menos dos caminos de transferencia de carga diferentes alternativos a la vía biológica en PSI. La vía de transferencia de carga con valores superbajos de β sólo estaba activa bajo ciertas condiciones potenciales de muestra y bias, lo que sugiere que la transferencia electrónica implica algún centro redox, y que tiene una direccionalidad a través de la proteína.

Appendix I

Symbols and Acronyms

2ME	2- mercaptoethanol
6AHT	6-amino-1-hexanethiol
8MOA	8-mercaptooctanoic acid
β	Distance decay factor
γ	Probe coupling
ΔG^o	Gibbs free energy
η	overpotential
ξ	Substrate coupling
A_0	Chlorophyll-a in Photosystem I
A_1	Phylloquinone in Photosystem I
ac	Alternating current
AFM	Atomic Force Microscopy
ALD	Atomic Layer Deposition
ATP	Adenosine triphosphate
Az	Azurin
BCA	Bicinchoninic acid
cAFM	Conductive Atomic Force Microscopy
CE	Counter Electrode
Cryo-EM	Cryogenic Electron Microscopy
Cys	Cysteine
d_{AB}	Distance between acceptor and donor
DDM	dodecyl-β-maltoside
DECC	Differential Electrochemical Conductance
DNA	Deoxyribonucleic acid
e^-	electron
ECSTM	Electrochemical Scanning Tunneling Microscopy
ECSTM-BJ	Electrochemical Scanning Tunneling Microscopy - Break Junctions
ECTS	Electrochemical Tunneling Spectroscopy
EDP	Electrophoretic Deposition Paint
EOC	Oxygen-evolving complex
ET	Electron Transfer
F_A	Iron sulfur Cluster in Photosystem I

F_B	Iron sulfur Cluster in Photosystem I
Fd	Ferredoxin
FR	Flickering Resonance
F_X	Iron sulfur Cluster in Photosystem I
G	Conductance
Go	Conductance Quantum
h	Planck constant
H_{AB}	Electronic coupling strength between acceptor and donor at the transition state
HiPIPs	High Potential Iron Sulfur Proteins
His	Histidine
I	Current
I_{blink}	Current at the blink
I_T	Tunneling current
I-t	Current-Time
I-V	Current Voltage
I-z	Current-Distance
k_B	Boltzmann constant
k_{ET}	Electron transfer rate
KPFM	Kelvin Probe Force Microscopy
LDOS	Local Density of States
LED	Light Emitting Diode
LEM	Laboratoire d'Electrochemie Moleculaire
Lhca	Light Harvesting complex a
Lhcb	Light Harvesting complex b
LHCI	Light Harvesting complex I
LHCII	Light Harvesting complex II
LRET	Long Range Electron Transfer
Met	Methionine
NAD/NADH	Nicotinamide adenine dinucleotide (oxidized/reduced)
NADP/NADPH	Nicotinamide adenine dinucleotide phosphate (oxidized/reduced)
NHE	Normal hydrogen electrode

NP	Nanoparticle
OCP	Open Circuit Potential
P680	Special pair of chlorophylls at Photosystem II
P700	Special pair of chlorophylls at Photosystem I
PBS	Phosphate-buffered saline
PC	Plastocyanin
PDB	Protein Data Bank
PSI	Photosystem I
PSII	Photosystem II
Psa	Photosystem I subunit
Q	Quinone
RCI	Reaction Center
RE	Reference Electrode
SAM	Self-Assembled Monolayer
SCE	Saturated calomel electrode
SE	Superexchange mechanism
SECM	Scanning Electrochemical Microscopy
SNOM	Near-field scanning optical microscopy
SPM	Scanning Probe Microscopy
STM	Scanning Tunneling Microscopy
STS	Scanning Tunneling Spectroscopy
TV	Transition Voltage
TVS	Transition Voltage Spectroscopy
U	Potential
U_{bias}	Bias Potential
UHV	Ultra High Vacuum
U_P, U_{Probe}	Probe potential
UQ	Ubiquinone
U_S, U_{Sample}	Sample potential
UV	Ultra Violet
UV-vis	Ultra Violet- Visible
WE	Working Electrode
Y_Z	Tyrosine at Photosystem II, adjacent to P680

Appendix II

Publications and Communications

Publications

M. López-Martínez, J. M. Artés, V. Sarasso, M. Carminati, I. Díez-Pérez, F. Sanz & P. Gorostiza. Differential electrochemical conductance imaging at the nanoscale. *In revision.*

J. M. Artés, M. López-Martínez, I. Díez-Pérez, F. Sanz & P. Gorostiza. Nanoscale charge transfer in redox proteins and DNA: Towards biomolecular electronics. Electrochimica Acta 2014 140, 83-95

J. M. Artés, M. López-Martínez, I. Díez-Pérez, F. Sanz & P. Gorostiza. Conductance Switching in Single Wired Redox Proteins. Small. 2014 1013, 2537-2541

J. M. Artés, M. López-Martínez, A. Giraudet, I. Díez-Pérez, F. Sanz, and P. Gorostiza. Current-Voltage Characteristics and Transition Voltage Spectroscopy of Individual Redox Proteins. Journal of the American Chemical Society 2012 134 (50), 20218-20221

Communications

M .López-Martínez, J.M. Artés, I. Díez-Pérez, F. Sanz and P. Gorostiza. Conductance imaging of electronic materials and redox proteins in aqueous solution at the nanoscale. 4th International Winterschool on Bioelectronics. 2017. Kirchberg in Tirol, Austria. Oral Presentation: M. López-Martínez

M. López-Martínez, J.M. Artés, I. Díez-Pérez, F. Sanz and P. Gorostiza. Conductance imaging of redox proteins in solution at the nanoscale. 9th IBEC symposium. 2016. Barcelona, Spain. Poster Presentation: M. López-Martínez

M. López-Martínez, J.M. Artés, I. Díez-Pérez, F. Sanz and P. Gorostiza. Developing new approaches to characterize charge transport in nanoscale junctions under electrochemical conditions. Fuerzas y Tunel. 2016. Girona, Spain. Oral Presentation: M. López-Martínez

M. López-Martínez, J.M. Artés, I. Díez-Pérez, F. Sanz and P. Gorostiza. Conductance imaging of electronic materials and redox proteins in aqueous solution at the nanoscale. 8th International Conference on Molecular Electronics. 2016. Paris, France. Oral Presentation: M. López-Martínez

M. López-Martínez, J.M. Artés, I. Díez-Pérez, F. Sanz and P. Gorostiza. Conductance imaging of electronic materials and redox proteins in aqueous solution at the nanoscale. 67th Annual Meeting of the International Society of Electrochemistry. 2016. The Hague, The Netherlands. Poster Presentation: I. Díez-Pérez.

M. López-Martínez, A. Anne, A. Chovin, F. Sanz, C. Demaille, I. Díez-Pérez and P. Gorostiza. Electrochemical Force Microscopy on Azurin Protein. 8th IBEC Symposium. 2015 Barcelona, Spain. Poster presentation: M. López-Martínez

M. López-Martínez and B. Gumi. Let's go to the nano: Scanning Probe Microscopies. Jornada d'Investigadors Predoctorals Interdisciplinària 2016. Barcelona, Spain. Oral Presentation.

M. López-Martínez, J.M. Artés, I. Díez-Pérez, F. Sanz and P. Gorostiza. Nanoscale Conductance imaging of electronic materials and redox proteins in aqueous solution. V Jornada de Biofísica. 2014. Barcelona, Spain. Oral Presentation: M. López Martínez

M. López-Martínez, J.M. Artés, I. Díez-Pérez, F. Sanz and P. Gorostiza. Nanoscale Conductance imaging of electronic materials and redox proteins in aqueous solution. NanoBio&Med 2014 International Conference. Barcelona, España. Poster Presentation: M. López-Martínez

J.M. Artés, M. López-Martínez, I. Díez-Pérez, F. Sanz and P. Gorostiza. Electrochemical Properties of the Redox Protein Azurin at the Single Molecule Level. 64th Annual Meeting of the International Society of Electrochemistry. 2013 Queretaro, Mexico. Oral Presentation: J. M. Artés

M. López-Martínez, J. M. Artés, I. Díez-Pérez, F. Sanz, and P. Gorostiza. Electronic Properties of Electrochemical and Bioelectrochemical Systems Studied By Diferential Conductance ECSTM. Vuitena Trobada de Joves Investigadors dels Països Catalans. 2013. Andorra La Vella, Andorra. Oral Presentation: M. López- Martínez

M. López-Martínez, J. M. Artés, I. Díez-Pérez, F. Sanz, and P. Gorostiza. Estudio de Sistemas Electroquímicos y Bioelectroquímicos mediante Differential Conductance Electrochemical Scanning Tunneling Microscopy (ECSTM). XXXIV Reunión del Grupo de Electroquímica del Grupo De Electroquímica de la RSEQ. 2013. Valencia, Spain. Oral Presentation: M. López-Martínez.

J.M. Artés, M. López-Martínez, I. Díez-Pérez, F. Sanz and P. Gorostiza. Electroquímica de Metaloproteínas a Nivel de Moléculas Individuales. Azurina: un Transistor Molecular. XXXIII Reunión del Grupo de Electroquímica de la RSEQ 2012. Madrid, Spain. Oral Presentation: J. M. Artés

M López-Martínez, J.M. Artes, I Díez-Pérez, F Sanz & P Gorostiza. Electronic Properties of Electrochemical and Bioelectrochemical Systems studied by Differential Conductance ECSTM. Vth IBEC Symposium on Bioengineering and Nanomedicine. 2012. Barcelona, Spain. Poster Presentation: M. López-Martínez

Acknowledgements

This thesis was carried out at the Physical Chemistry department of the University of Barcelona and the Institute for Bioengineering of Barcelona (IBEC), thanks to a FPI fellowship code BES-2013-066430. During this thesis two research stays were done in Dr Christophe Demaille's group at the Laboratoire d'Electrochemie Moleculaire in Paris, France, thanks to two mobility grants EEBB-I-15-09374 and EEBB-I-16-11575.

Llegando a la fase final de esta etapa, es inevitable echar la vista atrás y pensar en todas las personas que me han ayudado a llegar hasta aquí. Creo que es imposible mencionar a todos los que me habéis ayudado, de una manera u otra, a construir esta tesis, así que bueno, espero que me perdonéis, porque esto va a quedar incompleto seguro. Y porque me va a quedar bastante cursi, también.

Lo primero es lo primero, y me gustaría agradecer a todo el grupo de Nanoprobes y Nanoswitches. A Fausto, que me abrió las puertas del laboratorio, y a mis dos supervisores, Pau e Isma, por darme la oportunidad de iniciar mi carrera investigadora con ellos y orientarme en mis primeros pasos. Muchísimas gracias a Pau, además, por ser siempre tan optimista, y tener siempre palabras de ánimo. A Isma, gracias también por estar siempre disponible para resolver cualquier duda, bajar a ayudarnos cuando teníamos algún problema, y ponerte a pelar cables si hacía falta. También tengo que agradecer a Juanma, que me llevó de la manita al principio, con una paciencia infinita. Muchas gracias por siempre estar pendiente, incluso ahora que ha pasado el tiempo. Marina, me has ayudado tanto estos años que no sé cómo agradecerte. Tu puerta siempre ha estado abierta para mí, siempre que he tenido alguna duda (científica o no). He aprendido muchísimo de ti estos años, y no puedo estar más contenta de haberme encontrado contigo. Al resto del grupo de Nanoprobes and Nanoswitches, a los del Parc, y a los de Bellvitge, también muchisimas gracias. A los que me acogieron cuando llegué, Lorena, Andrés, Kay, Silvia, Anna, Javi, y un largo etc, y a Albert y Marta que llegaron conmigo. A los que vinieron después, los que vinieron de paso, como Vero y Claudia, y los que se quedaron, Berta, Davia, Fabio, Manu y todos los demás. A todos vosotros, gracias por acogerme tan bien, por conseguir que esté tan a gusto en el lab, y por llenar esta tesis de buenos momentos y mucho (mucho) café. Espero que no os importe, pero tengo que destacar a Marta, que ha sido mi compañera de batallas durante todo este tiempo. Marta, me ha encantado hacer este camino contigo y solo espero haberte ayudado tanto como tú me has ayudado a mí. También a Berta, porque contigo he llorado y reído en el laboratorio (a veces a la vez) como con nadie, y eres una de las mejores personas que me llevo de la tesis.

Fuera del grupo, también hay mucha gente del IBEC que me ha acompañado estos años y ha hecho mucho más agradable el camino. Claudia, Anna, Cris, Marc, Carlos, y un largo etcétera, por todo lo que hemos pasado juntos, y por las cerves y los cafés tomados, y en general, por formar parte de esta experiencia.

I also want to thank Dr. Christophe Demaille for giving me the opportunity of doing two research stays in his lab in Paris. I want to thank everybody in the group, Agnes, Arnaud, Khalil, Cecilia, Anisha and Carlos, for welcoming me to your lab and helping me with any problem I had.

No me quiero dejar a la gente de fuera del laboratorio, gente que, algunos sin ser demasiado conscientes, me ha ayudado muchísimo a llegar aquí. A mis compañeros de química de la UA, Alberto, Rosi, Toni, Vane, Ali, Joaquín y Sergio. Con ellos realmente empecé esta aventura, en los laboratorios de prácticas, y en los pasillos del ctq, y me encanta poder decir que me han acompañado hasta aquí. A mis amigos de Albacete, porque son mi segunda familia. Con la distancia, nos vemos poco, pero la verdad es que una caña con vosotros me alegra el día, y ya no me puedo imaginar las fechas señaladas sin veros, como las buenas familias. Especialmente, espero que los demás lo entenderán, quiero darle las gracias a Ana, Haydée, Cris, Mariángeles y Miriam, por siempre, siempre estar ahí. Además de por todo eso, y por acompañarme en Barcelona, muchísimas gracias, Cris, por diseñar la portada de esta tesis.

A mi familia, todo lo que ponga aquí se va a quedar corto. A mis padres, gracias por todo el esfuerzo que han hecho y hacen cada día para que yo esté aquí. A mi hermano, que siempre me ha animado en todo lo que he hecho, y que ahora con sus hijos me arranca una sonrisa todos los días. Y a Mari y a Victor, también, muchísimas gracias.

Y, sobre todo, a João, que es el mejor compañero de viaje. Muchas gracias por venir conmigo.

References

1. Marcus, R. A.; Sutin, N., Electron Transfers In Chemistry And Biology. *Biochimica Et Biophysica Acta* **1985,** *811* (3), 265-322.

2. Davis, J. J.; Morgan, D. A.; Wrathmell, C. L.; Axford, D. N.; Zhao, J.; Wang, N., Molecular bioelectronics. *Journal of Materials Chemistry* **2005,** *15* (22), 2160-2174.

3. Liu, J.; Chakraborty, S.; Hosseinzadeh, P.; Yu, Y.; Tian, S.; Petrik, I.; Bhagi, A.; Lu, Y., Metalloproteins Containing Cytochrome, Iron-Sulfur, or Copper Redox Centers. *Chemical Reviews* **2014,** *114* (8), 4366-4469.

4. Solomon, E. I.; Hadt, R. G.; Snyder, B. E. R., Activating Metal Sites for Biological Electron Transfer. *Israel Journal of Chemistry* **2016,** *56* (9-10), 649-659.

5. Bertini, I.; Cavallaro, G.; Rosato, A., Cytochrome c: Occurrence and functions. *Chemical Reviews* **2006,** *106* (1), 90-115.

6. Meyer, J., Iron-sulfur protein folds, iron-sulfur chemistry, and evolution. *Journal of Biological Inorganic Chemistry* **2008,** *13* (2), 157-170.

7. Stephens, P. J.; Jollie, D. R.; Warshel, A., Protein control of redox potentials of iron-sulfur proteins. *Chemical Reviews* **1996,** *96* (7), 2491-2513.

8. Bruschi, M.; Guerlesquin, F., Structure, Function And Evolution Of Bacterial Ferredoxins. *Fems Microbiology Letters* **1988,** *54* (2), 155-175.

9. Cowan, J. A.; Lui, S. M., Structure-function correlations in high-potential iron proteins. *Advances in Inorganic Chemistry, Vol 45* **1998,** *45*, 313-350.

10. Solomon, E. I.; Sundaram, U. M.; Machonkin, T. E., Multicopper oxidases and oxygenases. *Chemical Reviews* **1996,** *96* (7), 2563-2605.

11. Solomon, E. I.; Hare, J. W.; Dooley, D. M.; Dawson, J. H.; Stephens, P. J.; Gray, H. B., Spectroscopic Studies Of Stellacyanin, Plastocyanin, And Azurin - Electronic-Structure Of The Blue Copper Sites. *Journal of the American Chemical Society* **1980,** *102* (1), 168-178.

12. Alessandrini, A.; Corni, S.; Facci, P., Unravelling single metalloprotein electron transfer by scanning probe techniques. *Physical Chemistry Chemical Physics* **2006,** *8* (38), 4383-4397.

13. Parr, S. R.; Barber, D.; Greenwood, C.; Brunori, M., Electron-Transfer Reaction Between Azurin And Cytochrome-C Oxidase From Pseudomonas-Aeruginosa. *Biochemical Journal* **1977,** *167* (2), 447-455.

14. Adman, E. T.; Jensen, L. H., Structural Features Of Azurin At 2.7 A-Resolution. *Israel Journal of Chemistry* **1981,** *21* (1), 8-12.

15. Marreiros, B. C.; Calisto, F.; Castro, P. J.; Duarte, A. M.; Sena, F. V.; Silva, A. F.; Sousa, F. M.; Teixeira, M.; Refojo, P. N.; Pereira, M. M., Exploring membrane respiratory chains. *Biochimica Et Biophysica Acta-Bioenergetics* **2016,** *1857* (8), 1039-1067.

16. Nicholls, D., *Bioenergetics*. Academic Press: 2013.

17. Fiedorczuk, K.; Letts, J. A.; Degliesposti, G.; Kaszuba, K.; Skehel, M.; Sazanov, L. A., Atomic structure of the entire mammalian mitochondrial complex I. *Nature* **2016,** *538* (7625), 406-+.

18. Letts, J. A.; Fiedorczuk, K.; Sazanov, L. A., The architecture of respiratory supercomplexes. *Nature* **2016,** *537* (7622), 644-+.

19. Gu, J.; Wu, M.; Guo, R.; Yan, K.; Lei, J.; Gao, N.; Yang, M., The architecture of the mammalian respirasome. *Nature* **2016,** *537* (7622), 639-+.

20. Guerrero-Castillo, S.; Baertling, F.; Kownatzki, D.; Wessels, H. J.; Arnold, S.; Brandt, U.; Nijtmans, L., The Assembly Pathway of Mitochondrial Respiratory Chain Complex I. *Cell Metabolism* **2017,** *25* (1), 128-139.

21. Vinothkumar, K. R.; Zhu, J.; Hirst, J., Architecture of mammalian respiratory complex I. *Nature* **2014,** *515* (7525), 80-+.

22. Zhu, J.; Vinothkumar, K. R.; Hirst, J., Structure of mammalian respiratory complex I. *Nature* **2016,** *536* (7616), 354-8.

23. Berrisford, J. M.; Baradaran, R.; Sazanov, L. A., Structure of bacterial respiratory complex I. *Biochimica Et Biophysica Acta-Bioenergetics* **2016,** *1857* (7), 892-901.

24. Hirst, J.; Roessler, M. M., Energy conversion, redox catalysis and generation of reactive oxygen species by respiratory complex I. *Biochimica Et Biophysica Acta-Bioenergetics* **2016,** *1857* (7), 872-883.

25. Page, C. C.; Moser, C. C.; Chen, X. X.; Dutton, P. L., Natural engineering principles of electron tunnelling in biological oxidation-reduction. *Nature* **1999,** *402* (6757).

26. Sun, F.; Huo, X.; Zhai, Y. J.; Wang, A. J.; Xu, J. X.; Su, D.; Bartlam, M.; Rao, Z. H., Crystal structure of mitochondrial respiratory membrane protein complex II. *Cell* **2005,** *121* (7), 1043-1057.

27. Berry, E. A.; Guergova-Kuras, M.; Huang, L. S.; Crofts, A. R., Structure and function of cytochrome bc complexes. *Annual Review of Biochemistry* **2000,** *69*, 1005-1075.

28. Millar, A. H.; Whelan, J.; Soole, K. L.; Day, D. A., Organization and Regulation of Mitochondrial Respiration in Plants. *Annual Review of Plant Biology, Vol 62* **2011,** *62*, 79-104.

29. Mazor, Y.; Borovikova, A.; Nelson, N., The structure of plant photosystem I super-complex at 2.8 angstrom resolution. *Elife* **2015,** *4*.

30. Nelson, N.; Ben-Shem, A., The complex architecture of oxygenic photosynthesis. *Nature Reviews Molecular Cell Biology* **2004,** *5* (12), 971-982.

31. Nelson, N.; Yocum, C. F., Structure and function of photosystems I and II. *Annual Review of Plant Biology* **2006,** *57*, 521-565.

32. Croce, R.; van Amerongen, H., Light-harvesting in photosystem I. *Photosynthesis Research* **2013,** *116* (2-3), 153-166.

33. Nelson, N.; Junge, W., Structure and Energy Transfer in Photosystems of Oxygenic Photosynthesis. *Annual Review of Biochemistry, Vol 84* **2015,** *84*, 659-683.

34. Jordan, P.; Fromme, P.; Witt, H. T.; Klukas, O.; Saenger, W.; Krauss, N., Three-dimensional structure of cyanobacterial photosystem I at 2.5 angstrom resolution. *Nature* **2001,** *411* (6840), 909-917.

35. Ben-Shem, A.; Frolow, F.; Nelson, N., Crystal structure of plant photosystem I. *Nature* **2003,** *426* (6967), 630-635.

36. Stroebel, D.; Choquet, Y.; Popot, J. L.; Picot, D., An atypical haem in the cytochrome b(6)f complex. *Nature* **2003,** *426* (6965), 413-418.

37. Loll, B.; Kern, J.; Saenger, W.; Zouni, A.; Biesiadka, J., Towards complete cofactor arrangement in the 3.0 angstrom resolution structure of photosystem II. *Nature* **2005,** *438* (7070), 1040-1044.

38. Amunts, A.; Drory, O.; Nelson, N., The structure of a plant photosystem I supercomplex at 3.4 angstrom resolution. *Nature* **2007,** *447* (7140), 58-63.

39. Amunts, A.; Toporik, H.; Borovikova, A.; Nelson, N., Structure Determination and Improved Model of Plant Photosystem I. *Journal of Biological Chemistry* **2010,** *285* (5), 3478-3486.

40. Umena, Y.; Kawakami, K.; Shen, J.-R.; Kamiya, N., Crystal structure of oxygen-evolving photosystem II at a resolution of 1.9 angstrom. *Nature* **2011,** *473* (7345), 55-U65.

41. Ferreira, K. N.; Iverson, T. M.; Maghlaoui, K.; Barber, J.; Iwata, S., Architecture of the photosynthetic oxygen-evolving center. *Science* **2004,** *303* (5665), 1831-1838.

42. Kurisu, G.; Zhang, H. M.; Smith, J. L.; Cramer, W. A., Structure of the cytochrome b(6)f complex of oxygenic photosynthesis: Tuning the cavity. *Science* **2003,** *302* (5647), 1009-1014.

43. Mazor, Y.; Borovikova, A.; Caspy, I.; Nelson, N., Structure of the plant photosystem I supercomplex at 2.6 A resolution. *Nature plants* **2017,** *3*, 17014-17014.

44. Zouni, A.; Witt, H. T.; Kern, J.; Fromme, P.; Krauss, N.; Saenger, W.; Orth, P., Crystal structure of photosystem II from Synechococcus elongatus at 3.8 angstrom resolution. *Nature* **2001,** *409* (6821), 739-743.

45. Barber, J., Photosystem II: a multisubunit membrane protein that oxidises water. *Current Opinion in Structural Biology* **2002,** *12* (4), 523-530.

46. Kuhlbrandt, W.; Wang, D. N.; Fujiyoshi, Y., Atomic Model Of Plant Light-Harvesting Complex By Electron Crystallography. *Nature* **1994,** *367* (6464), 614-621.

47. Blankenship, R. E., *Molecular Mechanisms of Photosynthesis, 2nd Edition*. Wiley-Blackwell: 2014.

48. Hurt, E.; Hauska, G., A Cytochrome F-B6 Complex Of 5 Polypeptides With Plastoquinol-Plastocyanin-Oxidoreductase Activity From Spinach-Chloroplasts. *European Journal of Biochemistry* **1981,** *117* (3), 591-599.

49. Nelson, N.; Ben-Shem, A., Photosystem I reaction center: past and future. *Photosynthesis Research* **2002,** *73* (1-3), 193-206.

50. Scheller, H. V.; Jensen, P. E.; Haldrup, A.; Lunde, C.; Knoetzel, J., Role of subunits in eukaryotic Photosystem I. *Biochimica Et Biophysica Acta-Bioenergetics* **2001,** *1507* (1-3), 41-60.

51. Amunts, A.; Nelson, N., Plant Photosystem I Design in the Light of Evolution. *Structure* **2009,** *17* (5), 637-650.

52. Ben-Shem, A.; Frolow, F.; Nelson, N., Light-harvesting features revealed by the structure of plant Photosystem I. *Photosynthesis Research* **2004,** *81* (3), 239-250.

53. Bailey, S.; Walters, R. G.; Jansson, S.; Horton, P., Acclimation of Arabidopsis thaliana to the light environment: the existence of separate low light and high light responses. *Planta* **2001,** *213* (5), 794-801.

54. Chitnis, P. R., Photosystem I: Function and physiology. *Annual Review of Plant Physiology and Plant Molecular Biology* **2001,** *52*, 593-626.

55. McCarty, R. E.; Evron, Y.; Johnson, E. A., The chloroplast ATP synthase: A rotary enzyme? *Annual Review of Plant Physiology and Plant Molecular Biology* **2000,** *51*, 83-109.

56. Gray, H. B.; Winkler, J. R., Electron flow through metalloproteins. *Biochimica Et Biophysica Acta-Bioenergetics* **2010,** *1797* (8), 1563-1572.

57. Farver, O.; Pecht, I., Electron transfer in blue copper proteins. *Coordination Chemistry Reviews* **2011,** *255* (7-8).

58. Gray, H. B.; Winkler, J. R., Electron tunneling through proteins. *Quarterly Reviews of Biophysics* **2003,** *36* (3).

59. Vuilleumier, R.; Tay, K. A.; Jeanmairet, G.; Borgis, D.; Boutin, A., Extension of Marcus Picture for Electron Transfer Reactions with Large Solvation Changes. *Journal of the American Chemical Society* **2012,** *134* (4).

60. Reece, S. Y.; Nocera, D. G., Proton-Coupled Electron Transfer in Biology: Results from Synergistic Studies in Natural and Model Systems. *Annual Review of Biochemistry* **2009,** *78*, 673-699.

61. Zhang, J.; Kuznetsov, A. M.; Medvedev, I. G.; Chi, Q.; Albrecht, T.; Jensen, P. S.; Ulstrup, J., Single-molecule electron transfer in electrochemical environments. *Chemical Reviews* **2008,** *108* (7), 2737-2791.

62. Kuznetsov, A. M.; Ulstrup, J., Theory of electron transfer at electrified interfaces. *Electrochimica Acta* **2000,** *45* (15-16), 2339-2361.

63. Kuznetsov, A. M.; Ulstrup, J., Proton and proton-coupled electron transfer with paradigms towards single-molecule systems. *Journal of Physical Organic Chemistry* **2010,** *23* (7), 647-659.

64. Regan, J. J.; Dibilio, A. J.; Langen, R.; Skov, L. K.; Winkler, J. R.; Gray, H. B.; Onuchic, J. N., Electron-Tunneling In Azurin - The Coupling Across A Beta-Sheet. *Chemistry & Biology* **1995,** *2* (7), 489-496.

65. Gray, H. B.; Winkler, J. R., Long-range electron transfer. *Proceedings of the National Academy of Sciences of the United States of America* **2005,** *102* (10), 3534-3539.

66. Winkler, J. R.; Gray, H. B., Electron Flow through Metalloproteins. *Chemical Reviews* **2014,** *114* (7), 3369-3380.

67. Winkler, J. R.; Gray, H. B., Long-Range Electron Tunneling. *Journal of the American Chemical Society* **2014,** *136* (8), 2930-2939.

68. Blumberger, J., Recent Advances in the Theory and Molecular Simulation of Biological Electron Transfer Reactions. *Chemical Reviews* **2015,** *115* (20), 11191-11238.

69. Bortolotti, C. A.; Borsari, M.; Sola, M.; Chertkova, R.; Dolgikh, D.; Kotlyar, A.; Facci, P., Orientation-dependent kinetics of heterogeneous electron transfer for cytochrome c immobilized on gold: Electrochemical determination and theoretical prediction. *Journal of Physical Chemistry C* **2007,** *111* (32), 12100-12105.

70. Zhan, T.; Xi, M.; Wang, Y.; Sun, W.; Hou, W., Direct electrochemistry and electrocatalysis of myoglobin immobilized on Fe2O3 nanoparticle-sodium alginate-ionic liquid composite-modified electrode. *Journal of Colloid and Interface Science* **2010,** *346* (1), 188-193.

71. Chi, Q. J.; Farver, O.; Ulstrup, J., Long-range protein electron transfer observed at the single-molecule level: In situ mapping of redox-gated tunneling resonance. *Proceedings of the National Academy of Sciences of the United States of America* **2005,** *102* (45), 16203-16208.

72. Hirst, J., Mitochondrial Complex I. *Annual Review of Biochemistry, Vol 82* **2013,** *82*, 551-575.

73. Moser, C. C.; Page, C. C.; Dutton, P. L., Darwin at the molecular scale: selection and variance in electron tunnelling proteins including cytochrome c oxidase. *Philosophical Transactions of the Royal Society B-Biological Sciences* **2006,** *361* (1472), 1295-1305.

74. Fontecilla-Camps, J. C.; Volbeda, A.; Cavazza, C.; Nicolet, Y., Structure/function relationships of NiFe - and FeFe -hydrogenases. *Chemical Reviews* **2007,** *107* (10), 4273-4303.

75. Clarke, T. A.; Edwards, M. J.; Gates, A. J.; Hall, A.; White, G. F.; Bradley, J.; Reardon, C. L.; Shi, L.; Beliaev, A. S.; Marshall, M. J.; Wang, Z.; Watmough, N. J.; Fredrickson, J. K.; Zachara, J. M.; Butt, J. N.; Richardson, D. J., Structure of a bacterial cell surface decaheme electron conduit. *Proceedings of the National Academy of Sciences of the United States of America* **2011,** *108* (23), 9384-9389.

76. White, G. F.; Shi, Z.; Shi, L.; Wang, Z.; Dohnalkova, A. C.; Marshall, M. J.; Fredrickson, J. K.; Zachara, J. M.; Butt, J. N.; Richardson, D. J.; Clarke, T. A., Rapid electron exchange between surface-exposed bacterial cytochromes and Fe(III) minerals. *Proceedings of the National Academy of Sciences of the United States of America* **2013,** *110* (16), 6346-6351.

77. Moser, C. C.; Anderson, J. L. R.; Dutton, P. L., Guidelines for tunneling in enzymes. *Biochimica Et Biophysica Acta-Bioenergetics* **2010,** *1797* (8), 1573-1586.

78. Warren, J. J.; Ener, M. E.; Vlcek, A., Jr.; Winkler, J. R.; Gray, H. B., Electron hopping through proteins. *Coordination Chemistry Reviews* **2012,** *256* (21-22), 2478-2487.

79. Beratan, D. N.; Betts, J. N.; Onuchic, J. N., Protein Electron-Transfer Rates Set By The Bridging Secondary And Tertiary Structure. *Science* **1991,** *252* (5010), 1285-1288.

80. Beratan, D. N.; Onuchic, J. N.; Hopfield, J. J., Electron-Tunneling Through Covalent And Noncovalent Pathways In Proteins. *Journal of Chemical Physics* **1987,** *86* (8), 4488-4498.

81. Onuchic, J. N.; Beratan, D. N.; Winkler, J. R.; Gray, H. B., Pathway Analysis Of Protein Electron-Transfer Reactions. *Annual Review of Biophysics and Biomolecular Structure* **1992,** *21*, 349-377.

82. Zhang, Y.; Liu, C.; Balaeff, A.; Skourtis, S. S.; Beratan, D. N., Biological charge transfer via flickering resonance. *Proceedings of the National Academy of Sciences of the United States of America* **2014,** *111* (28), 10049-10054.

83. Beratan, D. N.; Liu, C.; Migliore, A.; Polizzi, N. F.; Skourtis, S. S.; Zhang, P.; Zhang, Y., Charge Transfer in Dynamical Biosystems, or The Treachery of (Static) Images. *Accounts of Chemical Research* **2015,** *48* (2), 474-481.

84. Amdursky, N.; Sepunaru, L.; Raichlin, S.; Pecht, I.; Sheves, M.; Cahen, D., Electron Transfer Proteins as Electronic Conductors: Significance of the Metal and Its Binding Site in the Blue Cu Protein, Azurin. *Advanced Science* **2015,** *2* (4).

85. Amdursky, N.; Marchak, D.; Sepunaru, L.; Pecht, I.; Sheves, M.; Cahen, D., Electronic Transport via Proteins. *Advanced Materials* **2014,** *26* (42), 7142-7161.

86. Nocera, D. G.; Winkler, J. R.; Yocom, K. M.; Bordignon, E.; Gray, H. B., Kinetics Of Intramolecular Electron-Transfer From Ru-Ii To Fe-Iii In Ruthenium-Modified Cytochrome-C. *Journal of the American Chemical Society* **1984,** *106* (18), 5145-5150.

87. Farver, O.; Pecht, I., Elucidation of Electron-Transfer Pathways in Copper and Iron Proteins by Pulse Radiolysis Experiments. *Progress in Inorganic Chemistry, Vol 55* **2007,** *55*, 1-78.

88. Moser, C. C.; Dutton, P. L., Engineering Protein-Structure For Electron-Transfer Function In Photosynthetic Reaction Centers. *Biochimica Et Biophysica Acta* **1992,** *1101* (2), 171-176.

89. Winkler, J. R.; Nocera, D. G.; Yocom, K. M.; Bordignon, E.; Gray, H. B., Electron-Transfer Kinetics Of Pentaammineruthenium(Iii)(Histidine-33)-Ferricytochrome-C - Measurement Of The Rate Of Intramolecular Electron-Transfer Between Redox Centers Separated By 15-A In A Protein. *Journal of the American Chemical Society* **1982,** *104* (21), 5798-5800.

90. Bortolotti, C. A.; Siwko, M. E.; Castellini, E.; Ranieri, A.; Sola, M.; Corni, S., The Reorganization Energy in Cytochrome c is Controlled by the Accessibility of the Heme to the Solvent. *Journal of Physical Chemistry Letters* **2011,** *2* (14), 1761-1765.

91. Chi, Q. J.; Zhang, J. D.; Nielsen, J. U.; Friis, E. P.; Chorkendorff, I.; Canters, G. W.; Andersen, J. E. T.; Ulstrup, J., Molecular monolayers and interfacial electron transfer of Pseudomonas aeruginosa azurin on Au(111). *Journal of the American Chemical Society* **2000,** *122* (17), 4047-4055.

92. Eckermann, A. L.; Feld, D. J.; Shaw, J. A.; Meade, T. J., Electrochemistry of redox-active self-assembled monolayers. *Coordination Chemistry Reviews* **2010,** *254* (15-16), 1769-1802.

93. Leger, C.; Bertrand, P., Direct electrochemistry of redox enzymes as a tool for mechanistic studies. *Chemical Reviews* **2008,** *108* (7), 2379-2438.

94. Wei, J. J.; Liu, H. Y.; Khoshtariya, D. E.; Yamamoto, H.; Dick, A.; Waldeck, D. H., Electron-transfer dynamics of cytochrome C: A change in the reaction mechanism with distance. *Angewandte Chemie-International Edition* **2002,** *41* (24), 4700-4703.

95. Winkler, J. R.; Di Bilio, A. J.; Farrow, N. A.; Richards, J. H.; Gray, H. B., Electron tunneling in biological molecules. *Pure and Applied Chemistry* **1999,** *71* (9), 1753-1764.

96. Saboe, P. O.; Conte, E.; Farell, M.; Bazan, G. C.; Kumar, M., Biomimetic and bioinspired approaches for wiring enzymes to electrode interfaces. *Energy & Environmental Science* **2017,** *10* (1), 14-42.

97. Kuchenreuther, J. M.; Grady-Smith, C. S.; Bingham, A. S.; George, S. J.; Cramer, S. P.; Swartz, J. R., High-Yield Expression of Heterologous FeFe Hydrogenases in Escherichia coli. *Plos One* **2010,** *5* (11).

98. Lubner, C. E.; Knoerzer, P.; Silva, P. J. N.; Vincent, K. A.; Happe, T.; Bryant, D. A.; Golbeck, J. H., Wiring an FeFe -Hydrogenase with Photosystem I for Light-Induced Hydrogen Production. *Biochemistry* **2010,** *49* (48), 10264-10266.

99. Wang, J., Electrochemical glucose biosensors. *Chemical Reviews* **2008,** *108* (2), 814-825.

100. Wu, Y.; Hu, S., Biosensors based on direct electron transfer in redox proteins. *Microchimica Acta* **2007,** *159* (1-2), 1-17.

101. Chen, X.; Yan, X.; Khor, K. A.; Tay, B. K., Multilayer assembly of positively charged polyelectrolyte and negatively charged glucose oxidase on a 3D Nafion network for detecting glucose. *Biosensors & Bioelectronics* **2007,** *22* (12), 3256-3260.

102. Rasmussen, M.; Minteer, S. D., Self-powered herbicide biosensor utilizing thylakoid membranes. *Analytical Methods* **2013,** *5* (5), 1140-1144.

103. Chi, Q. J.; Zhang, J. D.; Friis, E. P.; Andersen, J. E. T.; Ulstrup, J., Electrochemistry of self-assembled monolayers of the blue copper protein Pseudomonas aeruginosa azurin on Au(111). *Electrochemistry Communications* **1999,** *1* (3-4), 91-96.

104. Friis, E. P.; Andersen, J. E. T.; Madsen, L. L.; Moller, P.; Ulstrup, J., In situ STM and AFM of the copper protein Pseudomonas aeruginosa azurin. *Journal of Electroanalytical Chemistry* **1997,** *431* (1), 35-38.

105. Artes, J. M.; Diez-Perez, I.; Sanz, F.; Gorostiza, P., Direct Measurement of Electron Transfer Distance Decay Constants of Single Redox Proteins by Electrochemical Tunneling Spectroscopy. *Acs Nano* **2011,** *5* (3), 2060-2066.

106. Artes, J. M.; Diez-Perez, I.; Gorostiza, P., Transistor-like Behavior of Single Metalloprotein Junctions. *Nano letters* **2012,** *12* (6), 2679-84.

107. Gorostiza, P.; Artés, J. M., Scanning Tunneling Microscopy Studies of Immobilized Biomolecules. In *Encyclopedia of Applied Electrochemistry*, Kreysa, G.; Ota, K.-i.; Savinel, R., Eds. Springer New York: 2014; pp 1851-1868.

108. Shih, C.; Museth, A. K.; Abrahamsson, M.; Blanco-Rodriguez, A. M.; Di Bilio, A. J.; Sudhamsu, J.; Crane, B. R.; Ronayne, K. L.; Towrie, M.; Vlcek, A., Jr.; Richards, J. H.; Winkler, J. R.; Gray, H. B., Tryptophan-accelerated electron flow through proteins. *Science* **2008,** *320* (5884), 1760-1762.

109. Beratan, D. N.; Onuchic, J. N.; Betts, J. N.; Bowler, B. E.; Gray, H. B., Electron-Tunneling Pathways In Ruthenated Proteins. *Journal of the American Chemical Society* **1990,** *112* (22), 7915-7921.

110. Skov, L. K.; Pascher, T.; Winkler, J. R.; Gray, H. B., Rates of intramolecular electron transfer in Ru(bpy)(2)(im)(His83)-modified azurin increase below 220 K. *Journal of the American Chemical Society* **1998,** *120* (5), 1102-1103.

111. Langen, R.; Chang, I. J.; Germanas, J. P.; Richards, J. H.; Winkler, J. R.; Gray, H. B., Electron-Tunneling In Proteins - Coupling Through A Beta-Strand. *Science* **1995,** *268* (5218), 1733-1735.

112. Facci, P.; Alliata, D.; Cannistraro, S., Potential-induced resonant tunneling through a redox metalloprotein investigated by electrochemical scanning probe microscopy. *Ultramicroscopy* **2001,** *89* (4), 291-298.

113. Andolfi, L.; Bruce, D.; Cannistraro, S.; Canters, G. W.; Davis, J. J.; Hill, H. A. O.; Crozier, J.; Verbeet, M. P.; Wrathmell, C. L.; Astier, Y., The electrochemical characteristics of blue copper protein monolayers on gold. *Journal of Electroanalytical Chemistry* **2004,** *565* (1), 21-28.

114. Chi, Q. J.; Zhang, J. D.; Andersen, J. E. T.; Ulstrup, J., Ordered assembly and controlled electron transfer of the blue copper protein azurin at gold (111) single-crystal substrates. *Journal of Physical Chemistry B* **2001,** *105* (20), 4669-4679.

115. Khoshtariya, D. E.; Dolidze, T. D.; Shushanyan, M.; Davis, K. L.; Waldeck, D. H.; van Eldik, R., Fundamental signatures of short- and long-range electron transfer for the blue copper protein azurin at Au/SAM junctions.

Proceedings of the National Academy of Sciences of the United States of America **2010,** *107* (7), 2757-2762.

116. Salverda, J. M.; Patil, A. V.; Mizzon, G.; Kuznetsova, S.; Zauner, G.; Akkilic, N.; Canters, G. W.; Davis, J. J.; Heering, H. A.; Aartsma, T. J., Fluorescent Cyclic Voltammetry of Immobilized Azurin: Direct Observation of Thermodynamic and Kinetic Heterogeneity. *Angewandte Chemie-International Edition* **2010,** *49* (33), 5776-5779.

117. Patil, A. V.; Davis, J. J., Visualizing and Tuning Thermodynamic Dispersion in Metalloprotein Monolayers. *Journal of the American Chemical Society* **2010,** *132* (47), 16938-16944.

118. Monari, S.; Battistuzzi, G.; Dennison, C.; Borsari, M.; Ranieri, A.; Siwek, M. J.; Sola, M., Factors Affecting the Electron Transfer Properties of an Immobilized Cupredoxin. *Journal of Physical Chemistry C* **2010,** *114* (50), 22322-22329.

119. Jeuken, L. J. C.; Armstrong, F. A., Electrochemical origin of hysteresis in the electron-transfer reactions of adsorbed proteins: Contrasting behavior of the "blue" copper protein, azurin, adsorbed on pyrolytic graphite and modified gold electrodes. *Journal of Physical Chemistry B* **2001,** *105* (22), 5271-5282.

120. Chi, Q. J.; Zhang, J. D.; Jensen, P. S.; Christensen, H. E. M.; Ulstrup, J., Long-range interfacial electron transfer of metalloproteins based on molecular wiring assemblies. *Faraday Discussions* **2006,** *131*, 181-195.

121. Fujita, K.; Nakamura, N.; Ohno, H.; Leigh, B. S.; Niki, K.; Gray, H. B.; Richards, J. H., Mimicking protein-protein electron transfer: Voltammetry of Pseudomonas aeruginosa azurin and the Thermus thermophilus Cu-A domain at omega-derivatized self-assembled-monolayer gold electrodes. *Journal of the American Chemical Society* **2004,** *126* (43), 13954-13961.

122. Ron, I.; Sepunaru, L.; Itzhakov, S.; Belenkova, T.; Friedman, N.; Pecht, I.; Sheves, M.; Cahen, D., Proteins as Electronic Materials: Electron Transport through Solid-State Protein Monolayer Junctions. *Journal of the American Chemical Society* **2010,** *132* (12), 4131-4140.

123. Amdursky, N.; Pecht, I.; Sheves, M.; Cahen, D., Marked changes in electron transport through the blue copper protein azurin in the solid state upon deuteration. *Proceedings of the National Academy of Sciences of the United States of America* **2013,** *110* (2), 507-512.

124. Sepunaru, L.; Pecht, I.; Sheves, M.; Cahen, D., Solid-State Electron Transport across Azurin: From a Temperature-Independent to a Temperature-Activated Mechanism. *Journal of the American Chemical Society* **2011,** *133* (8), 2421-2423.

125. Yagati, A. K.; Lee, T.; Min, J.; Choi, J.-W., STM and cyclic voltammetric investigation of recombinant azurin-gold nanoparticle hybrids. *Bioelectrochemistry* **2012,** *83*, 8-14.

126. Artes, J. M.; Lopez-Martinez, M.; Diez-Perez, I.; Sanz, F.; Gorostiza, P., Conductance Switching in Single Wired Redox Proteins. *Small* **2014,** *10* (13), 2537-2541.

127. Davis, J. J.; Wrathmell, C. L.; Zhao, J.; Fletcher, J., The tunnelling conductance of molecularly ordered metalloprotein arrays. *Journal of Molecular Recognition* **2004,** *17* (3), 167-173.

128. Li, W. J.; Sepunaru, L.; Amdursky, N.; Cohen, S. R.; Pecht, I.; Sheves, M.; Cahen, D., Temperature and Force Dependence of Nanoscale Electron Transport via the Cu Protein Azurin. *Acs Nano* **2012,** *6* (12), 10816-10824.

129. Zhao, J. W.; Davis, J. J.; Sansom, M. S. P.; Hung, A., Exploring the electronic and mechanical properties of protein using conducting atomic force microscopy. *Journal of the American Chemical Society* **2004,** *126* (17), 5601-5609.

130. Zhao, J. W.; Davis, J. J., Molecular electron transfer of protein junctions characterised by conducting atomic force microscopy. *Colloids and Surfaces B-Biointerfaces* **2005,** *40* (3-4), 189-194.

131. Mentovich, E. D.; Belgorodsky, B.; Richter, S., Resolving the Mystery of the Elusive Peak: Negative Differential Resistance in Redox Proteins. *Journal of Physical Chemistry Letters* **2011,** *2* (10), 1125-1128.

132. Ron, I.; Pecht, I.; Sheves, M.; Cahen, D., Proteins as Solid-State Electronic Conductors. *Accounts of Chemical Research* **2010,** *43* (7), 945-953.

133. Marshall, N. M.; Garner, D. K.; Wilson, T. D.; Gao, Y.-G.; Robinson, H.; Nilges, M. J.; Lu, Y., Rationally tuning the reduction potential of a single cupredoxin beyond the natural range. *Nature* **2009,** *462* (7269), 113-U127.

134. Lancaster, K. M.; Sproules, S.; Palmer, J. H.; Richards, J. H.; Gray, H. B., Outer-Sphere Effects on Reduction Potentials of Copper Sites in Proteins: The Curious Case of High Potential Type 2 C112D/M121E Pseudomonas aeruginosa Azurin. *Journal of the American Chemical Society* **2010,** *132* (41), 14590-14595.

135. Chung, Y. H.; Lee, T.; Park, H. J.; Yun, W. S.; Min, J.; Choi, J. W., Nanoscale biomemory composed of recombinant azurin on a nanogap electrode. *Nanotechnology* **2013,** *24* (36).

136. Yagati, A. K.; Kim, S. U.; Lee, T.; Min, J.; Choi, J. W., Recombinant azurin-CdSe/ZnS hybrid structures for nanoscale resistive random access memory device. *Biosensors & Bioelectronics* **2017,** *90*, 23-30.

137. Alessandrini, A.; Salerno, M.; Frabboni, S.; Facci, P., Single-metalloprotein wet biotransistor. *Applied Physics Letters* **2005,** *86* (13).

138. Nelson, N., Plant Photosystem I - The Most Efficient Nano-Photochemical Machine. *Journal of Nanoscience and Nanotechnology* **2009,** *9* (3), 1709-1713.

139. Golbeck, J. H., A comparative analysis of the spin state distribution of in vitro and in vivo mutants of PsaC - A biochemical argument for the sequence of electron transfer in Photosystem I as F-X -> F-A -> F-B -> ferredoxin/flavodoxin. *Photosynthesis Research* **1999,** *61* (2), 107-144.

140. Das, R.; Kiley, P. J.; Segal, M.; Norville, J.; Yu, A. A.; Wang, L. Y.; Trammell, S. A.; Reddick, L. E.; Kumar, R.; Stellacci, F.; Lebedev, N.; Schnur, J.; Bruce, B. D.; Zhang, S. G.; Baldo, M., Integration of photosynthetic protein molecular complexes in solid-state electronic devices. *Nano Letters* **2004,** *4* (6), 1079-1083.

141. Castaneda Ocampo, O. E.; Gordiichuk, P.; Catarci, S.; Gautier, D. A.; Herrmann, A.; Chiechi, R. C., Mechanism of Orientation-Dependent Asymmetric Charge Transport in Tunneling Junctions Comprising Photosystem I. *Journal of the American Chemical Society* **2015,** *137* (26), 8419-27.

142. Beebe, J. M.; Kim, B.; Gadzuk, J. W.; Frisbie, C. D.; Kushmerick, J. G., Transition from direct tunneling to field emission in metal-molecule-metal junctions. *Physical Review Letters* **2006,** *97* (2).

143. Gerster, D.; Reichert, J.; Bi, H.; Barth, J. V.; Kaniber, S. M.; Holleitner, A. W.; Visoly-Fisher, I.; Sergani, S.; Carmeli, I., Photocurrent of a single photosynthetic protein. *Nature Nanotechnology* **2012,** *7* (10), 673-676.

144. Mikayama, T.; Iida, K.; Suemori, Y.; Dewa, T.; Miyashita, T.; Nango, M.; Gardiner, A. T.; Cogdell, R. J., The Electronic Behavior of a Photosynthetic Reaction Center Monitored by Conductive Atomic Force Microscopy. *Journal of Nanoscience and Nanotechnology* **2009,** *9* (1), 97-107.

145. Carmeli, I.; Kumar, K. S.; Heifler, O.; Carmeli, C.; Naaman, R., Spin Selectivity in Electron Transfer in Photosystem I. *Angewandte Chemie-International Edition* **2014,** *53* (34), 8953-8958.

146. Iwuchukwu, I. J.; Vaughn, M.; Myers, N.; O'Neill, H.; Frymier, P.; Bruce, B. D., Self-organized photosynthetic nanoparticle for cell-free hydrogen production. *Nature Nanotechnology* **2010,** *5* (1), 73-79.

147. Iwuchukwu, I. J.; Iwuchukwu, E.; Le, R.; Paquet, C.; Sawhney, R.; Bruce, B.; Frymier, P., Optimization of photosynthetic hydrogen yield from platinized photosystem I complexes using response surface methodology. *International Journal of Hydrogen Energy* **2011,** *36* (18), 11684-11692.

148. Lubner, C. E.; Heinnickel, M.; Bryant, D. A.; Golbeck, J. H., Wiring photosystem I for electron transfer to a tethered redox dye. *Energy & Environmental Science* **2011,** *4* (7), 2428-2434.

149. Utschig, L. M.; Silver, S. C.; Mulfort, K. L.; Tiede, D. M., Nature-Driven Photochemistry for Catalytic Solar Hydrogen Production: A Photosystem I-Transition Metal Catalyst Hybrid. *Journal of the American Chemical Society* **2011,** *133* (41), 16334-16337.

150. Utschig, L. M.; Dimitrijevic, N. M.; Poluektov, O. G.; Chemerisov, S. D.; Mulfort, K. L.; Tiede, D. M., Photocatalytic Hydrogen Production from Noncovalent Biohybrid Photosystem I/Pt Nanoparticle Complexes. *Journal of Physical Chemistry Letters* **2011,** *2* (3), 236-241.

151. Greenbaum, E., Platinized Chloroplasts - A Novel Photocatalytic Material. *Science* **1985,** *230* (4732), 1373-1375.

152. Grimme, R. A.; Lubner, C. E.; Golbeck, J. H., Maximizing H-2 production in Photosystem I/dithiol molecular wire/platinum nanoparticle bioconjugates. *Dalton Transactions* **2009,** (45), 10106-10113.

153. Esper, B.; Badura, A.; Roegner, M., Photosynthesis as a power supply for (bio-)hydrogen production. *Trends in Plant Science* **2006,** *11* (11), 543-549.

154. Millsaps, J. F.; Bruce, B. D.; Lee, J. W.; Greenbaum, E., Nanoscale photosynthesis: Photocatalytic production of hydrogen by platinized photosystem I reaction centers. *Photochemistry and Photobiology* **2001,** *73* (6), 630-635.

155. Tapia, C.; Milton, R. D.; Pankratova, G.; Minteer, S. D.; Akerlund, H.-E.; Leech, D.; De Lacey, A. L.; Pita, M.; Gorton, L., Wiring of PhotosystemI and Hydrogenase on an Electrode for Photoelectrochemical H-2 Production by using Redox Polymers for Relatively Positive Onset Potential. *Chemelectrochem* **2017,** *4* (1), 90-95.

156. Utschig, L. M.; Soltau, S. R.; Tiede, D. M., Light-driven hydrogen production from Photosystem I-catalyst hybrids. *Current Opinion in Chemical Biology* **2015,** *25*, 1-8.

157. Mukherjee, D.; Vaughn, M.; Khomami, B.; Bruce, B. D., Modulation of cyanobacterial photosystem I deposition properties on alkanethiolate Au substrate by various experimental conditions. *Colloids and Surfaces B-Biointerfaces* **2011,** *88* (1), 181-190.

158. Carmeli, I.; Frolov, L.; Carmeli, C.; Richter, S., Photovoltaic activity of photosystem I-based self-assembled monolayer. *Journal of the American Chemical Society* **2007,** *129* (41), 12352-+.

159. Terasaki, N.; Yamamoto, N.; Hiraga, T.; Sato, I.; Inoue, Y.; Yamada, S., Fabrication of novel photosystem I-gold nanoparticle hybrids and their photocurrent enhancement. *Thin Solid Films* **2006,** *499* (1-2), 153-156.

160. Badura, A.; Guschin, D.; Kothe, T.; Kopczak, M. J.; Schuhmann, W.; Roegner, M., Photocurrent generation by photosystem 1 integrated in crosslinked redox hydrogels. *Energy & Environmental Science* **2011,** *4* (7), 2435-2440.

161. Gizzie, E. A.; Niezgoda, J. S.; Robinson, M. T.; Harris, A. G.; Jennings, G. K.; Rosenthal, S. J.; Cliffel, D. E., Photosystem I-polyaniline/TiO2 solid-state solar cells: simple devices for biohybrid solar energy conversion. *Energy & Environmental Science* **2015,** *8* (12), 3572-3576.

162. Carmeli, I.; Lieberman, I.; Kraversky, L.; Fan, Z.; Govorov, A. O.; Markovich, G.; Richter, S., Broad Band Enhancement of Light Absorption in Photosystem I by Metal Nanoparticle Antennas. *Nano Letters* **2010,** *10* (6), 2069-2074.

163. Kiley, P.; Zhao, X. J.; Vaughn, M.; Baldo, M. A.; Bruce, B. D.; Zhang, S. G., Self-assembling peptide detergents stabilize isolated photosystem I on a dry surface for an extended time. *Plos Biology* **2005,** *3* (7), 1180-1186.

164. Ciesielski, P. N.; Hijazi, F. M.; Scott, A. M.; Faulkner, C. J.; Beard, L.; Emmett, K.; Rosenthal, S. J.; Cliffel, D.; Jennings, G. K., Photosystem I - Based biohybrid photoelectrochemical cells. *Bioresource Technology* **2010,** *101* (9), 3047-3053.

165. Binnig, G.; Rohrer, H., Scanning Tunneling Microscopy. *Helvetica Physica Acta* **1982,** *55* (6), 726-735.

166. Binnig, G.; Quate, C. F.; Gerber, C., Atomic Force Microscope. *Physical Review Letters* **1986,** *56* (9), 930-933.

167. Lindsay, S., *Introduction to Nanoscience*. Oxfird University Press: 2009.

168. Guell, A. G.; Diez-Perez, I.; Gorostiza, P.; Sanz, F., Preparation of reliable probes for electrochemical tunneling spectroscopy. *Analytical Chemistry* **2004,** *76* (17), 5218-5222.

169. Friis, E. P.; Andersen, J. E. T.; Kharkats, Y. I.; Kuznetsov, A. M.; Nichols, R. J.; Zhang, J. D.; Ulstrup, J., An approach to long-range electron transfer mechanisms in metalloproteins: In situ scanning tunneling microscopy with submolecular resolution. *Proceedings of the National Academy of Sciences of the United States of America* **1999,** *96* (4), 1379-1384.

170. Diez-Perez, I.; Guell, A. G.; Sanz, F.; Gorostiza, P., Conductance maps by electrochemical tunneling spectroscopy to fingerprint the electrode electronic structure. *Analytical Chemistry* **2006,** *78* (20), 7325-7329.

171. Alessandrini, A.; Gerunda, M.; Canters, G. W.; Verbeet, M. P.; Facci, P., Electron tunnelling through azurin is mediated by the active site Cu ion. *Chemical Physics Letters* **2003,** *376* (5-6), 625-630.

172. Della Pia, E. A.; Chi, Q. J.; Jones, D. D.; Macdonald, J. E.; Ulstrup, J.; Elliott, M., Single-Molecule Mapping of Long-range Electron Transport for a Cytochrome b(562) Variant. *Nano Letters* **2011,** *11* (1), 176-182.

173. Della Pia, E. A.; Chi, Q. J.; Macdonald, J. E.; Ulstrup, J.; Jones, D. D.; Elliott, M., Fast electron transfer through a single molecule natively structured redox protein. *Nanoscale* **2012,** *4* (22), 7106-7113.

174. Della Pia, E. A.; Elliott, M.; Jones, D. D.; Macdonald, J. E., Orientation-Dependent Electron Transport in a Single Redox Protein. *Acs Nano* **2012,** *6* (1), 355-361.

175. Climent, V.; Zhang, J. D.; Friis, E. P.; Ostergaard, L. H.; Ulstrup, J., Voltammetry and Single-Molecule in Situ Scanning Tunneling Microscopy of Laccases and Bilirubin Oxidase in Electrocatalytic Dioxygen Reduction on Au(111) Single-Crystal Electrodes. *Journal of Physical Chemistry C* **2012,** *116* (1), 1232-1243.

176. Madden, C.; Vaughn, M. D.; Diez-Perez, I.; Brown, K. A.; King, P. W.; Gust, D.; Moore, A. L.; Moore, T. A., Catalytic Turnover of FeFe -Hydrogenase Based on Single-Molecule Imaging. *Journal of the American Chemical Society* **2012,** *134* (3), 1577-1582.

177. Davis, J. J.; Wang, N.; Morgan, A.; Zhang, T. T.; Zhao, J. W., Metalloprotein tunnel junctions: compressional modulation of barrier height and transport mechanism. *Faraday Discussions* **2006,** *131*, 167-179.

178. Zhao, J. W.; Davis, J. J., Force dependent metalloprotein conductance by conducting atomic force microscopy. *Nanotechnology* **2003,** *14* (9), 1023-1028.

179. Andolfi, L.; Cannistraro, S., Conductive atomic force microscopy study of plastocyanin molecules adsorbed on gold electrode. *Surface Science* **2005,** *598* (1-3), 68-77.

180. Berthoumieu, O.; Patil, A. V.; Xi, W.; Aslimovska, L.; Davis, J. J.; Watts, A., Molecular Scale Conductance Photoswitching in Engineered Bacteriorhodopsin. *Nano Letters* **2012,** *12* (2), 899-903.

181. Mukhopadhyay, S.; Cohen, S. R.; Marchak, D.; Friedman, N.; Pecht, I.; Sheves, M.; Cahen, D., Nanoscale Electron Transport and Photodynamics Enhancement in Lipid-Depleted Bacteriorhodopsin Monomers. *Acs Nano* **2014,** *8* (8), 7714-7722.

182. Kondo, M.; Iida, K.; Dewa, T.; Tanaka, H.; Ogawa, T.; Nagashima, S.; Nagashima, K. V. P.; Shimada, K.; Hashimoto, H.; Gardiner, A. T.; Cogdell, R. J.;

Nango, M., Photocurrent and Electronic Activities of Oriented-His-Tagged Photosynthetic Light-Harvesting/Reaction Center Core Complexes Assembled onto a Gold Electrode. *Biomacromolecules* **2012,** *13* (2), 432-438.

183. Sumino, A.; Dewa, T.; Sasaki, N.; Kondo, M.; Nango, M., Electron Conduction and Photocurrent Generation of a Light-Harvesting/Reaction Center Core Complex in Lipid Membrane Environments. *Journal of Physical Chemistry Letters* **2013,** *4* (7), 1087-1092.

184. Lee, I.; Lee, J. W.; Warmack, R. J.; Allison, D. P.; Greenbaum, E., Molecular Electronics Of A Single Photosystem-I Reaction-Center - Studies With Scanning-Tunneling-Microscopy And Spectroscopy. *Proceedings of the National Academy of Sciences of the United States of America* **1995,** *92* (6), 1965-1969.

185. Lee, I.; Lee, J. W.; Greenbaum, E., Biomolecular electronics: Vectorial arrays of photosynthetic reaction centers. *Physical Review Letters* **1997,** *79* (17), 3294-3297.

186. Pobelov, I. V.; Mohos, M.; Yoshida, K.; Kolivoska, V.; Avdic, A.; Lugstein, A.; Bertagnolli, E.; Leonhardt, K.; Denuault, G.; Gollas, B.; Wandlowski, T., Electrochemical current-sensing atomic force microscopy in conductive solutions. *Nanotechnology* **2013,** *24* (11).

187. Halbritter, J.; Repphun, G.; Vinzelberg, S.; Staikov, G.; Lorenz, W. J., Tunneling Mechanisms In Electrochemical Stm - Distance And Voltage Tunneling Spectroscopy. *Electrochimica Acta* **1995,** *40* (10), 1385-1394.

188. Nagy, G.; Wandlowski, T., Double layer properties of Au(111)/H2SO4 (Cl)+Cu2+ from distance tunneling spectroscopy. *Langmuir* **2003,** *19* (24), 10271-10280.

189. Pompa, P. P.; Bramanti, A.; Maruccio, G.; Cingolani, R.; De Rienzo, F.; Corni, S.; Di Felice, R.; Rinaldi, R., Retention of nativelike conformation by proteins embedded in high external electric fields. *Journal of Chemical Physics* **2005,** *122* (18).

190. Horcas, I.; Fernandez, R.; Gomez-Rodriguez, J. M.; Colchero, J.; Gomez-Herrero, J.; Baro, A. M., WSXM: A software for scanning probe microscopy and a tool for nanotechnology. *Review of Scientific Instruments* **2007,** *78* (1).

191. Pobelov, I. V.; Li, Z.; Wandlowski, T., Electrolyte Gating in Redox-Active Tunneling Junctions-An Electrochemical STM Approach. *Journal of the American Chemical Society* **2008,** *130* (47), 16045-16054.

192. Artes, J. M.; Lopez-Martinez, M.; Giraudet, A.; Diez-Perez, I.; Sanz, F.; Gorostiza, P., Current-voltage characteristics and transition voltage spectroscopy of individual redox proteins. *Journal of the American Chemical Society* **2012,** *134* (50).

193. Guo, S.; Hihath, J.; Diez-Perez, I.; Tao, N., Measurement and Statistical Analysis of Single-Molecule Current-Voltage Characteristics, Transition Voltage Spectroscopy, and Tunneling Barrier Height. *Journal of the American Chemical Society* **2011,** *133* (47), 19189-19197.

194. Kim, B.; Choi, S. H.; Zhu, X. Y.; Frisbie, C. D., Molecular Tunnel Junctions Based on pi-Conjugated Oligoacene Thiols and Dithiols between Ag, Au, and Pt Contacts: Effect of Surface Linking Group and Metal Work Function. *Journal of the American Chemical Society* **2011,** *133* (49), 19864-19877.

195. Bennett, N.; Xu, G.; Esdaile, L. J.; Anderson, H. L.; Macdonald, J. E.; Elliott, M., Transition Voltage Spectroscopy of Porphyrin Molecular Wires. *Small* **2010,** *6* (22), 2604-2611.

196. Pan, J.; Jing, T. W.; Lindsay, S. M., Tunneling Barriers In Electrochemical Scanning-Tunneling-Microscopy. *Journal of Physical Chemistry* **1994,** *98* (16), 4205-4208.

197. Parsons, R., Electrical Double-Layer - Recent Experimental And Theoretical Developments. *Chemical Reviews* **1990,** *90* (5), 813-826.

198. Wigginton, N. S.; Rosso, K. M.; Stack, A. G.; Hochella, M. F., Jr., Long-Range Electron Transfer across Cytochrome-Hematite (alpha-Fe2O3) Interfaces. *Journal of Physical Chemistry C* **2009,** *113* (6), 2096-2103.

199. Haiss, W.; Nichols, R. J.; van Zalinge, H.; Higgins, S. J.; Bethell, D.; Schiffrin, D. J., Measurement of single molecule conductivity using the spontaneous formation of molecular wires. *Physical Chemistry Chemical Physics* **2004,** *6* (17), 4330-4337.

200. Baldea, I., Interpretation of Stochastic Events in Single-Molecule Measurements of Conductance and Transition Voltage Spectroscopy. *Journal of the American Chemical Society* **2012,** *134* (18), 7958-7962.

201. Monari, S.; Battistuzzi, G.; Bortolotti, C. A.; Yanagisawa, S.; Sato, K.; Li, C.; Salard, I.; Kostrz, D.; Borsari, M.; Ranieri, A.; Dennison, C.; Sola, M., Understanding the Mechanism of Short-Range Electron Transfer Using an Immobilized Cupredoxin. *Journal of the American Chemical Society* **2012,** *134* (29), 11848-11851.

202. Kim, S.-U.; Yagati, A. K.; Min, J.; Choi, J.-W., Nanoscale protein-based memory device composed of recombinant azurin. *Biomaterials* **2010,** *31* (6), 1293-1298.

203. Lyons, J. A.; Aragao, D.; Slattery, O.; Pisliakov, A. V.; Soulimane, T.; Caffrey, M., Structural insights into electron transfer in caa(3)-type cytochrome oxidase. *Nature* **2012,** *487* (7408), 514-518.

204. Tersoff, J.; Hamann, D. R., Theory Of The Scanning Tunneling Microscope. *Physical Review B* **1985,** *31* (2), 805-813.

205. Diez-Perez, I.; Sanz, F.; Gorostiza, P., In situ studies of metal passive films. *Current Opinion in Solid State & Materials Science* **2006,** *10* (3-4), 144-152.

206. Lee, T.; Kim, S.-U.; Min, J.; Choi, J.-W., Multilevel Biomemory Device Consisting of Recombinant Azurin/Cytochrome c. *Advanced Materials* **2010,** *22* (4), 510-+.

207. Manders, E. M. M.; Verbeek, F. J.; Aten, J. A., Measurement Of Colocalization Of Objects In Dual-Color Confocal Images. *Journal of Microscopy-Oxford* **1993,** *169*, 375-382.

208. Diez-Perez, I.; Gorostiza, P.; Sanz, F., Direct evidence of the electronic conduction of the passive film on iron by EC-STM. *Journal of the Electrochemical Society* **2003,** *150* (7), B348-B354.

209. Avouris, P.; Lyo, I. W.; Molinasmata, P., STM Studies Of The Interaction Of Surface-State Electrons On Metals With Steps And Adsorbates. *Chemical Physics Letters* **1995,** *240* (5-6), 423-428.

210. Everson, M. P.; Jaklevic, R. C.; Shen, W. D., Measurement Of The Local Density Of States On A Metal-Surface - Scanning Tunneling Spectroscopic Imaging Of Au(111). *Journal of Vacuum Science & Technology a-Vacuum Surfaces and Films* **1990,** *8* (5), 3662-3665.

211. Suganuma, Y.; Tomitori, M., Differential conductance imaging of Si and Ge islands deposited on Si(001) by scanning tunneling microscopy. *Japanese Journal of Applied Physics Part 1-Regular Papers Short Notes & Review Papers* **1998,** *37* (6B), 3789-3792.

212. Artes, J. M.; Lopez-Martinez, M.; Giraudet, A.; Diez-Perez, I.; Sanz, F.; Gorostiza, P., Current-Voltage Characteristics and Transition Voltage Spectroscopy of Individual Redox Proteins. *Journal of the American Chemical Society* **2012,** *134* (50), 20218-20221.

213. Venkat, A. S.; Corni, S.; Di Felice, R., Etectronic coupling between azurin and gold at different protein/substrate orientations. *Small* **2007,** *3* (8), 1431-1437.

214. Van De Kamp, M.; Floris, R.; Hali, F. C.; Canters, G. W., Site-Directed Mutagenesis Reveals That The Hydrophobic Patch Of Azurin Mediates Electron Transfer. *Journal of the American Chemical Society* **1990,** *112* (2), 907-908.

215. van Amsterdam, I. M. C.; Ubbink, M.; Einsle, O.; Messerschmidt, A.; Merli, A.; Cavazzini, D.; Rossi, G. L.; Canters, G. W., Dramatic modulation of electron transfer in protein complexes by crosslinking. *Nature Structural Biology* **2002,** *9* (1), 48-52.

216. Chang, B.-Y.; Park, S.-M., Electrochemical Impedance Spectroscopy. *Annual Review of Analytical Chemistry, Vol 3* **2010,** *3*, 207-229.

217. Nichols, R. J.; Higgins, S. J., Single-Molecule Electronics: Chemical and Analytical Perspectives. *Annual Review of Analytical Chemistry, Vol 8* **2015,** *8*, 389-417.

218. Aragones, A. C.; Aravena, D.; Cerda, J. I.; Acis-Castillo, Z.; Li, H.; Antonio Real, J.; Sanz, F.; Hihath, J.; Ruiz, E.; Diez-Perez, I., Large Conductance Switching in a Single-Molecule Device through Room Temperature Spin-Dependent Transport. *Nano Letters* **2016,** *16* (1), 218-226.

219. Xiang, L.; Palma, J. L.; Bruot, C.; Mujica, V.; Ratner, M. A.; Tao, N., Intermediate tunnelling-hopping regime in DNA charge transport. *Nature Chemistry* **2015,** *7* (3), 221-226.

220. Lyshevski, S. E., *Nano and Molecular Electronics Handbook*. CRC Press: 2016.

221. Raccosta, S.; Baldacchini, C.; Bizzarri, A. R.; Cannistraro, S., Conductive atomic force microscopy study of single molecule electron transport through the Azurin-gold nanoparticle system. *Applied Physics Letters* **2013,** *102* (20).

222. Davis, J. J.; Peters, B.; Xi, W., Force modulation and electrochemical gating of conductance in a cytochrome. *Journal of Physics-Condensed Matter* **2008,** *20* (37).

223. Axford, D. N.; Davis, J. J., Electron flux through apo- and holoferritin. *Nanotechnology* **2007,** *18* (14).

224. Lugstein, A.; Bertagnolli, E.; Kranz, C.; Kueng, A.; Mizaikoff, B., Integrating micro- and nanoelectrodes into atomic force microscopy cantilevers using focused ion beam techniques. *Applied Physics Letters* **2002,** *81* (2), 349-351.

225. Izquierdo, J.; Fernandez-Perez, B. M.; Eifert, A.; Souto, R. M.; Kranz, C., Simultaneous Atomic Force-Scanning Electrochemical Microscopy (AFM-SECM) Imaging Of Copper Dissolution. *Electrochimica Acta* **2016,** *201*, 320-332.

226. Birhane, Y.; Otero, J.; Perez-Murano, F.; Furnagalli, L.; Gomila, G.; Bausells, J., Batch fabrication of insulated conductive scanning probe microscopy probes with reduced capacitive coupling. *Microelectronic Engineering* **2014,** *119*, 44-47.

227. Eifert, A.; Mizaikoff, B.; Kranz, C., Advanced fabrication process for combined atomic force-scanning electrochemical microscopy (AFM-SECM) probes. *Micron* **2015,** *68*, 27-35.

228. Wain, A. J.; Pollard, A. J.; Richter, C., High-Resolution Electrochemical and Topographical Imaging Using Batch-Fabricated Cantilever Probes. *Analytical Chemistry* **2014,** *86* (10), 5143-5149.

229. Knittel, P.; Higgins, M. J.; Kranz, C., Nanoscopic polypyrrole AFM-SECM probes enabling force measurements under potential control. *Nanoscale* **2014,** *6* (4), 2255-2260.

230. Abbou, J.; Demaille, C.; Druet, M.; Moiroux, J., Fabrication of submicrometer-sized gold electrodes of controlled geometry for scanning electrochemical-atomic force microscopy. *Analytical Chemistry* **2002,** *74* (24), 6355-6363.

231. Hong, S. S.; Cha, J. J.; Cui, Y., One Nanometer Resolution Electrical Probe via Atomic Metal Filament Formation. *Nano Letters* **2011,** *11* (1), 231-235.

232. Patel, A. N.; Anne, A.; Chovin, A.; Demaille, C.; Grelet, E.; Michon, T.; Taofifenua, C., Scaffolding of Enzymes on Virus Nanoarrays: Effects of Confinement and Virus Organization on Biocatalysis. *Small* **2017,** *13* (13).

233. Ghorbal, A.; Grisotto, F.; Charlier, J.; Palacin, S.; Goyer, C.; Demaille, C.; Ben Brahim, A., Nano-Electrochemistry and Nano-Electrografting with an Original Combined AFM-SECM. *Nanomaterials* **2013,** *3* (2), 303-316.

234. Anne, A.; Bahri, M. A.; Chovin, A.; Demaille, C.; Taofifenua, C., Probing the conformation and 2D-distribution of pyrene-terminated redox-labeled poly(ethylene glycol) chains end-adsorbed on HOPG using cyclic voltammetry and atomic force electrochemical microscopy. *Physical Chemistry Chemical Physics* **2014,** *16* (10), 4642-4652.

235. Abbou, J.; Anne, A.; Demaille, C., Probing the structure and dynamics of end-grafted flexible polymer chain layers by combined atomic force-electrochemical microscopy. Cyclic voltammetry within nanometer-thick macromolecular poly(ethylene glycol) layers. *Journal of the American Chemical Society* **2004,** *126* (32), 10095-10108.

236. Proksch, R.; Schaffer, T. E.; Cleveland, J. P.; Callahan, R. C.; Viani, M. B., Finite optical spot size and position corrections in thermal spring constant calibration. *Nanotechnology* **2004,** *15* (9), 1344-1350.

237. Ghilane, J.; Hapiot, P.; Bard, A. J., Metal/polypyrrole quasi-reference electrode for voltammetry in nonaqueous and aqueous solutions. *Analytical Chemistry* **2006,** *78* (19), 6868-6872.

238. Rodriguez, R. D.; Anne, A.; Cambril, E.; Demaille, C., Optimized hand fabricated AFM probes for simultaneous topographical and electrochemical tapping mode imaging. *Ultramicroscopy* **2011,** *111* (8), 973-981.

239. Wain, A. J.; Cox, D.; Zhou, S.; Turnbull, A., High-aspect ratio needle probes for combined scanning electrochemical microscopy-Atomic force microscopy. *Electrochemistry Communications* **2011,** *13* (1), 78-81.

240. Gray, H. B.; Malmstrom, B. G.; Williams, R. J. P., Copper coordination in blue proteins. *Journal of Biological Inorganic Chemistry* **2000,** *5* (5), 551-559.

241. Fotiadis, D.; Muller, D. J.; Tsiotis, G.; Hasler, L.; Tittmann, P.; Mini, T.; Jeno, P.; Gross, H.; Engel, A., Surface analysis of the photosystem I complex by electron and atomic force microscopy. *Journal of Molecular Biology* **1998,** *283* (1), 83-94.

242. Mukherjee, D.; May, M.; Vaughn, M.; Bruce, B. D.; Khomami, B., Controlling the Morphology of Photosystem I Assembly on Thiol-Activated Au Substrates. *Langmuir* **2010,** *26* (20), 16048-16054.

243. Liu, J. G.; Zhang, X. F.; Wang, M.; Liu, J.; Cao, M. W.; Lu, J. R.; Cui, Z. F., Characterization of photosystem I from spinach: effect of solution pH. *Photosynthesis Research* **2012,** *112* (1), 63-70.

244. Manocchi, A. K.; Baker, D. R.; Pendley, S. S.; Nguyen, K.; Hurley, M. M.; Bruce, B. D.; Sumner, J. J.; Lundgren, C. A., Photocurrent Generation from Surface Assembled Photosystem I on Alkanethiol Modified Electrodes. *Langmuir* **2013,** *29* (7), 2412-2419.

245. Toporik, H.; Carmeli, I.; Volotsenko, I.; Molotskii, M.; Rosenwaks, Y.; Carmeli, C.; Nelson, N., Large Photovoltages Generated by Plant Photosystem I Crystals. *Advanced Materials* **2012,** *24* (22), 2988-2991.

246. Lee, I.; Lee, J. W.; Stubna, A.; Greenbaum, E., Measurement of electrostatic potentials above oriented single photosynthetic reaction centers. *Journal of Physical Chemistry B* **2000,** *104* (11), 2439-2443.

247. Frolov, L.; Rosenwaks, Y.; Carmeli, C.; Carmeli, I., Fabrication of a photoelectronic device by direct chemical binding of the photosynthetic reaction center protein to metal surfaces. *Advanced Materials* **2005,** *17* (20), 2434-+.

248. Chen, G. P.; Hijazi, F. M.; LeBlanc, G.; Jennings, G. K.; Cliffel, D. E., Scanning Electrochemical Microscopy of Multilayer Photosystem I Photoelectrochemistry. *Ecs Electrochemistry Letters* **2013,** *2* (12), H59-H62.

249. Kievit, O.; Brudvig, G. W., Direct electrochemistry of photosystem I. *Journal of Electroanalytical Chemistry* **2001,** *497* (1-2), 139-149.

250. Ko, B. S.; Babcock, B.; Jennings, G. K.; Tilden, S. G.; Peterson, R. R.; Cliffel, D.; Greenbaum, E., Effect of surface composition on the adsorption of photosystem I onto alkanethiolate self-assembled monolayers on gold. *Langmuir* **2004,** *20* (10), 4033-4038.

251. Ciobanu, M.; Kincaid, H. A.; Lo, V.; Dukes, A. D.; Jennings, G. K.; Cliffel, D. E., Electrochemistry and photoelectrochemistry of photosystem I adsorbed on hydroxyl-terminated monolayers. *Journal of Electroanalytical Chemistry* **2007,** *599* (1), 72-78.

252. Kincaid, H. A.; Niedringhaus, T.; Ciobanu, M.; Cliffel, D. E.; Jennings, G. K., Entrapment of photosystem I within self-assembled films. *Langmuir* **2006,** *22* (19), 8114-8120.

253. Faulkner, C. J.; Lees, S.; Ciesielski, P. N.; Cliffel, D. E.; Jennings, G. K., Rapid assembly of photosystem I monolayers on gold electrodes. *Langmuir* **2008,** *24* (16), 8409-8412.

254. Wientjes, E.; Croce, R., PMS: Photosystem I electron donor or fluorescence quencher. *Photosynthesis Research* **2012,** *111* (1-2), 185-191.

255. Bassi, R.; Simpson, D., Chlorophyll-Protein Complexes Of Barley Photosystem-I. *European Journal of Biochemistry* **1987,** *163* (2), 221-230.

256. Caffarri, S.; Croce, R.; Breton, J.; Bassi, R., The major antenna complex of photosystem II has a xanthophyll binding site not involved in light harvesting. *Journal of Biological Chemistry* **2001,** *276* (38), 35924-35933.

257. Wientjes, E.; van Amerongen, H.; Croce, R., LHCII is an antenna of both photosystems after long-term acclimation. *Biochimica Et Biophysica Acta-Bioenergetics* **2013,** *1827* (3), 420-426.

258. Chen, G.; LeBlanc, G.; Jennings, G. K.; Cliffel, D. E., Effect of Redox Mediator on the Photo-Induced Current of a Photosystem I Modified Electrode. *Journal of the Electrochemical Society* **2013,** *160* (6), H315-H320.

259. Capdevila, D. A.; Marmisolle, W. A.; Williams, F. J.; Murgida, D. H., Phosphate mediated adsorption and electron transfer of cytochrome c. A time-resolved SERR spectroelectrochemical study. *Physical Chemistry Chemical Physics* **2013,** *15* (15), 5386-5394.

260. Hugelmann, M.; Schindler, W., Tunnel barrier height oscillations at the solid/liquid interface. *Surface Science* **2003,** *541* (1-3), L643-L648.